

## **INFORMATION TO USERS**

This manuscript has been reproduced from the microfilm master. UMI films the text directly from the original or copy submitted. Thus, some thesis and dissertation copies are in typewriter face, while others may be from any type of computer printer.

**The quality of this reproduction is dependent upon the quality of the copy submitted.** Broken or indistinct print, colored or poor quality illustrations and photographs, print bleedthrough, substandard margins, and improper alignment can adversely affect reproduction.

In the unlikely event that the author did not send UMI a complete manuscript and there are missing pages, these will be noted. Also, if unauthorized copyright material had to be removed, a note will indicate the deletion.

Oversize materials (e.g., maps, drawings, charts) are reproduced by sectioning the original, beginning at the upper left-hand corner and continuing from left to right in equal sections with small overlaps.

ProQuest Information and Learning  
300 North Zeeb Road, Ann Arbor, MI 48106-1346 USA  
800-521-0600

**UMI<sup>®</sup>**



**An Inverse-Problem Approach to Spatial Distortion  
Correction in MRI**

by

Patrice Munger

Department of Biomedical Engineering  
McGill University, Montréal, Québec, Canada

A Thesis submitted to the Faculty of Graduate Studies  
and Research in partial fulfillment of the requirements  
for the degree of Doctor of Philosophy.

© P. Munger, March 2001.



**National Library  
of Canada**

**Acquisitions and  
Bibliographic Services**

**395 Wellington Street  
Ottawa ON K1A 0N4  
Canada**

**Bibliothèque nationale  
du Canada**

**Acquisitions et  
services bibliographiques**

**395, rue Wellington  
Ottawa ON K1A 0N4  
Canada**

*Your file Votre référence*

*Our file Notre référence*

**The author has granted a non-exclusive licence allowing the National Library of Canada to reproduce, loan, distribute or sell copies of this thesis in microform, paper or electronic formats.**

**The author retains ownership of the copyright in this thesis. Neither the thesis nor substantial extracts from it may be printed or otherwise reproduced without the author's permission.**

**L'auteur a accordé une licence non exclusive permettant à la Bibliothèque nationale du Canada de reproduire, prêter, distribuer ou vendre des copies de cette thèse sous la forme de microfiche/film, de reproduction sur papier ou sur format électronique.**

**L'auteur conserve la propriété du droit d'auteur qui protège cette thèse. Ni la thèse ni des extraits substantiels de celle-ci ne doivent être imprimés ou autrement reproduits sans son autorisation.**

0-612-70107-7

**Canada**

# Contents

<b>Contents</b>	<b>ii</b>
<b>Abstract</b>	<b>vii</b>
<b>Résumé</b>	<b>ix</b>
<b>List of figures</b>	<b>xiii</b>
<b>Acknowledgments</b>	<b>xiv</b>
<b>List of Symbols and Abbreviations</b>	<b>xv</b>
<b>List of Contributions</b>	<b>xviii</b>
<b>1 Introduction</b>	<b>1</b>
1.1 Proposed Solution . . . . .	4
1.2 Goals of the thesis . . . . .	6
1.3 Outline of the thesis . . . . .	6
1.4 Original contributions . . . . .	7
<b>2 Background</b>	<b>9</b>
2.1 Magnetic Resonance Imaging . . . . .	9
2.1.1 Nuclear spin and magnetic moment . . . . .	9

2.1.2	Polarization: equilibrium magnetization . . . . .	10
2.1.3	Dynamics of the magnetization . . . . .	12
2.1.4	Excitation . . . . .	14
2.1.5	Relaxation . . . . .	16
2.1.6	Imaging principles . . . . .	17
2.1.7	K-space interpretation . . . . .	18
2.1.8	Sampling . . . . .	20
2.1.9	Selective Excitation . . . . .	22
2.1.10	Signal-to-noise ratio . . . . .	24
2.2	Distortion in MRI: Theory . . . . .	26
2.2.1	Machine-Dependant factors . . . . .	26
2.2.2	Subject-Dependant factors . . . . .	30
2.2.3	Mathematical characterization of distortion . . . . .	34
2.3	Echo Planar Imaging . . . . .	36
2.4	Field mapping . . . . .	40
2.4.1	Spin-echo imaging . . . . .	40
2.4.2	Gradient echo imaging . . . . .	42
2.4.3	$B_0$ map noise . . . . .	42
2.5	Iterative Methods for Linear Systems . . . . .	44
2.5.1	Quadratic Forms . . . . .	44
2.5.2	General search direction: line minimization . . . . .	45
2.5.3	General search direction method . . . . .	45
2.5.4	Normal equations . . . . .	47
2.5.5	Conjugate Gradient and noise . . . . .	49
<b>3</b>	<b>Distortion Correction in MRI</b>	<b>51</b>
3.1	Post-processing approaches . . . . .	51

3.1.1	$B_0$ map based methods . . . . .	52
3.1.2	Double-gradient Methods . . . . .	57
3.2	Modified Acquisitions . . . . .	60
3.2.1	View angle tilting . . . . .	61
3.2.2	Echo-projection and similar techniques. . . . .	62
3.2.3	Conclusion . . . . .	63
<b>4</b>	<b>EPI correction as an image restoration problem</b>	<b>66</b>
4.1	EPI Imaging Equation . . . . .	67
4.2	EPI point spread function (PSF) . . . . .	68
4.3	Matrix formulation . . . . .	70
4.3.1	Low rank approximation of the kernel . . . . .	74
4.4	Implementation of 2D correction . . . . .	77
4.4.1	$B_0$ map processing . . . . .	77
4.4.2	4D kernel computation . . . . .	83
4.4.3	Solution of the 4D linear system . . . . .	84
4.5	1D correction approximation . . . . .	84
4.5.1	Solution of the 2D linear systems . . . . .	88
4.6	Summary . . . . .	89
<b>5</b>	<b>Computer simulations and techniques comparisons</b>	<b>90</b>
5.1	Introduction . . . . .	90
5.2	Methods . . . . .	91
5.2.1	Analytic phantom . . . . .	91
5.2.2	EPI k-space trajectory . . . . .	91
5.2.3	Simulation of EPI images . . . . .	92
5.2.4	Validation methodology . . . . .	95

5.2.5	Implementation of the CG algorithm for EPI correction . . . .	96
5.2.6	Noise and EPI images . . . . .	98
5.2.7	Noise and $B_0$ map . . . . .	98
5.2.8	Computer hardware . . . . .	99
5.3	Results . . . . .	100
5.3.1	Effect of CG parameters . . . . .	100
5.3.2	Comparison between the different methods for EPI correction	105
5.4	Discussion . . . . .	127
5.4.1	Effect of CG parameters . . . . .	127
5.4.2	Comparison between the different methods for EPI correction	128
5.4.3	General Discussion . . . . .	129
5.4.4	Conclusion . . . . .	130
<b>6</b>	<b>Application to real data</b>	<b>132</b>
6.1	Methods . . . . .	132
6.1.1	EPI imaging . . . . .	132
6.1.2	3D anatomical imaging . . . . .	132
6.2	Results . . . . .	133
6.2.1	Correction of real EPI images . . . . .	133
6.2.2	Results of correction of a 3D flash image . . . . .	135
6.3	Discussion . . . . .	138
6.3.1	EPI . . . . .	138
6.3.2	Gradient-echo imaging . . . . .	139
6.4	Summary . . . . .	140
<b>7</b>	<b>Conclusions</b>	<b>142</b>
7.1	Thesis Summary . . . . .	143

7.2	Main findings . . . . .	145
7.3	Future Work . . . . .	147
7.3.1	In-Vivo Experimental validation: MR tagging . . . . .	147
7.3.2	Field map acquisition and processing . . . . .	147
7.4	Concluding remarks . . . . .	148
<b>A</b>	<b>Source code</b>	<b>150</b>
A.1	CG 2D algorithm . . . . .	150
A.2	1D CG algorithm . . . . .	154
A.3	PGI and SI-PGI algorithms . . . . .	156
A.4	KSC algorithm . . . . .	163
A.5	Analytic phantom . . . . .	165
A.6	EPI image simulation . . . . .	168
A.7	K-space trajectory . . . . .	169
A.8	Support functions . . . . .	172
	<b>Bibliography</b>	<b>192</b>

# Abstract

This thesis treats of the issue of distortion in magnetic resonance (MR) imaging, with focus on Echo Planar imaging (EPI) and anatomical 3D imaging.

After a review of MR theory, the principle of image formation, an analysis of distortion in the context of MRI and field mapping principles, an analysis of the EPI image formation process, which reveals the two-dimensional nature of the EPI point-spread function (PSF), is presented, and a full 2D correction technique based on the inversion of the 4D tensor EPI imaging equation using the Conjugate Gradient (CG) method is proposed. A 1D approximation of the technique is also derived for cases where the PSF can be approximated as being one-dimensional, such as in Fourier imaging, or EPI imaging in fields with low field inhomogeneity.

The proposed technique is demonstrated by means of computer simulations, and several aspects of its implementation are studied. A comparison between different correction methods based on field map data, still using computer simulations, is presented and reveals the behaviour of the different methods when applied in non-ideal conditions.

Finally, the practical application of the proposed method is demonstrated on real EPI scans and gradient echo images.

This work reveals some interesting characteristics of the correction method based on the CG algorithm, like fast convergence, possibility to recover from severe distortions.

tions and EPI  $B_0$ -induced ghost artifacts reduction, but it also points out limitations of this correction method, such as potentially high computational cost and noise sensitivity.

# Résumé

Dans cette thèse, le problème de la distortion dans les images de résonance magnétique (IRM) est étudié, plus particulièrement dans le contexte de l'imagerie écho-planaire (EPI) ainsi que de l'imagerie de Fourier conventionnelle.

Après une révision de la théorie sous-jacente aux principes de résonance magnétique et de la nature des distortions, une analyse du processus de formation d'image par la technique EPI révèle la nature bi-dimensionnelle de la fonction d'étalement de point (PSF), et une méthode de correction 2D basée sur l'inversion, par la méthode des gradients conjugués, du système d'équations 4D représentant le problème est proposée. Ensuite, le cas particulier dans lequel la fonction d'étalement peut être approximée par une distribution unidimensionnelle est dérivé.

La méthode proposée est démontrée au moyen de simulations par ordinateur et différents aspects de l'implémentation de la méthode sont étudiés. Une comparaison des différentes méthodes de correction des distortions dans les images d'IRM dans des conditions non idéales est ensuite effectuée.

Finalement, l'application à de véritables images de résonance magnétique est démontrée dans le cas d'images écho-planaires, et d'images provenant d'une étude 3D en écho de gradient.

Ce travail révèle d'importantes caractéristiques concernant la méthode de correction basée sur les gradients conjugués, telles que la convergence rapide, la possibilité

de restorer de sévères distortions et la réduction des fantômes, dans les images EPI, causés par les inhomogénéités du champ magnétique. Il souligne par contre les limitations de cette technique, telle la sensibilité au bruit et les longs temps de calcul qu'elle requiert.

# List of Figures

1.1	1D vs. 2D correction, and the respective applications. . . . .	5
2.1	Available states of the magnetic moment for a spin 1/2. . . . .	10
2.2	Distribution of spin population. . . . .	11
2.3	Precession of the magnetization . . . . .	13
2.4	Excitation in the lab reference frame. . . . .	14
2.5	Excitation in the rotating reference frame. . . . .	15
2.6	Encoding in spin-warp imaging and the relation to k-space trajectory. . . . .	20
2.7	Examples of the NMR sampling function magnitude. . . . .	22
2.8	Simultaneous measurement of $B_0$ and gradient errors. . . . .	29
2.9	The EPI image process. . . . .	38
2.10	The EPI sequence and its k-space trajectory . . . . .	39
2.11	Spin-echo sequence with the gradient echo shifted from the spin-echo. . . . .	41
2.12	Typical gradient-echo sequence. . . . .	43
2.13	Conjugate gradient iterations on noisy data . . . . .	50
3.1	Sekihara's geometrical distortion correction method. . . . .	54
3.2	Weis's distortion correction method . . . . .	55
3.3	Conjugate Phase Reconstruction for an EPI image. . . . .	58
3.4	Illustration of the Tilted View Angle Technique. . . . .	60

3.5	Echo Projection Imaging . . . . .	64
4.1	The EPI point spread function . . . . .	71
4.2	Illustration of the origin of field-inhomogeneity related ghosts. . . . .	72
4.3	The 4D tensor equation in matrix form. . . . .	73
4.4	Line component of the EPI k-space trajectory. . . . .	78
4.5	Column component of the EPI k-space trajectory. . . . .	79
4.6	Main component of the EPI point spread function. . . . .	80
4.7	Ghost component of the EPI point spread function. . . . .	81
4.8	The two components of the EPI PSF . . . . .	82
4.9	Algorithm for the computation of the 4D kernel $\tilde{\mathbf{A}}$ . . . . .	83
4.10	Various matrices involved in 1D correction. . . . .	88
5.1	Analytic phantom used in the simulation . . . . .	92
5.2	Simulated EPI images and $B_0$ maps used in the simulations . . . . .	93
5.3	Algorithm for the calculation of the simulated EPI image. . . . .	94
5.4	Effect of the number of iterations in the 2D CG algorithm. . . . .	101
5.5	Effect of the sparsity level of the kernel in the 2D CG algorithm. . . . .	102
5.6	Effect of the number of iterations in the 1D CG algorithm . . . . .	103
5.7	Effect of the sparsity of the kernel in the 1D CG algorithm. . . . .	104
5.8	Simulations of the effect of EPI image noise . . . . .	107
5.9	Effect of EPI image noise. Maximum $B_0$ amplitude = $\pm 25$ Hz. . . . .	108
5.10	Effect of EPI image noise. Maximum $B_0$ amplitude = $\pm 50$ Hz. . . . .	109
5.11	Effect of EPI image noise. Maximum $B_0$ amplitude = $\pm 75$ Hz. . . . .	110
5.12	Correction with EPI SNR= $\infty$ , and $B_0$ max. amplitude = $\pm 25$ Hz. . . . .	111
5.13	Correction with EPI SNR=70, maximum $B_0$ amplitude = $\pm 25$ Hz. . . . .	112
5.14	Correction with EPI SNR=50, maximum $B_0$ amplitude = $\pm 25$ Hz. . . . .	113

5.15	Correction with EPI SNR= $\infty$ , maximum $B_0$ amplitude = $\pm 50$ Hz.	114
5.16	Correction with EPI SNR=70, maximum $B_0$ amplitude = $\pm 50$ Hz.	115
5.17	Correction with EPI SNR=50, maximum $B_0$ amplitude = $\pm 50$ Hz.	116
5.18	Correction with EPI SNR= $\infty$ , maximum $B_0$ amplitude = $\pm 75$ Hz.	117
5.19	Correction with EPI SNR=70, maximum $B_0$ amplitude = $\pm 75$ Hz.	118
5.20	Correction with EPI SNR=50, maximum $B_0$ amplitude = $\pm 75$ Hz.	119
5.21	Simulations of the effect of $B_0$ map noise	121
5.22	Effect of $B_0$ map noise	122
5.23	Correction with $B_0$ SNR=10, maximum $B_0$ amplitude = $\pm 50$ Hz.	123
5.24	Correction with $B_0$ SNR=50, maximum $B_0$ amplitude = $\pm 50$ Hz.	124
5.25	Correction with a noisy, unprocessed $B_0$ map.	125
5.26	Correction with a noisy, masked $B_0$ map.	126
6.1	High and low bandwidth gradient-echo 3D imaging sequences.	134
6.2	$B_0$ field mapping sequence.	135
6.3	CP and CG reconstructions of the EPI image of a phantom.	136
6.4	Distortion correction on a volunteers head EPI image.	137
6.5	Distortion correction a flash acquisition with the CG1D method.	139

# Acknowledgments

This work would have been impossible without the support of the following people:

- My supervisors Dr G. Bruce Pike and Dr Terry M. Peters for their countless hours of availability. Their contribution reached well further the strict scientific aspects. The journey through the final version of this thesis has been long and difficult. Without their patience, support and direction, this work may never have been completed.
- John Sled for providing me with his spline smoothing source code and program.
- Gerard Crelier, for helpful discussions and suggestions.
- Brad Gill and Jeff Atkinson for taking some of their precious time to serve as subjects for in-vivo experiments.
- Dr. Abas Sadikot and Dr. Mario Alonso, neurosurgeons, for helping me to appreciate the clinical relevance of my work.

# List of Symbols and Abbreviations

$e$	Euler Constant (2.71828 ...)
$\gamma$	Gyromagnetic Ratio of Hydrogen Nucleus (42.58 MHz/T)
$i$	Imaginary Number Unit ( $\sqrt{-1}$ )
$\omega$	Precession frequency
$\pi$	Pi Constant (3.141592 ...)
$\hbar$	Plank's constant ( $1.054589 \cdot 10^{-34} J \cdot s$ )
2-D	Two-Dimensional
3-D	Three-Dimensional
ADC	Analog to Digital Converter
$B_0$	Main Static Magnetic Field
$B_1$	Excitation field
BW	Bandwidth
$BW_{\text{pix}}$	Bandwidth per pixel
CG	Conjugate Gradient
CP	Conjugate Phase
CT	Computerized Tomography
DFT	Discrete Fourier Transform
$G_x$	Gradient Field in the $x$ -direction

$G_y$	Gradient Field in the $y$ -direction
$G_z$	Gradient Field in the $z$ -direction
EEG	Electroencephalography
EMF	Electromotive Force
EPI	Echo-planar Imaging
fMRI	Functional MRI
FFT	Fast Fourier Transform
FOV	Field of view
Hz	Hertz frequency unit ( $s^{-1}$ )
ICGI	Intensity Corrected Geometrical Interpolation
IDFT	Inverse Discrete Fourier Transform
IFFT	Inverse Fast Fourier Transform
IGNS	Image-Guided Neurosurgery
KSC	K-space Correction
MR	Magnetic Resonance
MRI	Magnetic Resonance Imaging
NMR	Nuclear Magnetic Resonance
PGI	Pure Geometrical Interpolation
ppm	Part per million
PSF	Point Spread Function
RF	Radio-Frequency
RMS	Root Mean Square
SI-ICGI	Sinc Interpolated Intensity Compensated Geometrical Interpolation
SI-PGI	Sinc Interpolated Pure Geometrical Interpolation
SNR	Signal-to-noise Ratio

<b>SVD</b>	<b>Singular Value Decomposition</b>
<b>T</b>	<b>Tesla magnetic induction unit</b>
<b>T1</b>	<b>Longitudinal Relaxation Time</b>
<b>T2</b>	<b>Transverse Relaxation Time</b>
<b>TE</b>	<b>Echo Time</b>
<b>TR</b>	<b>Repetition Time</b>
<b>M</b>	<b>Magnetization</b>

# List of Contributions

1. P. Munger, G.R. Crelier, T.M. Peters and G.B. Pike. An inverse problem approach to the correction of distortion in EPI images. *IEEE Trans Med Imaging*. 2000 Jul;19(7):681-9.
2. P. Munger. Beyond Fourier: The Wavelet Transform. Chapter 5 of the book "The Fourier Transform in Biomedical Engineering", Terry M. Peters, Jackie Williams Editors, Birkausser, Boston, 1998.
3. P. Munger, G. Crelier, T.M. Peters and G.B. Pike. Conjugate Gradient Restoration of EPI Images. Proceedings of the Sixth Annual Meeting of the International Society for Magnetic Resonance in Medicine. Sydney, Australia, April 1998.
4. G.R. Crelier, R.D. Hoge, P. Munger and G.B. Pike. Perfusion-based functional magnetic resonance imaging with single-shot RARE and GRASE acquisitions. *Magn Reson Med*. 1999 Jan;41(1):132-6.
5. T.M. Peters, B.L.K. Davey, P. Munger, R.M. Comeau, A. Evans, and A. Olivier. Three-dimensional multi-modal image-guidance for neurosurgery. *IEEE Transactions on Medical Imaging*, 15:121-128, 1996.

# Chapter 1

## Introduction

Since its introduction in 1973, Magnetic Resonance Imaging (MRI) [64] has gained wide acceptance as a valuable diagnostic modality, in part because of its ability to represent different properties of the tissues (proton nuclei density, relaxation times, susceptibility, etc.) and different physiological aspects (flow, diffusion, perfusion, motion, etc.), and also due to its non-invasive nature.

In the early days of MRI, data were acquired as projections and well known reconstruction methods, such as filtered back-projection, used in x-ray computed tomography, were applied to MRI data. The advent of Fourier imaging, [59, 35] which allowed higher signal-to-noise ratios (SNR), marked an important step in MR imaging. These techniques are however limited in certain clinical applications due to the fact that static field inhomogeneities translate as geometrical distortions of the images. In contrast, in projection reconstruction, the effect of field inhomogeneity is to cause blurring in the reconstructed image [62].

Advances in magnet design technology have contributed significantly to improve this situation, but still, MRI does not in general meet the geometrical accuracy requirements of applications such as Image-Guided Neurosurgery (IGNS). Furthermore,

very rapid imaging techniques, such as echo planar imaging (EPI), can suffer extreme distortion. This is in part due to the fact that field inhomogeneities do not arise exclusively from imperfect magnet design, but also from magnetic properties of different tissues, cavities and biological liquids.

A number of methods have been proposed to reduce or eliminate the deleterious effects of static field inhomogeneities. These include pre-scan shimming [89], modified acquisitions and post-processing corrections. All of these methods have drawbacks, such as increased imaging time, incomplete correction, requirement of human intervention or dependence on the imager hardware that limit their use in real-life clinical problems that often generate a large amount of data.

The problem of distortion becomes particularly important in areas of dynamic EPI and Image-Guided Neurosurgery.

### **Dynamic EPI**

Echo-Planar Imaging (EPI) [67] is an ultra-fast imaging technique that is extremely sensitive to static field inhomogeneities because of the low effective bandwidth per pixel used. Large distortions in EPI, in addition to field inhomogeneity-related artifacts, restricts its use in IGNS.

Additionally, the analysis of functional MRI (fMRI) data acquired with EPI sequences [9] often relies on the precise registration between anatomical and fMRI images. Distortion in EPI images may result in a misalignment between the functional and anatomical data, which may in turn interfere with the interpretation of results.

The effect of static field inhomogeneities on EPI imaging is not only geometric distortion, but also signal loss. Furthermore, the geometric distortion cannot be considered as strictly one-dimensional. In this case, a full 2D correction scheme can be considered.

### **Image-Guided Neurosurgery using volumetric gradient-echo data**

For the large majority of qualitative diagnostic applications, small geometrical distortions can be safely ignored without major consequences. However, Image-Guided Neurosurgery, which uses pre-operative MRI anatomical information to provide interactive guidance during open-cranium surgery [28, 29, 40, 41, 81], often requires geometric accuracy on the order of 1 mm. This geometrical accuracy requirement may not be reached in some regions of the MRI volume, especially near air-tissue interfaces. Distortion of stereotactic frame fiducial markers, used to establish image geometry, is also a concern [15].

Although the use of high bandwidth sequences may help to reduce the effect of geometrical distortions, this is achieved at the expense of reduced signal-to-noise ratio (SNR) [80, 27]. Hence, an efficient correction method could contribute to relaxing the tradeoff between SNR and geometrical accuracy and provide distortion-free images with higher SNR.

The general requirements for a distortion correction technique may be stated as follows:

- Acquisition time – minimal overhead on total acquisition time.
- Automatic – no or minimal intervention of the operator.
- Computation time – can be applied in a reasonable time compared to the normal time-scale between pre-operative scan and surgery, in the case of IGNS, or compared to the time required for data analysis, in the case of functional EPI.
- Effective – provides stable and significant correction of distortion and related effects without introducing new artifacts.

## 1.1 Proposed Solution

This thesis addresses the problem of distortion in MRI from first principles, with an approach similar to image restoration and inverse problem methods. From the knowledge of the non-ideal conditions and the detailed mathematical process by which the images are formed, one tries to mathematically invert the process to yield a restored image, free from the effects of non-ideal conditions. Although this approach can in general be applied to any imaging situation, some types of image degradation, such as blurring or dephasing, where part of the information is irreversibly lost, are handled with difficulty by inverse problem approaches. The case of distortion is different because, when distortion is not too severe, no information is lost. In that case, we have found that it can be effectively dealt with using inverse problem methods.

The primary field of application of the proposed inverse-problem method is the restoration of EPI images. Because EPI image degradations due to static field inhomogeneity is not strictly one-dimensional, we state the problem in terms of a general 4D linear system of equations relating the ideal, undistorted image and the measured image.

We further show that this method can be applied as well to 1D correction problems. EPI distortion can be approximated, through some simplifications of the k-space trajectory, as a one-dimensional distortion problem. All Fourier imaging methods (including 3D gradient-echo imaging) in which a single k-space line is acquired at each excitation, strictly conforms to the 1D distortion problem. Figure 1.1 illustrates the relationship between the 2D and 1D correction methods and the imaging situations where they are applicable.

Whether it is applied to 1D or 2D restoration, the proposed approaches follow the same logic. Under ideal conditions, this imaging equation, relating the measured signal and the imaged object, takes the form of a discrete Fourier transform (DFT),

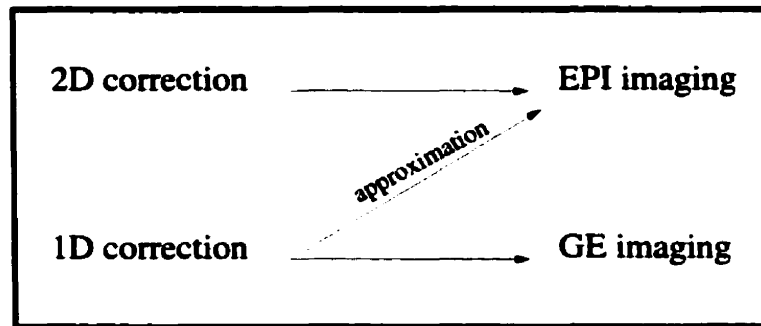


Figure 1.1: 1D vs. 2D correction, and the respective applications.

*Relation between 1D and 2D correction vs. relevant imaging techniques. In order to take account of the two-dimensional nature of EPI image degradations, a 2D correction method is needed (top arrow). However, the EPI degradation can also be approximated as one-dimensional, which can be addressed by a 1D correction method (diagonal arrow). In the case of anatomical 3D imaging, the image degradation is strictly one-dimensional, and the 1D method is suitable for this case (bottom arrow).*

and the image is normally reconstructed using an inverse FFT. When static field inhomogeneities are present, the equation deviates from the DFT relationship and a more general solution approach must be taken. The distortion correction problem can be expressed as a system of linear equations relating the distorted image with the ideal, distortion-free image. In the case of 2D processing, the linear relationship takes the form of a 4D tensor equation that can be reshaped into a large system of linear equations. In the case of 1D processing, the correction consists of independent resolution of a linear system of equation for each column of an image<sup>a</sup>.

It has been found in practice that using iterative techniques such as the Conjugate Gradient method or the Steepest Descent method [47, 97] provided good correction of geometrical and associated intensity distortions in a very small number of iterations (2-3). Furthermore, because the distortion problem is stated in the form of a system

<sup>a</sup>For simplicity, "column" refers to the direction in which the primary distortion occurs. It is the readout direction in Fourier imaging, and the phase encoding direction for EPI.

of linear equations, any technique for solving linear systems may be used, provided that the size of the linear system allows them to be used practically (i.e. matrix inversion, Gaussian elimination, etc).

## 1.2 Goals of the thesis

The objectives of this thesis are:

- Formulate the MRI image distortion correction process as an inverse problem.
- Implement and evaluate this inverse problem method for the full 2D correction of EPI images.
- Adapt the method for 1D processing.
- Compare the performance of some of the  $B_0$ -map based distortion correction methods for EPI image processing in different non-ideal situations.
- Evaluate the 2D and 1D correction approaches for EPI imaging sequence.

## 1.3 Outline of the thesis

Chapter 2 presents a review of the relevant physical and mathematical aspects of MRI together with introductions to different topics of interest with respect to this work. This includes the physical conditions giving rise to the distortion phenomenon, MR image formation principles, EPI imaging, field mapping and a brief introduction to iterative methods for solving linear systems of equations.

A literature review of the the main classes of existing distortion correction methods is presented in Chapter 3. The attention is mainly focused on “ $B_0$  map”-based correction methods, because these methods allow the subject-dependent, as well as the

machine dependent distortions to be addressed, and because the correction approach proposed in this thesis falls into that category.

The core of the thesis begins at Chapter 4, where the mathematical foundation of the proposed method is developed. The EPI imaging process is discussed in detail and a full 2D formulation is developed. A description of the 1D correction model, following [54] is also presented, and the approximation allowing the EPI distortion to be corrected by the 1D model is discussed.

Chapter 5 presents computer simulations allowing the basic properties of the proposed method to be better understood, and comparisons with other existing  $B_0$  map based methods to be achieved.

Chapter 6 deals with the specific application of the proposed method to the correction to Echo-Planar images. The focus is to demonstrate the applicability of the inverse-problem approach to EPI and 3D imaging applications, and to discuss the practical issues encountered.

## 1.4 Original contributions

The original contributions of this thesis are:

- Formulation of the EPI geometrical distortion correction problem as a 2D inverse problem.
- Design, implementation and evaluation of a full 2D correction scheme, extending that proposed by [54], on EPI images that corrects for geometrical distortion, and for second order effects related to field inhomogeneity.
- Evaluation of the potential advantages of using 2D correction, rather than 1D, for EPI data.

- Objective comparison of existing 1D distortion correction methods by means of computer simulations.
- Evaluation of the developed correction methods in an in-vivo human imaging context.

# Chapter 2

## Background

### 2.1 Magnetic Resonance Imaging

Magnetic resonance imaging is a technique based on the physical phenomenon called *nuclear magnetic resonance* (NMR) [105, 50, 22]. This section briefly reviews the basic physics of NMR necessary for the understanding of this thesis and discusses the means by which this phenomenon is exploited for imaging.

#### 2.1.1 Nuclear spin and magnetic moment

Atomic nuclei constituted with an odd number of protons and/or neutrons possess a magnetic moment  $\mathbf{m}$  related to their spin angular momentum  $\mathbf{s}$  by:

$$\mathbf{m} = \gamma \mathbf{s}, \quad (2.1)$$

where  $\gamma$  is a constant (different for each nuclear species) called the *gyro-magnetic ratio*. Hydrogen nuclei ( $^1\text{H}$ ) are the most common in biological tissues and are the ones generally used for generating the MRI signal. The gyro-magnetic ratio of hydrogen is 42.58 MHz/T.

Because the angular momentum is subject to spatial quantization in the presence of a magnetic field, so is the magnetic moment. If the magnetic field is directed along the  $z$ -axis, the  $z$ -projection of the angular momentum of a nucleus with spin quantum number  $I$  may only take a set of discrete values  $m_s \hbar$ , where  $m_s = -I, -I + 1, \dots, I - 1, I$ , and is called the *magnetic quantum number* and  $\hbar$  is Planck's constant. According to Eq. (2.1) the  $z$ -projection of the magnetic moment may take the values  $m_z = \gamma m_s \hbar$ . The magnitude of the angular momentum is  $\sqrt{I(I+1)}\hbar$ .

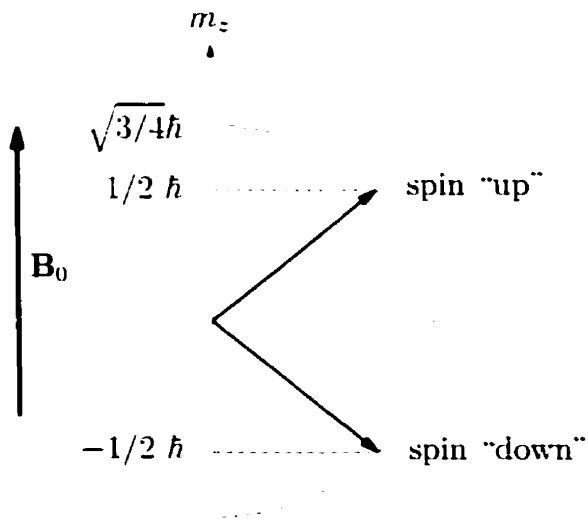


Figure 2.1: Available states of the magnetic moment for a spin  $1/2$ .  
*In the presence of a magnetic field  $B_0$ , two values of the  $z$ -projection of the magnetic moment are possible for a spin  $1/2$ . These states are referred to as "spin up" and "spin down".*

### 2.1.2 Polarization: equilibrium magnetization

The physical quantity manipulated and measured in NMR is the magnetization  $M$  that is defined as the total magnetic moment per unit volume present in a given material. The first step to observe the NMR phenomenon is to create a polarization, which generates an equilibrium magnetization.

Because  $^1\text{H}$  nuclei have a spin quantum number  $I = 1/2$ , the spin<sup>a</sup> population is split into two energy levels in the presence of a static magnetic field  $\mathbf{B}_0$ <sup>b</sup> directed along the  $z$ -axis.

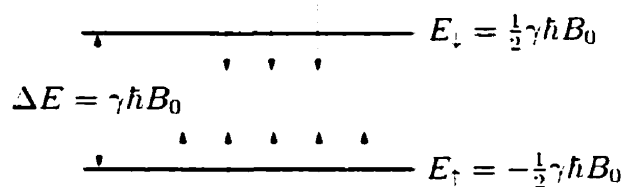


Figure 2.2: Distribution of spin population.

*The excess of spins in the “up” state, giving rise to the net magnetization, is dictated by the Boltzmann distribution.*

The two states are typically referred to as “spin up” and “spin down” according to the sign of the  $z$  component of the magnetic moment (Fig. 2.1). The energy separation between the two levels is  $\Delta E = \gamma \frac{\hbar}{2\pi} B_0 = \gamma\hbar B_0$  (Fig. 2.2). The relative number of spins per unit volume occupying the two states at a temperature  $T$  is dictated by the Boltzmann equation

$$\frac{n_\uparrow}{n_\downarrow} = e^{\frac{\Delta E}{kT}} = e^{\frac{\gamma\hbar B_0}{kT}}, \quad (2.2)$$

where  $k$  is Boltzmann’s constant, and where  $n_\uparrow$  and  $n_\downarrow$  are the number of spins in the

<sup>a</sup>It is current practice to call “spin” the nuclei exhibiting this property. Hence, the terms “spins” and “nuclei” may be used interchangeably.

<sup>b</sup> Calling  $\mathbf{B}$  “magnetic field” is an abuse of language currently committed in the MRI literature. In the physics literature, the symbol  $\mathbf{B}$  refers to the *magnetic induction* or *magnetic flux density*, and the magnetic field is represented by  $\mathbf{H}$ . The important thing to remember is that  $\mathbf{H}$  results only from the current distribution while  $\mathbf{B}$  includes a contribution due the magnetic properties of the surrounding material. Because the MRI signal always arises in some material, the relevant vector is  $\mathbf{B}$ . From now on, we will retain the MRI convention and refer to  $\mathbf{B}$  as the magnetic field.

“up” and “down” states respectively. This excess of spins in the “up” state ,

$$n_{\uparrow} - n_{\downarrow} = N \tanh \frac{\gamma \hbar B_0}{2kT} \approx N \frac{\gamma \hbar B_0}{2kT}, \quad (2.3)$$

where  $N = n_{\uparrow} + n_{\downarrow}$  is the total number of spins per unit volume, produces a net macroscopic magnetization vector  $\mathbf{M}_0$ , directed along the  $z$ -axis, whose amplitude is:

$$M_0 = \frac{1}{2} \gamma \hbar (n_{\uparrow} - n_{\downarrow}) = \frac{N \gamma^2 \hbar^2 B_0}{4kT}. \quad (2.4)$$

In the classical view, the net equilibrium magnetization arises from the partial alignment of the spin’s magnetic dipoles with the static magnetic field  $\mathbf{B}_0$ .

### 2.1.3 Dynamics of the magnetization

In classical terms, the basic equation describing the behaviour of a magnetic moment  $\mathbf{m}(t)$  experiencing a magnetic field  $\mathbf{B}(t)$  is derived by equating the torque experienced by the magnetic moment,  $\gamma \mathbf{m}(t) \times \mathbf{B}(t)$ , with the temporal rate of change of the angular momentum,  $d\mathbf{m}(t)/dt$ .

$$\frac{d\mathbf{m}(t)}{dt} = \gamma \mathbf{m}(t) \times \mathbf{B}(t). \quad (2.5)$$

However, at a microscopic level, quantum mechanics provides the only accurate description of the behaviour of the spins. Nevertheless, it can be shown that, under the conditions of minimally interacting spins, the equation for the time evolution of the expectation value of the magnetic moment operators is exactly the same as the classical equation [25, 1]. This legitimizes the extension of the above equation to describe the dynamic behaviour of the net magnetization:

$$\frac{d\mathbf{M}(t)}{dt} = \gamma \mathbf{M}(t) \times \mathbf{B}(t). \quad (2.6)$$

The solution of this differential equation in the case of a static magnetic field  $\mathbf{B}_0$  (it

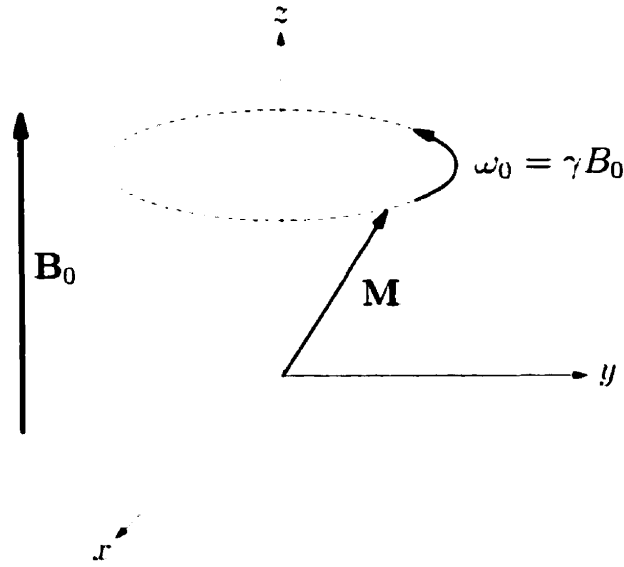


Figure 2.3: Precession of the magnetization

*In the presence of a static magnetic field  $\mathbf{B}_0$ , the magnitude of the magnetization  $\mathbf{M}$  remains constant while its projection in the  $x$ - $y$  plane rotates at an angular rate  $\gamma B_0$  around the  $z$ -axis.*

is assumed by convention that  $\mathbf{B}_0$  is directed along the positive  $z$ -axis) is:

$$M_{xy} \equiv M_x + iM_y = e^{-i\gamma B_0 t} \quad (2.7)$$

$$M_z = \text{constant}. \quad (2.8)$$

Hence, the magnetization vector remains constant in magnitude and undergoes a precession at an angular rate

$$\omega_0 = \gamma B_0 \quad (2.9)$$

around the  $z$ -axis (Fig. 2.3). Equation (2.6) is known as the *Larmor equation* and  $\omega_0$  as the *Larmor frequency*. For hydrogen nuclei and for a typical 1.5 Teslas magnetic field strength, the Larmor frequency is  $42.58 \text{ MHz/T} \times 1.5 \text{ T} = 63.9 \text{ MHz}$

We will see shortly that Eq. (2.6) does not take the important relaxation processes into account. It is however suitable for describing the magnetization behaviour when

the time scale involved is short compared to the relaxation constants. Hereafter, the quantities  $M_{xy}$  and  $M_z$  will be referred to as *transverse magnetization* and *longitudinal magnetization* respectively.

The use of complex notation in Eq. (2.7) will be useful when dealing with the Fourier interpretation of the imaging process.

### 2.1.4 Excitation

Excitation refers to the process of disturbing the net magnetization from its equilibrium state by the application of radio-frequency (RF) fields.

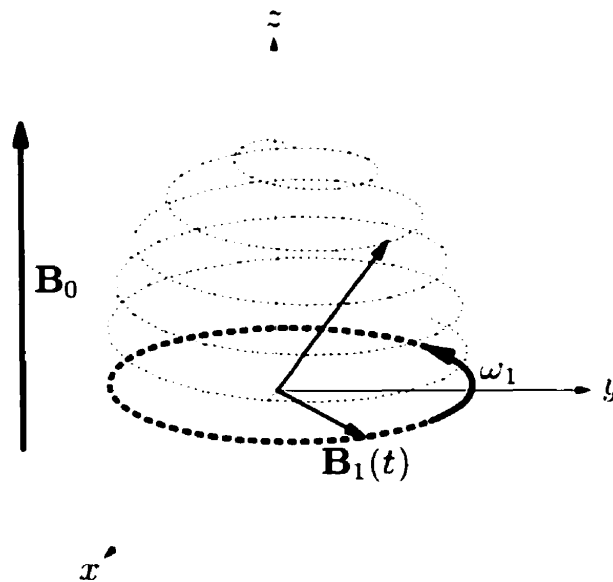


Figure 2.4: Excitation in the lab reference frame.

*The precessing magnetization can be tipped away from its equilibrium state when a rotating magnetic field in the  $x$ - $y$  plane  $B_1(t)$  is applied.*

The magnetization can be moved away from its equilibrium position if a magnetic field  $B_1(t)$  rotating in the transverse ( $xy$ ) plane at an angular frequency  $\omega_{RF}$  is applied (Fig 2.4). In order to write the solution of (2.6), it is useful to adopt a frame of

reference that rotates around the  $z$ -axis at  $\omega_{\text{RF}}$ , the angular rate of  $\mathbf{B}_1$ . In the rotating frame, the solution is again a precession of the magnetic moment vector, but around a magnetic field  $\mathbf{B}_{\text{eff}}$  given by

$$\mathbf{B}_{\text{eff}} = \frac{\Delta\omega\hat{z}'}{\gamma} + \mathbf{B}'_1, \quad (2.10)$$

where  $\Delta\omega = \omega_0 - \omega_{\text{RF}}$  is the difference between the Larmor frequency  $\gamma B_0$  and that of the rotating frame, and  $\hat{z}'$  is the unit vector directed along the positive  $z'$ -axis (Fig. 2.5).

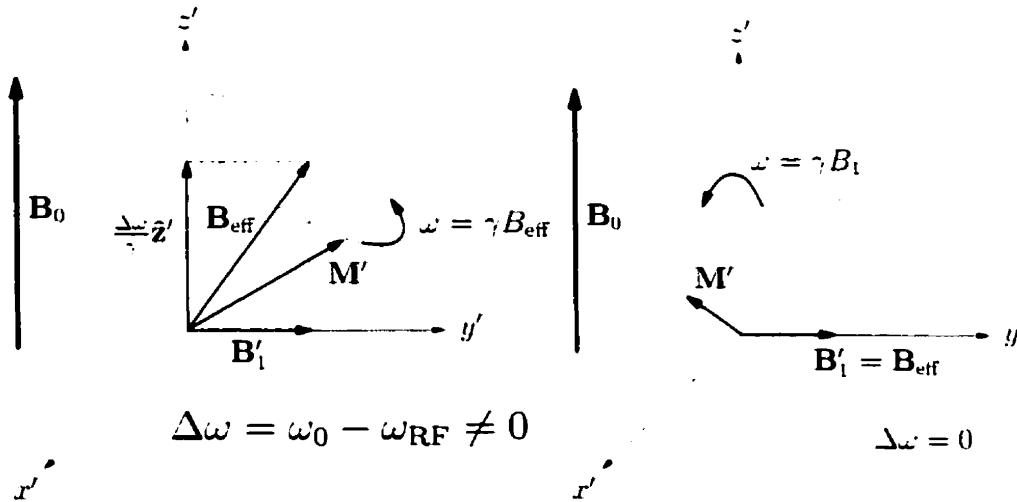


Figure 2.5: Excitation in the rotating reference frame.

*The excitation is described more simply in a reference frame rotating together with with the rotating  $\mathbf{B}_1$  field. In this reference frame, the effect of the  $\mathbf{B}_1$  field is to change the direction along which the precession takes place. When the angular rate of  $\mathbf{B}_1$  is different from the Larmor frequency  $\gamma B_0$ , the magnetization precesses around the direction of  $\mathbf{B}_{\text{eff}}$  (left). When the two angular rates are equal, the “on-resonance” condition is achieved, where the magnetization can be tipped away from the  $z$ -axis the most efficiently.*

The phenomenon of resonance is exhibited in the last equation: because the amplitude of the rotating field  $\mathbf{B}_1$  is typically much smaller than that of the static field  $\mathbf{B}_0$ , the effective field in the rotating frame is very close to the  $z$ -axis unless  $\omega_1$  is

close to  $\omega_0$ . When  $\omega_1 = \omega_0$ ,  $\Delta\omega = 0$  and the effective field completely lies in the transverse plane. In this case, the magnetization precesses around the  $\mathbf{B}_1$  field and can be significantly tipped away from the  $z$ -axis, into the  $xy$  plane, if the excitation field is applied for a sufficient time.

From the quantum mechanical point of view, excitation may be considered as resulting from stimulated transitions between the different energy levels.

### 2.1.5 Relaxation

As stated before, the time evolution of the magnetization presented so far is incomplete. We introduce the Bloch equation which describes the behaviour of the net magnetization including relaxation effects [10]:

$$\frac{d\mathbf{M}(t)}{dt} = \gamma\mathbf{M}(t) \times \mathbf{B}(t) - \frac{M_x\hat{\mathbf{x}} + M_y\hat{\mathbf{y}}}{T_2} + \frac{(M_0 - M_z)\hat{\mathbf{z}}}{T_1}, \quad (2.11)$$

where  $\hat{\mathbf{x}}$ ,  $\hat{\mathbf{y}}$  and  $\hat{\mathbf{z}}$  are the unit vectors corresponding to the axes  $x$ ,  $y$  and  $z$  respectively. The first term of the Bloch equation accounts for the previously discussed time evolution of the magnetization in presence of a magnetic field. The two other terms describe the  $T_2$  (transverse) and  $T_1$  (longitudinal) relaxation processes respectively.

$T_1$  relaxation is the re-growth of the  $M_z$  component to the equilibrium value of the magnetization after a departure from this equilibrium. The recovery is approximately exponential and is associated with energy exchange between the spin system and the surrounding lattice. For this reason it is also called spin-lattice relaxation. Longitudinal relaxation may be understood by spin transitions stimulated by atomic and molecular motion of the surrounding lattice from excited energy levels to lower ones. It is principally due to the components of this motion at the Larmor frequency.

$T_2$  relaxation is due to a loss of phase coherence between the spins and is also called “spin-spin” relaxation. It is caused by the fact that the spins experience slightly

different magnetic fields (and consequently different precession frequencies) depending of the physico-chemical environment. As opposed to  $T_1$  relaxation,  $T_2$  relaxation is also affected by low frequency local field variations.

Relaxation processes play an essential role in MRI since they constitute the primary mechanism for controlling the image contrast.

In the case of a time varying magnetic field  $B_z(t)$ , the solution of the Bloch equation for the transverse magnetization, in the absence of an exciting field, is

$$M_{xy}(t) = M_{xy}(0)e^{-t/T_2}e^{-i\gamma \int_0^t B_z(\tau)d\tau}. \quad (2.12)$$

From now on,  $M$  will refer to the transverse magnetization unless stated otherwise.

### 2.1.6 Imaging principles

Once the magnetization has been tipped away from the longitudinal axis by the excitation, the resulting time-varying transverse magnetization may induce an electromotive force (EMF) in the receiver coil.

In order to form an image, the signals from different points of the imaged object must be resolved. This is performed by manipulating the phase of the spin system in a space variant manner by means of magnetic field gradients.

Consider first a one dimensional magnetization distribution  $M(x)$ . After the excitation of  $M(x)$ , the signal generated,  $s(t)$ , will be, according to (2.7),

$$\begin{aligned} s(t) &= \int_x M(x)e^{-i\gamma B_0 t} dx \\ &= e^{-i\gamma B_0 t} \int_x M(x) dx, \end{aligned} \quad (2.13)$$

which only gives information relating to the total magnetization of the distribution. To resolve different points in the distribution, a gradient field  $G_x$  (directed along the  $z$ -axis but varying in magnitude along the  $x$ -axis) is apply along with the static  $\mathbf{B}_0$

field. The total magnetic field experienced by the spins being  $\mathbf{B}_0 + G_x x \hat{\mathbf{z}}$ , the signal recorded is:

$$\begin{aligned} s(t) &= \int_x M(x) e^{-i\gamma(B_0 + G_x x)t} dx \\ &= e^{-i\gamma B_0 t} \int_x M(x) e^{-iG_x x t} dx. \end{aligned} \quad (2.14)$$

Filtering out the frequency component at  $\omega_0$  from this signal, i.e. demodulating at  $\omega_0$ , and applying the variable change  $k_x = \frac{\gamma}{2\pi} G_x t$  we obtain:

$$s(k_x) = \int_x M(x) e^{-2\pi i k_x x} dx. \quad (2.15)$$

This equation establishes that the base-band time signal generated in the presence of a gradient field is proportional to the 1D Fourier transform of the spatial magnetization distribution  $M(x)$ . Sampling this signal at equal intervals and performing a discrete Fourier transform yields the 1D image of the transverse magnetization distribution  $M(x)$ .

### 2.1.7 K-space interpretation

A very elegant and useful way to look at the MR imaging process is the *k-space* interpretation [103]. K-space refers to the 2 or 3-D Fourier transform space of the imaged object. An MRI sequence can be described as a way to collect data in k-space, and once enough data are gathered, the reconstruction can be performed and the image obtained.

To derive the general k-space formulation, we write the solution for the transverse magnetization of the Bloch equation for an arbitrary time-varying linear gradient  $\mathbf{G}(t) = [G_x(t), G_y(t), G_z(t)]$ .

$$M(\mathbf{r}, t) = M(\mathbf{r}, 0) e^{-t/T_2(\mathbf{r})} e^{-i\omega_0 t} e^{-i\gamma \int_0^t \mathbf{G}(\tau) \cdot \mathbf{r} d\tau} \quad (2.16)$$

where  $\mathbf{r} = [x, y, z]$ .

The general continuous imaging equation is obtained by integrating (2.16) over space and ignoring relaxation effects.

$$s(t) = \int_{\mathbf{r}} M(\mathbf{r}, t) d\mathbf{r} \quad (2.17)$$

$$= e^{-i\omega_0 t} \int_{\mathbf{r}} M(\mathbf{r}, 0) e^{-i\gamma \int_0^t \mathbf{G}(\tau) \cdot \mathbf{r} d\tau} d\mathbf{r}. \quad (2.18)$$

Removing the high frequency component  $e^{-i\omega_0 t}$  and letting

$$\mathbf{k} = \frac{\gamma}{2\pi} \int_t \mathbf{G}(\tau) d\tau, \quad (2.19)$$

with  $\mathbf{k} = [k_x, k_y, k_z]$ , we find

$$s(\mathbf{k}) = \int_V M(\mathbf{r}, 0) e^{-2\pi i \mathbf{k} \cdot \mathbf{r}} d\mathbf{r}. \quad (2.20)$$

In MRI, a pulse sequence generates a series of gradients in such a way as to cover the k-space data. The generality of the k-space formulation allows an infinite number of ways to perform this operation. The path along which data are measured in k-space is referred to as the *k-space trajectory*. A common k-space trajectory, that of *spin warp* imaging [35], consists of measuring one raster line of k-space for every excitation. The line encoding is referred to as *readout encoding* since data are sampled in the presence of a linear gradient that spread the frequency spectrum of the MR signal according to its origin in space. The encoding in the other direction, i.e. corresponding to moving between different lines in k-space is called the *phase encoding*. It is performed by letting the spins dephase by applying a gradient of a given amplitude during a fixed time (Fig. 2.6) <sup>c</sup>.

---

<sup>c</sup>Readout direction is often referred to as “frequency encoding” direction because different spatial positions in the image are associated with different temporal frequencies in the NMR signal. However, from the k-space perspective, frequency and phase encoding both encode the signal by imposing linear phase variations of the magnetization across the imaged object. The frequency encoding gradient does so in a continuous manner rather than discrete as in phase encoding.

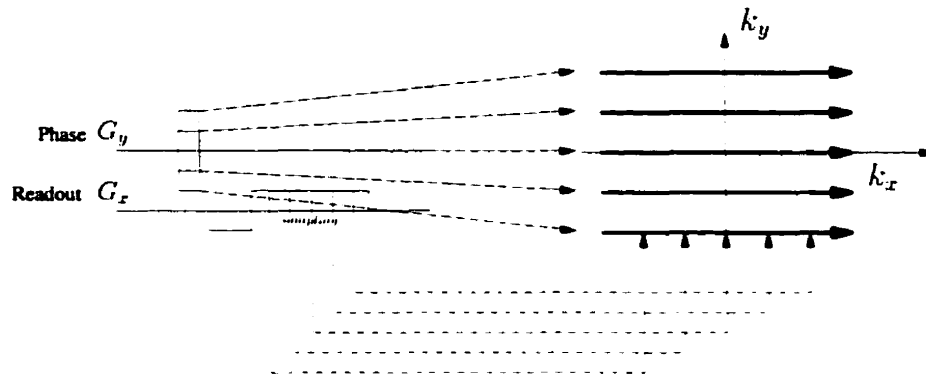


Figure 2.6: Encoding in spin-warp imaging and the relation to k-space trajectory.

*Encoding in the  $k_x$  direction is performed by applying a gradient in the  $x$ -direction while the signal is sampled. The  $x$ -direction is referred to as readout direction. Encoding in the  $k_y$  direction is done by applying a gradient in the  $y$  direction prior to signal readout. The direction  $y$  is called phase encoding direction.*

### 2.1.8 Sampling

For the reconstruction to be performed with a computer, the analog time signal must be sampled and digitized. We discuss now the implications of this sampling process. To simplify things, we consider a 1D case and assume that the k-space trajectory is linear and uniform. This assumption is satisfied when the readout gradient and the sampling rate are both constant. Since we are interested only in the relationship between the object and the image, we will not explicitly distinguish between frequency and phase encoding.

Sampling the signal involves a finite number of points  $N$ . One of the consequences of this is that higher spatial frequencies of the objects are not measured, limiting the resolution of the image. The other effect of sampling is aliasing.

The real, continuous magnetization distribution is obtained from the analog signal

by the inverse Fourier transform

$$M(x) = \int_{-\infty}^{+\infty} s(k)e^{2\pi ikx} dk \quad (2.21)$$

However in practice, the analog signal  $s(k)$  is sampled at a finite number  $N$  of locations  $n\Delta k$ , with  $n = -N/2, \dots, N/2 - 1$ . Thus, the sampled signal is:

$$s(n\Delta k) = \Delta k \int_{-\infty}^{+\infty} M(x)e^{-2\pi in\Delta kx} dx. \quad (2.22)$$

The reconstructed image  $\hat{M}(m\Delta x)$  is obtained by inverse discrete Fourier transform of the sampled signal, or

$$\begin{aligned} \hat{M}(m\Delta x) &= \sum_{n=-N/2}^{N/2-1} s(n\Delta k)e^{2\pi imn\Delta k\Delta x} \\ &= \int_{-\infty}^{+\infty} M(x) \sum_{n=-N/2}^{N/2-1} e^{2\pi in\Delta k(m\Delta x-x)} dx \\ \hat{M}(m\Delta x) &= M(x) * S(x)|_{m\Delta x}, \end{aligned} \quad (2.23)$$

where

$$\begin{aligned} S(x) &= \sum_{n=-N/2}^{N/2-1} e^{2\pi in\Delta kx} \\ &= \sum_{n=-N/2}^{N/2-1} e^{2\pi inkx/\Delta x/N} \\ &= \frac{\sin\left(\frac{\pi x}{\Delta x}\right)}{\sin\left(\frac{\pi x}{N\Delta x}\right)} e^{-\frac{\pi ix}{N\Delta x}}, \end{aligned} \quad (2.24)$$

and is called the *NMR sampling function* [80]. Equation (2.24) relates the real, continuous magnetization distribution  $M(x)$  with the finite resolution, discrete reconstructed image  $\hat{M}(m\Delta x)$ . The NMR sampling function is periodic of period  $N\Delta x = \text{FOV}$ , where FOV is the field of view, and has zeros at  $n\Delta x$  where  $n$  is an integer. Fig. 2.7 illustrates two examples of the NMR sampling function. Note that the NMR sampling function exhibits both the spread of the main peaks and the Gibbs ringing due to the finite extent sampling of k-space [112], and the aliasing caused by discrete k-space sampling.

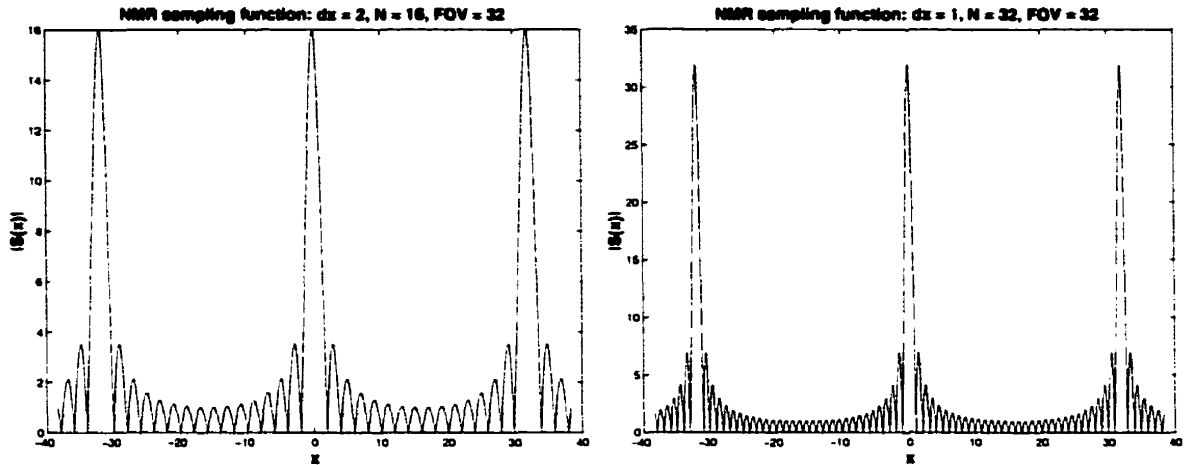


Figure 2.7: Examples of the NMR sampling function magnitude.

*The NMR sampling function relates a real, infinite resolution object, with the MR image of this object. Its period (the distance between the larger peaks) is related to the space between samples in  $k$ -space and defines the field-of-view (FOV). The smaller ripples are related to the extent of the  $k$ -space covered by the sampling and define the spatial resolution ( $dx$ ) of the image.*

### 2.1.9 Selective Excitation

An important aspect of MR imaging is the ability to selectively excite the magnetization based on its position in space.

Selective excitation is achieved by applying RF energy to the sample in the presence of a magnetic field gradient. Some insight into this process can be gained by looking at the Bloch equations. In practice, the selective excitation pulses are much shorter than the typical relaxation constants of tissues and it may be approximated that no relaxation occurs. Furthermore, the small flip angle approximation will lead to a powerful interpretation of the selective excitation in terms of Fourier relationship.

Taking  $\mathbf{B}(\mathbf{r}, t) = B'_{1y}(t) \hat{\mathbf{x}} + B'_{1y}(t) \hat{\mathbf{y}} + \mathbf{G}(t) \cdot \mathbf{r} \hat{\mathbf{z}}$ , the Larmor equation in the rotating frame can be written, in the particular case of excitation, as:

$$\frac{d}{dt} \begin{pmatrix} M'_x(\mathbf{r}, t) \\ M'_y(\mathbf{r}, t) \\ M'_z(\mathbf{r}, t) \end{pmatrix} = \gamma \begin{pmatrix} 0 & \mathbf{G}(t) \cdot \mathbf{r} & -B'_{1y}(t) \\ -\mathbf{G}(t) \cdot \mathbf{r} & 0 & B'_{1x}(t) \\ B'_{1y}(t) & -B'_{1x}(t) & 0 \end{pmatrix} \begin{pmatrix} M'_x(\mathbf{r}, t) \\ M'_y(\mathbf{r}, t) \\ M'_z(\mathbf{r}, t) \end{pmatrix} \quad (2.25)$$

The small flip angle approximation allows the equation for the  $z$  magnetization to be decoupled from that for the transverse magnetization. Letting  $M_z(\mathbf{r}, t) \approx M_0$  and  $dM_z(\mathbf{r}, t)/dt = 0$  we obtain:

$$\frac{d}{dt} \begin{pmatrix} M'_x(\mathbf{r}, t) \\ M'_y(\mathbf{r}, t) \\ M'_z(\mathbf{r}, t) \end{pmatrix} = \gamma \begin{pmatrix} 0 & \mathbf{G}(t) \cdot \mathbf{r} & -B'_{1y}(t) \\ -\mathbf{G}(t) \cdot \mathbf{r} & 0 & B'_{1x}(t) \\ 0 & 0 & 0 \end{pmatrix} \begin{pmatrix} M'_x(\mathbf{r}, t) \\ M'_y(\mathbf{r}, t) \\ M_0(\mathbf{r}) \end{pmatrix} \quad (2.26)$$

We now can write the equation for the transverse magnetization  $M = M_x + iM_y$ ,

$$\frac{d}{dt} M(\mathbf{r}, t) = \frac{d}{dt} M_x(\mathbf{r}, t) + i \frac{d}{dt} M_y(\mathbf{r}, t) \quad (2.27)$$

$$= -\gamma i (\mathbf{G}(t) \cdot \mathbf{r} M(\mathbf{r}, t) - M_0(\mathbf{r}) B'_{1xy}(t)), \quad (2.28)$$

where  $B'_{1xy} = B'_{1x} + iB'_{1y}$ . Assuming that  $M(\mathbf{r}, 0) = 0$  and that the excitation takes place between  $t = 0$  and  $t = T$ , the solution of this first order linear equation at the end of the excitation is:

$$M(\mathbf{r}, T) = i\gamma M_0(\mathbf{r}) \int_0^T B'_{1xy}(t) e^{-i\gamma \int_t^T \mathbf{G}(\tau) \cdot \mathbf{r} d\tau} dt. \quad (2.29)$$

The  $k$ -space interpretation can be made evident by letting:

$$\mathbf{k}(t) = \frac{\gamma}{2\pi} \int_t^T \mathbf{G}(\tau) d\tau \quad (2.30)$$

Thus, we obtain for the transverse magnetization

$$M(\mathbf{r}, T) = i\gamma M_0(\mathbf{r}) \int_0^T B_{1xy}(t) e^{-i2\pi\mathbf{k}\cdot\mathbf{r}} dt \quad (2.31)$$

$$= i\gamma M_0(\mathbf{r}) \int_{\mathbf{k}(0)}^0 B_{1xy}(t) \left| \frac{dt}{d\mathbf{k}} \right| e^{-i2\pi\mathbf{k}\cdot\mathbf{r}} d\mathbf{k}. \quad (2.32)$$

### 2.1.10 Signal-to-noise ratio

The signal in MRI is determined by the available transverse magnetization, which is itself determined by the equilibrium magnetization, Eq. (2.4), and the pulse sequence parameters.

Noise in MRI primarily comes from two sources [19]. The first source is electrical Johnson noise within the receiving coil and amplifier, which can be kept to a minimum by proper coil and amplifier design and matching. The second source of noise is produced by random Brownian electronic fluctuations inside the sample or subject. For small samples and low frequencies, coil-related noise is more important and coil optimization is essential. In imaging however, where the size of samples can be large and operating frequencies high, subject-related noise dominates. From whichever source it may originate, noise in MRI is considered white (with a constant power spectrum), i.e., the noise energy is the same at all frequencies, and moreover, is independent from the signal. The noise power spectrum, as a function of frequency is given by:

$$N(f) = 4kTR, \quad (2.33)$$

where  $k$  is the Boltzmann's constant,  $T$  the temperature and  $R$  is the resistance of the receiving coil and of the sample. The total noise voltage for a bandwidth BW is then:

$$\text{Noise voltage} = \sqrt{4kTR (\text{BW})} \text{ [volts]}. \quad (2.34)$$

Hence, one way to control the amount of noise measured in an MRI sequence is to change the receiver bandwidth. Since the noise energy is constant for all frequencies, the noise collected is proportional to the square root of the bandwidth.

Signal-to-noise ratio (SNR) is an important measure of image quality and gives an indication of the relative importance of useful signal relative to useless noise. We will use the amplitude SNR defined as:

$$\text{SNR} = \sqrt{\frac{\text{signal energy}}{\text{noise energy}}}. \quad (2.35)$$

Noise in MRI is considered to be normally distributed, of variance  $\sigma^2$ , on both the real and imaginary channels. Thus,

$$\text{SNR} = \sqrt{\frac{\text{signal energy}}{\sigma^2}} = \frac{\text{signal amplitude}}{\sigma}. \quad (2.36)$$

When considering magnitude images, this complex Gaussian noise translates as Rician-distributed noise in regions of the image where signal is present, and Rayleigh distributed noise in background regions.

Because the standard deviation of the Rayleigh distributed noise is  $\sqrt{2 - \pi/2}\sigma$ , the SNR of a magnitude image may be estimated from the background standard deviation  $\sigma_{bk}$  by:

$$\text{SNR} = \frac{\text{signal amplitude}}{\sigma_{bk}} \sqrt{2 - \pi/2}. \quad (2.37)$$

### Effect of imaging parameters on SNR

For a given pulse sequence, the MR image noise is affected by the various image parameters: voxel size ( $\Delta x, \Delta y, \Delta z$ ), matrix size ( $N_x, N_y, N_z$ ) and receiver bandwidth (BW). The simplest way to express SNR, for spin-warp imaging is [34, 80]:

$$\text{SNR} \propto \Delta x \Delta y \Delta z \sqrt{\text{Total readout time}}. \quad (2.38)$$

If  $T_{\text{aq}}$  is the readout duration and  $N_{\text{ex}}$  is the number of excitation sequences averaged to obtain the image, this can be expanded as:

$$\text{SNR} \propto \Delta x \Delta y \Delta z \sqrt{N_y N_z T_{\text{aq}} N_{\text{ex}}} = \Delta x \Delta y \Delta z \frac{\sqrt{N_y N_z N_{\text{ex}}}}{\sqrt{\text{BW}_{\text{pix}}}}. \quad (2.39)$$

The proportionality with respect to the voxel size arises from the fact that the MR signal is proportional to the voxel volume. The proportionality to the square root of the  $N$ 's may be explained by the fact that each voxel being interrogated  $N$  times, the total signal is  $N$  times larger than that of a single measurement while the noise standard deviation is  $\sqrt{N}$  times that of a single measurement<sup>d</sup>. The dependence on the receiver bandwidth per pixel  $\text{BW}_{\text{pix}}$  explained by the constant power spectrum of the noise: the wider the receiver bandwidth, the larger is the noise energy measured. We note that, although the noise is affected by the receiver total bandwidth, the SNR depends only on the bandwidth per pixel.

## 2.2 Distortion in MRI: Theory

Distortion in MRI is a well known phenomenon. The various factors that may induce distortion are typically divided into two main classes [69, 5]: machine-dependent and subject-dependent factors. In any case, distortions are the result of any factor that cause the spatial position of a spin to be erroneously encoded.

### 2.2.1 Machine-Dependant factors

These are the distortion factors attributed to imperfections of the imaging device. Although these were quite significant in the early days of MRI, they have become less

<sup>d</sup>We recall that for independent noise values, the variances add instead of the standard deviation. For instance, for  $n_1$  and  $n_2$  two normally distributed random variables,  $\text{var}(n_1 + n_2 + \dots + n_N) = \text{var}(n_1) + \text{var}(n_2) + \dots + \text{var}(n_N)$

of a problem nowadays with the advances in hardware design technology. Moreover, the subject-independent nature of these effects render them predictable and easily measurable and, in certain case, it is possible to compensate for such problems using techniques established [42].

### **Static $B_0$ field inhomogeneity**

The static  $B_0$  field is typically produced by a coil of super-conducting material. Because of the limited physical dimensions of such a coil and manufacturing imperfections, the magnetic field produced is not perfectly uniform [19]. Furthermore, current fluctuations within the coil induce time-varying variations of the main magnetic field. Static field inhomogeneities are typically spatially smooth variations. Note that the distortion caused by  $B_0$  inhomogeneities are proportional to the strength of this static field, and larger effects may be expected for high field (e.g. 3-4 T) imagers.

### **Gradient field spatial non-linearity**

The spatial encoding of MR images strongly relies upon the assumption that the gradient fields are linear. It has been shown [56, 5] that this may not be the case in general.

It is generally accepted that gradient non-linearity depends on the geometry of the coil only, and consequently, scales linearly with the current flowing through the coil. As will be discussed later, this fact is important for the determination of the effect of gradient field non-linearity on the reconstructed image. It has been experimentally demonstrated that the gradient nonlinearity-induced distortions are essentially independent of the polarity of the phase encoding gradient and of the gradient strength [5].

Gradient non-linearity tends to increase with the distance from the magnet isocen-

tre. In brain MR imaging, the imaged region usually lies in the vicinity of the isocentre, where the effects of gradient non-linearity are likely to be minimized.

Static field inhomogeneities do not have any effect in the phase encoding direction in spin-warp imaging (this will be discussed in further detail later in this chapter), so gradient non-linearity is the main cause of distortions in the phase encoding direction. In EPI, there is no such clear distinction between readout and phase encoding, and gradient non-linearity has an effect in both directions.

Hence, in spin-warp imaging, a technique to estimate the gradient non-linearity is to acquire pairs of images of a reference phantom of known geometry with orthogonal directions of the phase encoding gradient (Fig. 2.8). It is then possible from these two images to determine independently the component of distortion due to gradient field non-linearity and static inhomogeneity [56]. Note that this technique, as it relies on knowing the true geometry of the object with respect of the distorted images, can only be applied to access system-related field imperfections.

More recently, a method for the correction of gradient non-linearity was proposed [63], in which the analytic expression of the gradient field was determined by least-square fitting based on phantom data.

Intrinsic gradient non-linearity is present in many commercial scanners, leading to considerable (but predictable) image distortion. Such distortions are usually corrected by a post-processing “image-warping” algorithm.

### **Eddy currents**

Eddy currents are caused by the rapid switching of the magnetic field gradients, causing currents to be induced in the electrically conductive parts of the MR scanner [11]. These time-variant currents in turn, induce extra time varying gradient fields that add to the one applied, resulting in an effective gradient field different from that

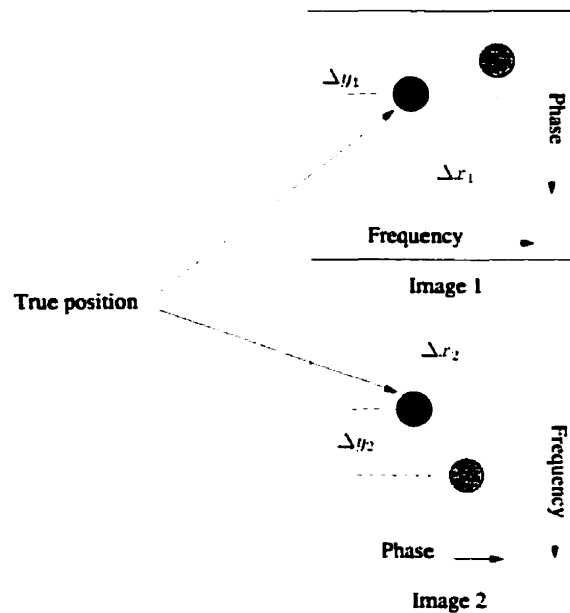


Figure 2.8: Simultaneous measurement of  $B_0$  and gradient errors.

*If two images of the same object of known geometry are acquired with orthogonal directions of readout and phase encoding, it is possible to measure both the static field and the gradient field errors. This assumes however that the underlying true geometry of the object is known.*

expected. Because the induced currents have a direction such as to decrease the rate of change of the magnetic field, the effect of eddy currents is to flatten the effective applied gradient waveform, i.e. to reduce the effective rise time of the gradients. Since eddy currents have a predictable behaviour given a known temporal variation rate of the gradient, they can be measured and a modified gradient waveform that will lead to the desired effective waveform can be derived based on these measurements. Most modern MR imagers are also equipped with actively shielded gradient coils that minimize the effects of eddy currents. The combination of eddy-current compensation and active gradient shielding makes the effects of eddy currents negligible in most situations. Exceptions are reported for imaging techniques involving very fast switching of gradients (e.g. EPI) or particularly strong gradients (e.g. diffusion imaging).

Time varying eddy currents do not generally cause distortion in MR images: instead they cause positioning errors of the points in k-space. The in-plane effect on the reconstructed images when reconstructed with normal 2D-IFT is usually more complex than simple pixel displacement. It has been noted however that eddy-currents may induce distortion of the slice profile [42].

## 2.2.2 Subject-Dependant factors

### Bulk susceptibility effects

The susceptibility effect arises because the magnetic field  $\mathbf{B}$ , which is the physically relevant quantity that determines the precession frequency, is affected by the magnetic properties of the surrounding material [83]. If the nominal magnetic field is  $\mathbf{B}_0$ , the magnetic field  $\mathbf{B}$  experienced by different materials will be:

$$\mathbf{B} = (1 + \chi)\mathbf{B}_0, \quad (2.40)$$

where  $\chi$  is the magnetic susceptibility of the material.

Because the reconstruction process assumes the magnetic field is  $B_0$ , the extra factor  $\chi B_0$  is reflected in the reconstructed image as a geometrical distortion [23, 4, 8]. Hence, the effective magnetic field giving rise to the NMR phenomenon is dependent upon the magnetic susceptibility of the surrounding material. The exact dependency is itself a function of the geometry of the various regions [37, 36]. Several researchers have investigated the susceptibility effects. Shizhe *et al.* [98] used a finite element model of a human head to find the magnetic field distribution based on the solution of Maxwell's equations. Sumanaweera *et al.* [102] present an experimental determination of the susceptibility induced distortions and conclude that, although the effect is negligible at bone-tissue interfaces, it is important near air-tissue interfaces. The spatial variation of the perturbation field caused by susceptibility may be much more rapid than in

the case of those from static  $B_0$  non-linearity. Moreover, various pathologies, such as tumours and haematoma, may generate extra susceptibility effects [26, 113].

Susceptibility effects are not always a nuisance, and can in fact be used as a means of measuring the magnetic susceptibility of materials or substances [51].

### Flow effects

In some applications, including image-based guidance for electroencephalography (EEG) depth electrode placement, it is mandatory to avoid blood vessels. The effect of flow-induced phase shifts has been studied [74] and is well-understood. It is due to the fact that the position of a given spin moves between the encoding of its  $y$ -position and the encoding of its  $x$ -position. In the idealized case where the flow velocity profile is flat, the displacement is uniform across the vessel and a shift of the vessel is observed in the reconstructed image. In more realistic situations, the flow velocity profile is non-uniform (e.g. tends to zero toward the walls of the vessel) and the shape of the vessel is deformed as well.

A number of methods have been proposed to reduce the flow displacement effect. The “offset gradient echo method” [76] uses asymmetrical echoes to reduce the time interval between the phase encoding gradient and the gradient echo. Backward-evolving phase encoding uses a time-variant phase encoding that terminates at a fixed time as close as possible to the readout gradient, providing a constant echo-time. This method is similar to the Kumar-Welti-Ernst technique [59] and consequently leads to distortion in the phase encoding direction due to static field inhomogeneities<sup>e</sup>. Mo-

<sup>e</sup> The Kumar-Welti-Ernst imaging sequence differs from the spin-warp method from the fact that the duration of the phase encoding gradient is varied at each excitation rather than its amplitude. The implication is that static field inhomogeneity causes distortion in the phase encoding direction, as well as in the frequency encoding direction. The spin-warp method does not suffer from the distortion in the phase encoding direction.

ment compensated phase encoding [74] employs a bipolar phase encoding gradient with a large first moment that “extrapolates” the phase that a spin moving at constant velocity should have at the gradient echo centre.

This thesis does not address flow induced distortions and this brief review is included here for the sake of completeness.

### Chemical Shift effect

The Larmor relationship (2.9) links the resonance and the precession frequency of the magnetization arising from an ensemble of nuclei of a given isotope. Beside the intrinsic magnetic property of these nuclei (captured by the gyromagnetic ratio), their chemical environment (e.g. the molecule within which they are situated) has an impact on the observed precession frequency. In magnetic resonance imaging, the signal is primarily generated by hydrogen nuclei present in two chemical environments, water ( $\text{H}_2\text{O}$ ) or fat ( $\text{CH}_2$  groups). The chemical shift appears because the  $^1\text{H}$  nuclei “sees” a different magnetic field depending on the chemical environment to which it belongs (water or fat). This difference is generally described by including a chemical species dependent *screening constant*,  $\sigma$ , in the Larmor relationship:

$$\omega_w = \gamma(1 - \sigma_w)B_0 \quad (2.41)$$

$$\omega_f = \gamma(1 - \sigma_f)B_0, \quad (2.42)$$

where the subscripts w and f refer to water and fat respectively. The chemical shift is defined as the difference between the angular precession rates of the two species:

$$\omega_{cs} = \omega_f - \omega_w = \gamma(\sigma_w - \sigma_f)B_0. \quad (2.43)$$

An important characteristic of the chemical shift is that it is field-dependent as shown by the above equation. Hence, a higher magnetic field gives rise to larger chemical

shifts. Because of this, the chemical shift is often expressed as a relative value in ppm (parts per million),  $\delta_{CS}$ , in order to remove the field dependence:

$$\delta_{CS} = \frac{\omega_f - \omega_w}{\omega_w} 10^6 \text{ [ppm]} = \frac{\sigma_w - \sigma_f}{1 - \sigma_w} 10^6 \text{ [ppm]} \quad (2.44)$$

In MRI, the nominal Larmor frequency is set to that of water protons. This implies that the protons in fat generate a signal which is off-resonance. At 1.5 T, the relative chemical shift  $\delta_{CS}$  between water and fat around  $-3.5$  ppm, which results in an absolute chemical shift  $\omega_{CS}/(2\pi)$  of around  $-220$  Hz. The minus sign indicates that the precession frequency in fat is lower than that in water.

In spin-warp imaging, chemical shift translates into a spatial displacement of pixels containing fat with respect to those containing water. In other words, an image may be considered as a superposition of water and fat images that are shifted with respect to each other. Depending on the bandwidth per pixel, this shift may be on the order of several pixels. For instance, with a bandwidth per pixel of 200 Hz, the shift is of one pixel. In EPI, where the effective bandwidth is much smaller, the shift may be on the order of 10 pixels or more.

The most drastic approach to solve this problem is to saturate the fat signal, usually by a frequency selective binomial pulse, leaving only the water signal in the image. One drawback of this method is that  $B_0$  field inhomogeneities may cause the fat saturation pulse to partially destroy some of the water signal, leading to water signal losses. Increasing the bandwidth per pixel is also effective in reducing distortion but this results in a loss of SNR, as described earlier.

Another approach to reduce the chemical shift artifact is to use the so called *fat nulling* technique that is based on the fact that the T1 relaxation time of fat is different from that of water in most tissues. The technique employs an inversion recovery sequence, where a  $180^\circ$  pulse inverting the magnetization is followed by a  $90^\circ$  pulse. The time between the two pulses is carefully adjusted (around 150 ms at

1.5 T) so that the fat signal is zero at the excitation ( $90^\circ$  pulse), and only the water magnetization is excited into the transverse plane to generate a signal.

Chemical shift may also be used to selectively image water or fat [33]. This may be done by adding and subtracting images acquired with different echo times. If the echo time difference is such that the phases of water and fat are  $180^\circ$  from one another at readout time, the addition of the two images will give a water image, and their subtraction will give a fat image. This simple method may not work in the presence of static field inhomogeneities, but other more complicated methods involving more acquisitions allow water and fat to be separated in such non ideal conditions [46, 45].

In brain imaging, fat is normally only present near the skin and in the region of the optic tracts, so the fat-shift phenomenon is not considered as an important problem for many applications. This thesis does not address distortion caused by chemical shift.

### 2.2.3 Mathematical characterization of distortion

Here we develop the mathematical relationships describing distortion in MRI for the one dimensional case, as it applies to spin-warp imaging. Two situations are discussed: frequency encoding, where the signal is sampled at regular time intervals while a constant readout-gradient is applied, and phase encoding, where each sample is acquired after the application of a fixed duration gradient of varying amplitude.

#### Frequency encoding

We consider static field inhomogeneities  $\Delta B_0(x)$ , (which may arise either from magnet imperfection or from susceptibility effects), and gradient field non-linearities  $\Delta G_x(x)$ .

Extending Eq. 2.12 to account for the spatial variation of the magnetization, the

1-D signal equation may be written:

$$s(t) = \int_x M(x) e^{-i\gamma \int_0^t B(x,\tau) d\tau} dx. \quad (2.45)$$

The magnetic field (excluding  $B_0$ ) at any time is:

$$B(t, x) = (\Delta B_0(x) + G_x x + \Delta G_x(x)x)t \quad (2.46)$$

$$= \left( \frac{\Delta B_0(x)}{G_x} + \left( 1 + \frac{\Delta G_x(x)}{G_x} \right) x \right) G_x t. \quad (2.47)$$

Setting  $k_x(t) = \gamma/2\pi G_x t$ , the signal equation is:

$$s(k_x(t)) = \int M(x) e^{-2\pi i \left( \frac{\Delta B_0(x)}{G_x} + \left( 1 + \frac{\Delta G_x(x)}{G_x} \right) x \right) k_x(t)} dx \quad (2.48)$$

The effect on the reconstructed image may be seen by defining the variable change:

$$x'(x) = x + \frac{\Delta B_0(x)}{G_x} + \frac{\Delta G_x(x)}{G_x} x \quad (2.49)$$

Provided that the inverse mapping  $x(x')$  exists, we obtain

$$s(k_x(t)) = \int M(x(x')) e^{-2\pi i x'(x) k_x} \left| \frac{dx}{dx'} \right| dx' \quad (2.50)$$

$$= \int M(x(x')) e^{-2\pi i x'(x) k_x} \left| \frac{dx'}{dx} \right|^{-1} dx'. \quad (2.51)$$

So, the IFT reconstructed image  $M'(x')$  is

$$M'(x') = M(x) \left| \frac{dx'}{dx} \right|^{-1}, \quad (2.52)$$

showing that an intensity distortion is associated with the geometrical distortion.

### Phase Encoding

In the phase encoding direction, time is not directly involved. We use  $m$  to parameterize the phase encoding step.

$$s(m) = \int M(y) e^{-i\gamma B(m,y)} dy. \quad (2.53)$$

The total magnetic field is

$$B(m, y) = \Delta B_0(y) + (G_y + \Delta G_y(y))ym, \quad (2.54)$$

and setting  $k_y(m) = \gamma/2\pi G_y m$ ,

$$s(k_y(m)) = \int M(y) e^{-i\gamma \Delta B_0(y)} e^{-2\pi i \left(1 + \frac{\Delta G_y(y)}{G_y}\right) k_y y} dy \quad (2.55)$$

and similarly to the previous case,

$$M'(y') = M(y) \left| \frac{dy'}{dy} \right|^{-1} e^{-i\gamma \Delta B_0(y)}, \quad (2.56)$$

where

$$y' = y + \frac{\Delta G_y(y)}{G_y} y. \quad (2.57)$$

As compared to the frequency encoding case, we note that the static field inhomogeneity does not cause geometrical distortion in the phase encoding direction: it merely causes a phase error that is not troublesome when looking at magnitude images. However, the effect introduces intensity errors in inversion recovery images, where the real part of the image data is of interest, or can be problematic when using half Fourier techniques where one unmeasured half of k-space is inferred from the other measured half.

## 2.3 Echo Planar Imaging

Echo-planar imaging (EPI) is an ultra fast imaging sequence allowing images to be acquired in a time on the order of 100 ms. The obvious advantage of performing imaging at such a speed is that most physiological motion can be “frozen”. Unfortunately, this speed advantage may only be achieved at the expense of significant image degradations.

One cause of degradation in EPI images is the phase error introduced by the main ( $B_0$ ) field inhomogeneity along the EPI trajectory. Although this phase error is predictable for a point-object (it increases linearly along the trajectory) it is non linear when the signal comes from different points of the object with different local  $B_0$  values (Fig. 2.9). The most adverse effect of these phase errors is geometrical distortion. These distortions can be troublesome in various applications, including surgical guidance and correlation of functional magnetic resonance imaging (fMRI) data with anatomical information from different sources. In addition to geometrical distortions, we show in Chapter 4 that  $B_0$  inhomogeneity also introduces so-called  $N/2$  ghosting.

Several methods have been suggested to address the distortion problem in EPI images. Some approaches correct distortion directly in image space using a  $B_0$  field map [88] or by using two acquisitions having different polarity of the phase encoding gradient [12]. Other methods apply a phase correction to the k-space data prior to performing normal 2D DFT reconstruction [108, 93]. All of these methods approach the EPI distortion problem on a column-by-column basis, by independent 1D corrections of the EPI image along the phase encoding direction. This 1D processing approach is based on the assumption, which is valid under certain conditions, that the EPI point spread function is one-dimensional.

The single-shot EPI sequence [67], acquires the entire k-space data matrix in one excitation. In the blipped EPI method [87], an oscillating readout gradient is applied, together with the short blipped phase encoding gradient (Fig. 2.10a). If data are sampled only during the constant portion of the readout gradient, the resulting k-space sampling is uniform. When data are acquired during the ramp-up or ramp-down period of the readout gradient, the k-space data resulting from a uniform temporal sampling rate are non-uniform. To obtain uniformly spaced points in k-space, one can

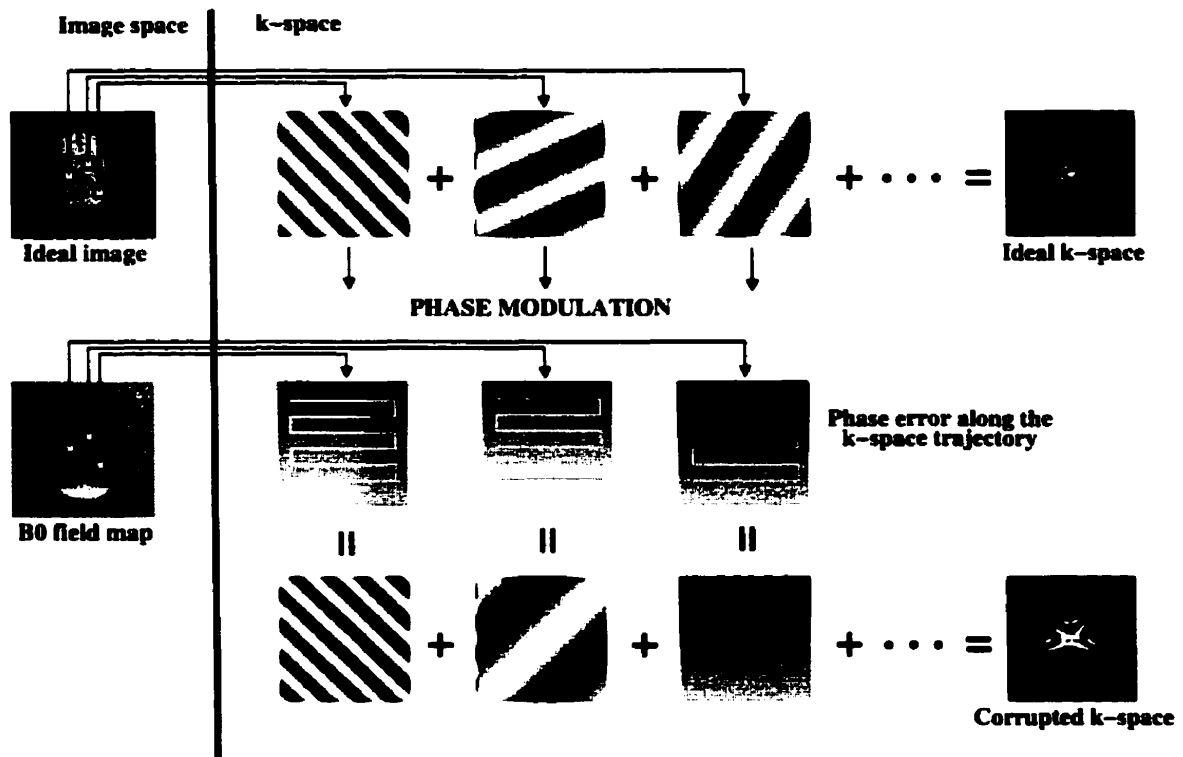


Figure 2.9: The EPI image process.

*Each pixel of an imaged object (called here ideal image) contribute to the total k-space data (top row). However, because of field inhomogeneity each of these contributions is affected by a phase error which depend on the field inhomogeneity and the k-space trajectory (centre row). The corrupted k-space components add up to constitute the total non-ideal k-space data.*

use a non-uniform sampling rate [38] or perform interpolation [13] of the non-uniform data prior to reconstruction by inverse DFT. The EPI sequences discussed in this thesis use the first method (non-uniform sampling rate) so that no interpolation is required. The k-space trajectory is as shown in Fig. 2.10b.

Because the phase variation along the EPI k-space trajectory is much larger in the blipped encoding direction [107], the effect on the reconstructed image can be approximated by distortion in the direction of the blipped encoding. The reason for this is that most of the EPI distortion correction methods work by applying 1D

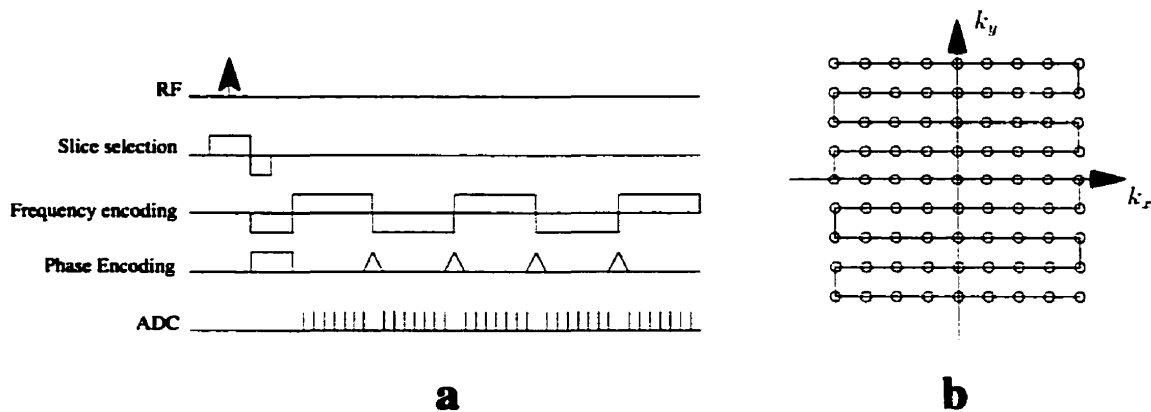


Figure 2.10: The EPI sequence and its k-space trajectory

a) The EPI blipped sequence uses an alternating readout gradient and a so-called “blip” phase encoding gradient. b) K-space trajectory. The alternating readout gradient moves the measurement point back and forth in k-space. The blip gradient ensures that a different  $k_y$  line is measured at each traversal of k-space in the  $k_x$  direction.

corrections to each column of a corrupted EPI image. We will later discuss the implications of this approximation, together with a full 2D correction method of EPI distortions.

This characteristic of EPI images, to be affected by  $B_0$  inhomogeneity mainly in the phase encoding direction, is inverse to the situation found in spin-warp imaging where the distortion affects the readout direction. This can be explained by seeing the k-space trajectory as a long readout gradient being folded in 2D k-space. Even though in EPI the receiver bandwidth is set according to the time length of the readout gradient required to read one line of k-space (as it is the case in 2D or 3D Fourier imaging), one often refers to the EPI *effective bandwidth*, which corresponds to the inverse of the total readout time. The distortion in the phase encoding direction in EPI imaging is directly related to the effective bandwidth. For instance, if the total readout time is 200 ms, the effective bandwidth is  $1/200 \cdot 10^3 \text{s}^{-1} = 5 \text{Hz}$  and a field inhomogeneity equivalent to  $5 \text{Hz}$  will produce a one pixel distortion in the phase

encoding direction, and a 220 Hz chemical shift would result in a pixel displacement of 44 pixels.

## 2.4 Field mapping

Since the primary effect of field inhomogeneity is to induce phase shifts, the most popular method for measuring  $B_0$ -maps is based on phase maps. Several  $B_0$  mapping methods have been proposed [96, 95]. Because phase effects other than those produced by static field inhomogeneity may be present, a difference of the phases of two images acquired with different echo times may be used to obtain the phase variation due only to the static field inhomogeneity. As introduced earlier, one such important effect in in-vivo imaging is the chemical shift caused by fat.

We discuss here the production of field maps using both spin-echo and gradient-echo sequences in the presence of fat.

### 2.4.1 Spin-echo imaging

In spin echo imaging, the  $180^\circ$  refocusing pulse brings the phase of the water signal to zero at time TE. For any other time, the complex signal may be written [46]:

$$I = (\rho_W + \rho_F e^{-i\omega_{cs}\Delta t}) e^{i\gamma\Delta B\Delta t}, \quad (2.58)$$

where  $\rho_W$  and  $\rho_F$  are the proton density of water and fat respectively,  $\omega_{cs}$  is the fat precession angular frequency difference between water and fat ( $\approx -200$  Hz at 1.5 T) and  $\Delta t = t_{GE} - t_{SE}$  is the time difference between the gradient echo and the spin echo.

Consider two acquisitions with time differences of  $\Delta t = \pm\pi/\omega_{cs}$ . The complex signal for each acquisition is:

$$I_{\pm} = (\rho_W - \rho_F) e^{-i\gamma\Delta B\Delta t} \quad (2.59)$$

$$I_+ = (\rho_W - \rho_F) e^{i\gamma\Delta B\Delta t}. \quad (2.60)$$

The phase of the product  $I_-I_+^*$

$$I_-I_+^* = [\rho_W^2 + \rho_F^2] e^{-2i\gamma\Delta B\Delta t}, \quad (2.61)$$

is proportional to the field inhomogeneity  $\Delta B$ .

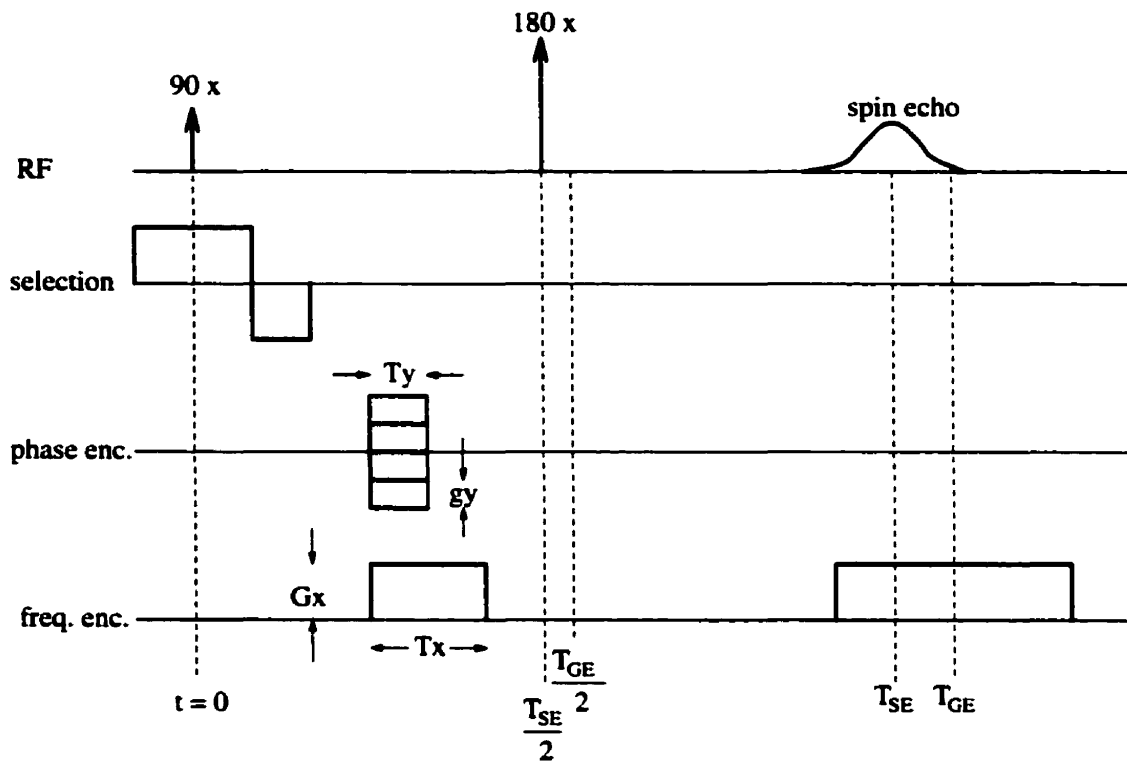


Figure 2.11: Spin-echo sequence with the gradient echo shifted from the spin-echo.

*Normally, the readout gradient is applied so that the centre of the gradient echo corresponds to the centre of the spin echo. By shifting the readout gradient, the centre of the gradient echo does not correspond to the centre of the spin echo, and the spins are not refocused in the centre of  $k$ -space, leaving a  $B_0$  inhomogeneity-dependent phase terms in the image that may be used to determined the  $B_0$  field map.*

## 2.4.2 Gradient echo imaging

In the case of gradient echo imaging, the phase continuously evolves from the time of excitation to the time of readout because no refocusing occurs.

$$I = (\rho_W + \rho_F e^{i\omega_{cs}t}) e^{-i\gamma\Delta Bt}. \quad (2.62)$$

Consider again two acquisitions with TE's of  $t = \text{TE} \pm \pi/\omega_{cs}$ . The complex signal for each acquisition is:

$$I_- = (\rho_W - \rho_F e^{i\omega_{cs}\text{TE}}) e^{i\gamma\Delta B\Delta t} e^{-i\Delta B\text{TE}} \quad (2.63)$$

$$I_+ = (\rho_W - \rho_F e^{i\omega_{cs}\text{TE}}) e^{-i\gamma\Delta B\Delta t} e^{-i\Delta B\text{TE}}. \quad (2.64)$$

The product  $I_- I_+^*$  gives:

$$I_- I_+^* = [\rho_W^2 - \rho_W \rho_F (e^{i\omega_{cs}\text{TE}} + e^{-i\omega_{cs}\text{TE}}) + \rho_F^2] e^{2i\gamma\Delta B\Delta t} \quad (2.65)$$

$$= [\rho_W^2 - 2\rho_W \rho_F \cos(\omega_{cs}\text{TE}) + \rho_F^2] e^{2i\gamma\Delta B\Delta t}. \quad (2.66)$$

Again, because the term in square brackets is real and positive (law of cosines), the phase of this product is proportional to the static field inhomogeneity.

We note that in both cases, the dynamic range of the  $B_0$  map is  $\gamma\Delta B = \pm\omega_{cs}/2 \approx \pm 100$  Hz at 1.5 T.

## 2.4.3 $B_0$ map noise

Since field maps are in fact phase maps, their noise characteristics are quite different from those of magnitude images or complex images. As discussed before, the noise on the real and imaginary channels of an image may be considered to be Gaussian distributed.

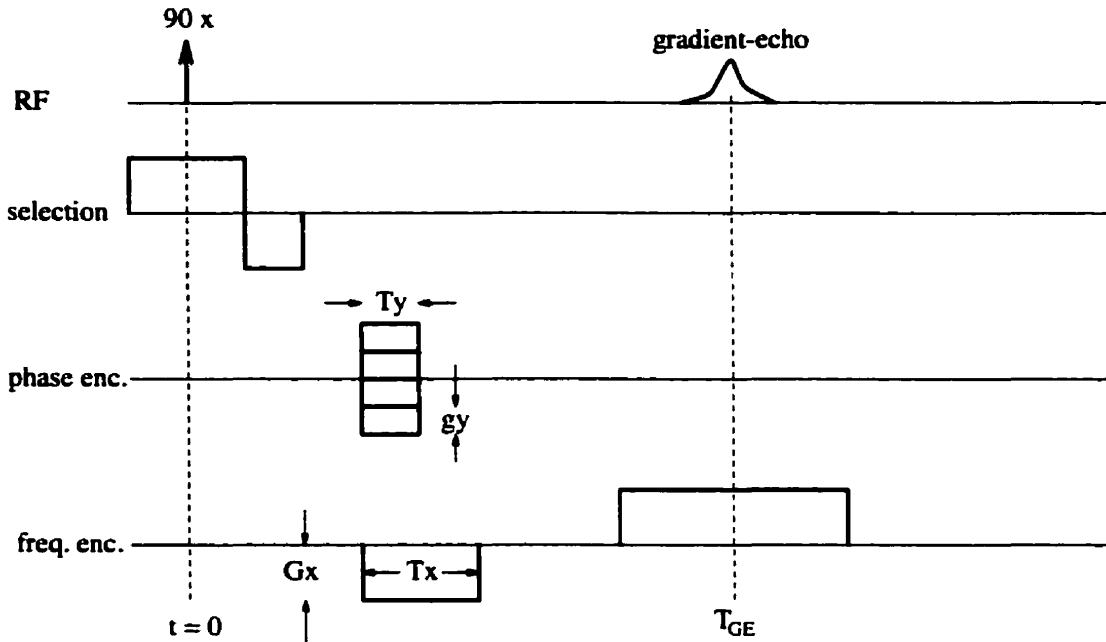


Figure 2.12: Typical gradient-echo sequence.

*In a gradient echo sequence, there is no  $180^\circ$  RF pulse to refocus the dephasing caused by the  $B_0$  inhomogeneity. So, gradient echo images naturally contain phase terms that are related to the  $B_0$  inhomogeneity.*

Consider an image pixel having a real value  $R$ , an imaginary value  $I$  and a noise standard deviation  $\sigma$ . The exact phase noise distribution is quite a complex function but the limiting cases where  $\text{SNR} \rightarrow 0$  and  $\text{SNR} \rightarrow \infty$  are simple [100, 99]:

$$\sigma_\phi = \begin{cases} \pi/\sqrt{3} & \text{SNR} = 0 \\ \sigma/m & \text{SNR} \rightarrow \infty \end{cases} \quad (2.67)$$

where  $\text{SNR} = m/\sigma$  is the magnitude signal-to-noise ratio and  $m = \sqrt{R^2 + I^2}$ . In the first case ( $\text{SNR} = 0$ ) the phase noise is uniformly distributed between  $-\pi$  and  $+\pi$  and in the second case ( $\text{SNR} \rightarrow \infty$ ) it is normally distributed.

This points out the fact that  $B_0$  noise standard deviation essentially depends upon the magnitude data. Furthermore, this means that the  $B_0$  map is meaningless for background regions where the magnitude is completely determined by noise.  $B_0$

map data must be processed in some manner in order to get rid of the meaningless phase map values, i.e. those in the image of the background. One way to do it is to apply a mask on the  $B_0$  map, based on a thresholded version of the magnitude data. Other ways to avoid the non-significant field map values will be considered later.

## 2.5 Iterative Methods for Linear Systems

The core of this thesis consists of considering the MR image distortion problem as a system of linear equations. As stated in the introduction, the only practical methods for solving the large linear systems of equations arising in image restoration problems are the iterative ones. The Conjugate Gradient method is one of them. In this section, the theory underlying the Conjugate Gradient method is briefly discussed.

### 2.5.1 Quadratic Forms

We define  $f$ , the scalar function of the vector  $\mathbf{x}$  by

$$f(\mathbf{x}) = \frac{1}{2}\mathbf{x}^\dagger \mathbf{A}\mathbf{x} - \mathbf{x}^\dagger \mathbf{b} + \mathbf{c}, \quad (2.68)$$

where  $\mathbf{A}$  is an  $N \times N$  matrix, and  $\mathbf{b}$  and  $\mathbf{c}$  are  $N \times 1$  vectors.  $\mathbf{x}^\dagger$  means the Hermitian conjugate, i.e. complex conjugation and transposition, of  $\mathbf{x}$ . If  $\mathbf{A}$  is symmetric, the gradient of  $f$  is given by

$$\Delta f(\mathbf{x}) = (\mathbf{A}\mathbf{x} - \mathbf{b})^\dagger. \quad (2.69)$$

Furthermore, if  $\mathbf{A}$  is positive definite, i.e if

$$\mathbf{x}^\dagger \mathbf{A}\mathbf{x} > 0 \text{ for all } \mathbf{x} \neq 0, \quad (2.70)$$

$f(\mathbf{x})$  is a multidimensional parabola which has a critical point  $\mathbf{x}_m$  satisfying

$$\mathbf{A}\mathbf{x}_m = \mathbf{b}. \quad (2.71)$$

Consequently, finding the minimum of  $f(\mathbf{x})$  is equivalent to solving the linear system

$$\mathbf{Ax} = \mathbf{b}. \quad (2.72)$$

In order to solve (2.72) iteratively, a few definitions are needed.

- The  $n^{\text{th}}$  iteration of the vector  $\mathbf{x}$  is denoted by  $\mathbf{x}_n$ .
- The error  $\mathbf{e}_n$  at the  $n^{\text{th}}$  iteration is
 
$$\mathbf{e}_n \equiv \mathbf{x}_n - \mathbf{x}.$$
- The residual  $\mathbf{r}_n$  at the  $n^{\text{th}}$  iteration is
 
$$\mathbf{r}_n \equiv \mathbf{b} - \mathbf{Ax}_n = -\Delta f(\mathbf{x}_n) = -\mathbf{Ae}_n.$$

### 2.5.2 General search direction: line minimization

The basic element of many iterative techniques is the line minimization, which consists of finding the minimum of an  $N$ -dimensional quadratic form  $f(\mathbf{x})$  along a given direction  $\mathbf{x}_0 + \mathbf{p}$  where  $\mathbf{x}_0$  and  $\mathbf{p}$  are vectors of dimension  $N - 1$ . This solution can be found by finding the value of a scalar parameter  $\alpha$  such that  $f(\alpha\mathbf{p})$  is minimum. This can be done by setting the directional derivative of  $f(\mathbf{x})$  to zero.

$$\frac{\partial}{\partial \alpha} f(\alpha\mathbf{p}) = \Delta f(\alpha\mathbf{p})\mathbf{p} = 0 \quad (2.73)$$

$$(\alpha\mathbf{Ap} - \mathbf{r})^\dagger \mathbf{p} = 0 \Rightarrow \alpha = \frac{\mathbf{r}^\dagger \mathbf{p}}{\mathbf{p}^\dagger \mathbf{Ap}}. \quad (2.74)$$

### 2.5.3 General search direction method

In an iterative context, we consider a set of search directions  $\{\mathbf{p}_0, \mathbf{p}_1, \dots, \mathbf{p}_N\}$ . Starting from an initial value  $\mathbf{x}_0$ , the global minimization proceeds by successive minimizations along the search directions  $\mathbf{p}_i$ .

$$\mathbf{r}_n = \mathbf{b} - \mathbf{Ax}_n \quad (2.75)$$

$$\alpha_n = \frac{\mathbf{r}_n^\dagger \mathbf{p}_n}{\mathbf{p}_n^\dagger \mathbf{A} \mathbf{p}_n} \quad (2.76)$$

$$\mathbf{x}_{n+1} = \mathbf{x}_n + \alpha_n \mathbf{p}_n, n = 0, 1, \dots, N. \quad (2.77)$$

The essential difference between the different iterative methods is in the way the search directions are chosen.

### Steepest Descent Method

In this method, the search directions are chosen to be the residuals. The rationale behind this choice is that, since the residuals are equal to the negative gradient, the search directions are those along which the quadratic form decreases the fastest. The iteration steps of the Steepest Descent Method are then:

$$\mathbf{r}_n = \mathbf{b} - \mathbf{A} \mathbf{x}_n \quad (2.78)$$

$$\alpha_n = \frac{\mathbf{r}_n^\dagger \mathbf{r}_n}{\mathbf{r}_n^\dagger \mathbf{A} \mathbf{r}_n} \quad (2.79)$$

$$\mathbf{x}_{n+1} = \mathbf{x}_n + \alpha_n \mathbf{r}_n, n = 0, 1, \dots, N. \quad (2.80)$$

One feature of this method is that the residual at a given step is orthogonal to that at the next step.

The main drawbacks to this method are that the search directions are not necessarily independent of each other; a given direction may be searched more than once, and the minimization along one given direction can partially be undone by the search in a direction previously taken.

### Conjugate Gradient Method

In the Conjugate Gradient Method, the search directions are chosen in such a way as to minimize the number of searches by avoiding searching the same direction more than once, ensuring that the residual is decreased at each iteration. To achieve this a

set of  $\mathbf{A}$ -conjugate vectors<sup>†</sup> is built-up as the iterations are performed. The algorithm is as follows:

$$\mathbf{r}_0 = \mathbf{b} - \mathbf{A}\mathbf{x}_0 \quad (2.81)$$

$$\mathbf{p}_0 = \mathbf{r}_0 \quad (2.82)$$

$$\left\{ \begin{array}{l} \alpha_n = \frac{\mathbf{r}_n^\dagger \mathbf{r}_n}{\mathbf{p}_n^\dagger \mathbf{A} \mathbf{p}_n} \\ \mathbf{x}_{n+1} = \mathbf{x}_n + \alpha_n \mathbf{r}_n, \\ \mathbf{r}_{n+1} = \mathbf{r}_n - \alpha_n \mathbf{A} \mathbf{p}_n, \\ \beta_{n+1} = \frac{\mathbf{r}_{n+1}^\dagger \mathbf{r}_{n+1}}{\mathbf{r}_n^\dagger \mathbf{r}_n} \\ \mathbf{p}_{n+1} = \mathbf{r}_{n+1} + \beta_{n+1} \mathbf{p}_n \end{array} \right. \quad (2.83)$$

The last two equations of the algorithm update the search vector. Although the final form of this algorithm is simple, its derivation requires a considerable amount of analysis, which is beyond the scope of this section but can be found in [47]. Much of this analysis is to demonstrate that the conjugate directions are mutually  $\mathbf{A}$ -conjugate and that old search directions are not required to derive new search directions satisfying this property.

#### 2.5.4 Normal equations

Because the iterative methods presented above require the system matrix to be symmetric and positive definite, they can be applied to the normal equations related to a general linear systems. The normal equation corresponding to the system  $\mathbf{b} = \mathbf{A}\mathbf{x}$  is:

$$\mathbf{A}^\dagger \mathbf{b} = \mathbf{A}^\dagger \mathbf{A} \mathbf{x}. \quad (2.84)$$

If the matrix  $\mathbf{A}$  is non-singular,  $\mathbf{A}^\dagger \mathbf{A}$  satisfies the properties of symmetry and positive-definiteness. When the matrix  $\mathbf{A}$  is singular,  $\mathbf{A}^\dagger \mathbf{A}$  is non positive definite but the CG

<sup>†</sup> A set  $\{\mathbf{p}_0, \mathbf{p}_1, \dots, \mathbf{p}_{N-1}\}$  are said to be mutually  $\mathbf{A}$ -conjugate when  $\mathbf{p}_i^\dagger \mathbf{A} \mathbf{p}_j = 0$  when  $i \neq j$ .

algorithm may still give useful solutions. Hestenes [49] derives a relation between the conjugate gradient and the pseudo-inverse of a matrix.

The conjugate gradient method is particularly attractive for large sparse linear systems because it uses the system matrix  $\mathbf{A}$  only through multiplication with vectors (even when used with normal equation, the product  $\mathbf{A}^t \mathbf{A}$  never needs to be computed explicitly).

Without going into too much detail in the convergence property of the Conjugate Gradient algorithm, we can say that the number of iterations required to achieve solution is at most equal to the number of distinct eigen-values of the matrix  $\mathbf{A}$  [47, 97]. Hence, in the ideal case where the eigen-values of  $\mathbf{A}$  are all equal, the CG method (and also the Steepest Descent method) would converge in one iteration. This can be explained by noting that, in this case, the multidimensional parabola has a perfect circular symmetry which causes the gradient always to point directly to the minimum point.

In general, the CG method is theoretically guaranteed to converge in at most  $N$  iterations ( $N$  is the dimension of the linear system). In practice however, accumulated roundoff errors cause a gradual loss of orthogonality of the search directions and convergence may not be obtained after  $N$  iterations. In this respect, CG can be considered as a genuine iterative method. Moreover, for large linear systems, it may be impossible to perform even close to  $N$  iterations.

Reports of the use of conjugate gradient methods for deblurring of projection reconstruction MR images were produced by [57] and Man [66], and for EPI imaging distortion correction by Kadah [54].

## 2.5.5 Conjugate Gradient and noise

In any real life situation, random noise may contaminate Eq. (2.71) and the exact solution may not exist. In this situation, the problem may be considered as a least square problem. The conjugate gradient is still useful in these conditions, as it may lead to an approximate solution of the problem.

Figure 2.13 show an example of the behavior the conjugate gradient algorithm in the presence of noise. In such noise contaminated problems, the monotonic decrease of the residual may not correspond to a reduction of the error between the solution vector and the true solution. This behavior is due to the fact that the matrix  $\mathbf{A}$  is usually ill-conditioned, which means that largely differing vectors  $\mathbf{x}_1$  and  $\mathbf{x}_2$  may lead, when multiplied by  $\mathbf{A}$  to nearly equal results  $\mathbf{b}_1$  and  $\mathbf{b}_2$ .

In this thesis, the number of iterations is kept small, and a precise understanding of the effect of noise on the convergence properties of the conjugate gradient method is not as relevant as for other applications where a larger number of iteration are needed in order to achieve an acceptable solution. For instance, in [66], the problem is regularized by replacing the problem (2.84) by:

$$\mathbf{A}^\dagger \mathbf{b} = (\mathbf{A}^\dagger \mathbf{A} - \lambda \mathbf{I}) \mathbf{x}, \quad (2.85)$$

where  $\mathbf{I}$  is the identity matrix of the same size as  $\mathbf{A}$ , and  $\lambda$  is a regularization parameter whose value is selected according to the noise level. As the value  $\lambda$  increases, the approaches the conjugate phase solution.

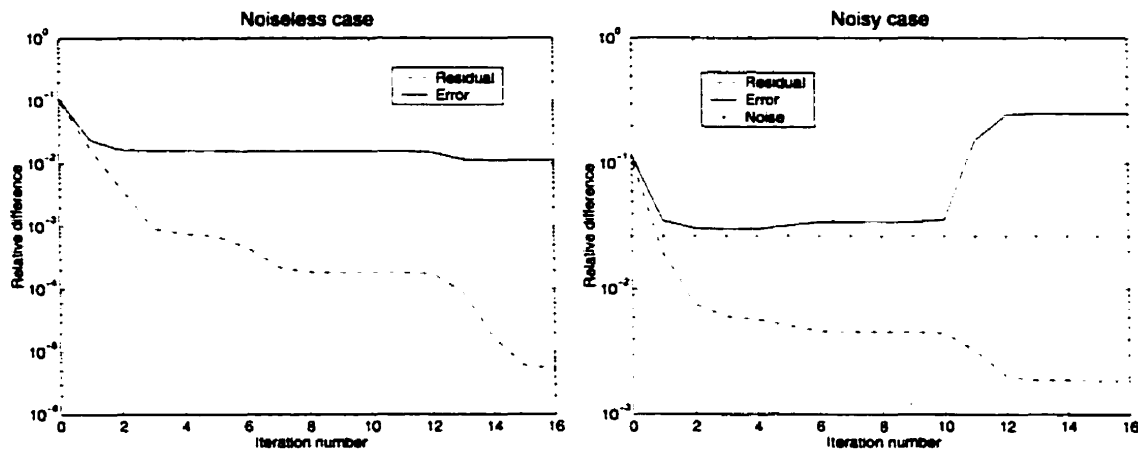


Figure 2.13: Conjugate gradient iterations on noisy data

*Example of the behavior of the residual and error terms in noiseless (left) and noisy (right) situations, for a  $64 \times 64$  system of equation. The residual term is  $\|\mathbf{Ax}_i - \mathbf{b}\|_2 / \|\mathbf{b}\|_2$ , the error term is  $\|\mathbf{x}_i - \mathbf{x}\|_2 / \|\mathbf{x}\|_2$  and the noise term is  $\|\mathbf{n}\|_2 / \|\mathbf{b}\|_2$ , where  $\|\mathbf{v}\|_2$  refers to the 2-norm of the vector  $\mathbf{v}$ , i.e., the square root of the sum of the squared elements of  $\mathbf{v}$ . In both the noiseless and noisy cases, the residual decreases monotonically as the number of iterations increase. In the noiseless case, this reduction of the residual is associated with a reduction of the error term. In the noisy case, on the other hand, the error term may increase even when the residual decreases, due to the ill-conditioned nature of the matrix  $\mathbf{A}$ . The dotted line in the right graph shows the noise level, and illustrates that the error term can never go below the noise level.*

## Chapter 3

# Distortion Correction in MRI

Since the first days of MRI, attempts have been made to address the issue of geometrical distortion. As stated in the previous chapter, the main distortion source is static field inhomogeneity - which may itself be due to machine imperfections or to susceptibility effects - and the deviations of the gradients from linearity. Even though various distortion correction methods have been proposed in the past (e.g. [52]), we will focus in this chapter on those methods that allow the magnetic susceptibility effects to be taken into account.

### 3.1 Post-processing approaches

As in [17], we may distinguish two main categories of distortion correction methods: those that use explicit  $B_0$  map information and those that do not.

### 3.1.1 $B_0$ map based methods

#### Direct implementation of the distortion equation

A number of methods are based on the direct application [93, 94, 39, 78] of the distortion equation (2.52). This is typically performed in two steps. The first step takes care of the geometrical distortion itself, and the second step addresses the associated intensity inhomogeneity. Because these methods are all similar, only one of these approaches, that proposed by Sekihara ([93]) is described in some length here.

First, a linear interpolation is performed to correct for geometrical distortion (fig. 3.1). In one dimension, the geometrically corrected image  $M_d(I)$  is computed with:

$$g = I + \delta(I) \quad (3.1)$$

$$I' = [g] \quad (3.2)$$

$$D = g - I', \quad (3.3)$$

and

$$M_d(I) = (1 - D)M'(I') + DM'(I' + 1). \quad (3.4)$$

$[x]$  indicates the largest integer not greater than  $x$ . Equation (3.1) computes  $g$ , the position of pixel  $I$  due to the field offset.  $I'$ , in Eq. (3.2), represents the index of the pixel in which the center of the distorted falls and  $D$ , from Eq. (3.4) is the fraction the distorted pixel overlaps with the pixel grid. In Eq. 3.4, the geometrically corrected pixel value  $M_d$  is computed as a linear combination of the values of pixels  $I'$  and  $I' + 1$  with weights corresponding to the amount of overlap ( $1 - D$  and  $D$  respectively).

Following this interpolation, the discrete Jacobian is evaluated from the  $B_0$  map data and is applied to the interpolated data to perform density compensation.

$$M(I) = M_d(I)W(I) \quad (3.5)$$

$$W(I) = 1 + \delta(I + 1) - \delta(I), \quad (3.6)$$

where  $M(I)$  is the value of the fully corrected pixel.

This method consists essentially of a discrete implementation of the distortion equation.

Feig et. al. [39] proposed a similar technique with the difference that the phase error was derived from the image itself rather than from a separately acquired field map. This approach did not consider phase variations due to factors other than static field inhomogeneity.

### Geometrical warping

Weis et al. [106] introduced a method based exclusively on geometrical interpolation.

The interpolation used is:

$$L = I - 0.5 + \delta(I - 0.5) \quad (3.7)$$

$$R = I + 0.5 + \delta(I + 0.5) \quad (3.8)$$

$$I'_l = \text{round}(L) \quad (3.9)$$

$$I'_r = \text{round}(R) \quad (3.10)$$

$$D_l = L - (I'_l - 0.5) \quad (3.11)$$

$$D_r = R - (I'_r - 0.5) \quad (3.12)$$

$$n = I'_r - I'_l + 1. \quad (3.13)$$

$L$  and  $R$  are the positions of the left and right edges of the distorted voxel respectively.  $I'_l$  and  $I'_r$  are the indices of undistorted pixel where  $L$  and  $R$  lie.  $D_l$  ( $D_r$ ) is the distance between  $L$  ( $R$ ) and the left side of the pixel  $I'_l$  ( $I'_r$ ). Finally,  $n$  corresponds to the number of undistorted pixels that are “touched” by the distorted one. Fig. 3.2 clarifies the meaning of the different values.

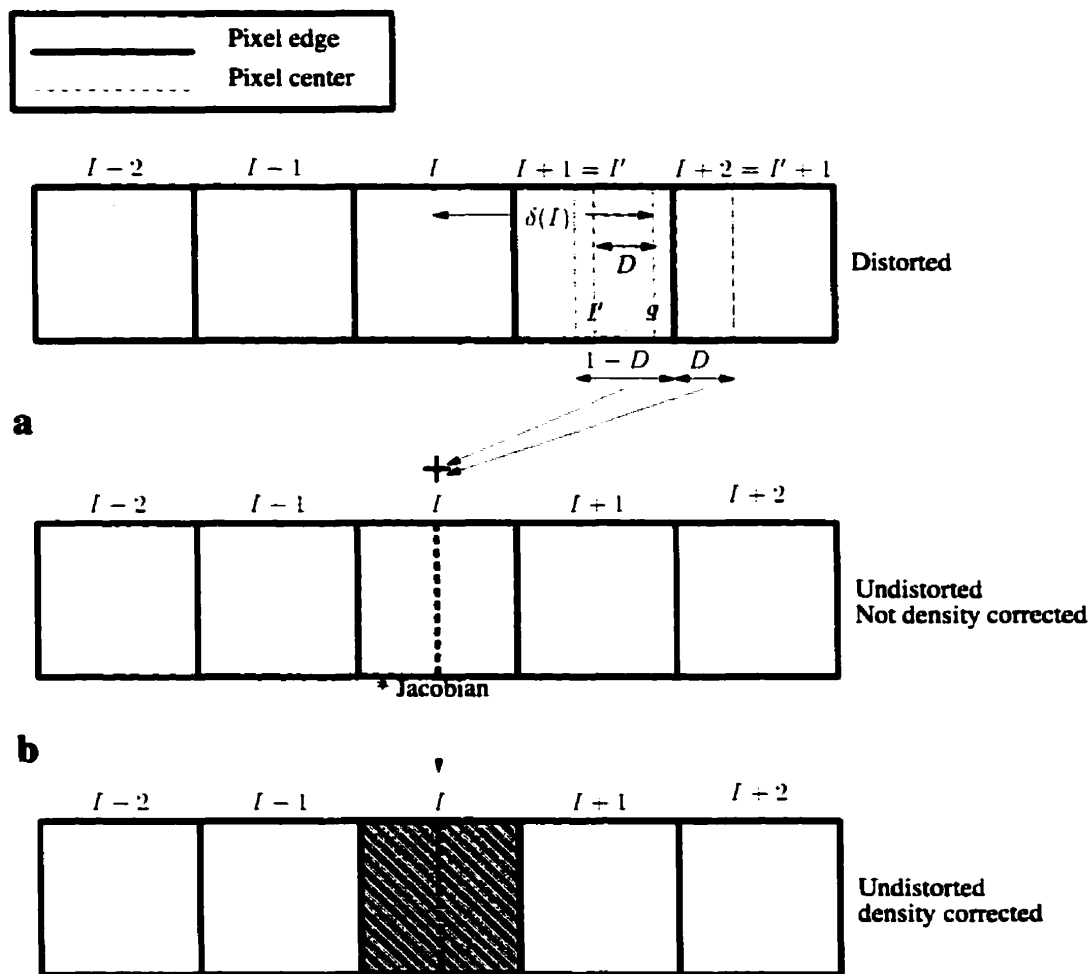


Figure 3.1: Sekihara's geometrical distortion correction method.

The correction is performed in two steps. In the first step, a linear interpolation is performed to displace the distorted pixel to the correct position as determined by the field map (a). Secondly, the resulting corrected pixel value is multiplied by the intensity compensation factor derived from the values of the  $B_0$  map at the pixel of interest and the following pixel. This last term is an approximation of the Jacobian of the coordinate transformation between the distorted and non-distorted image.

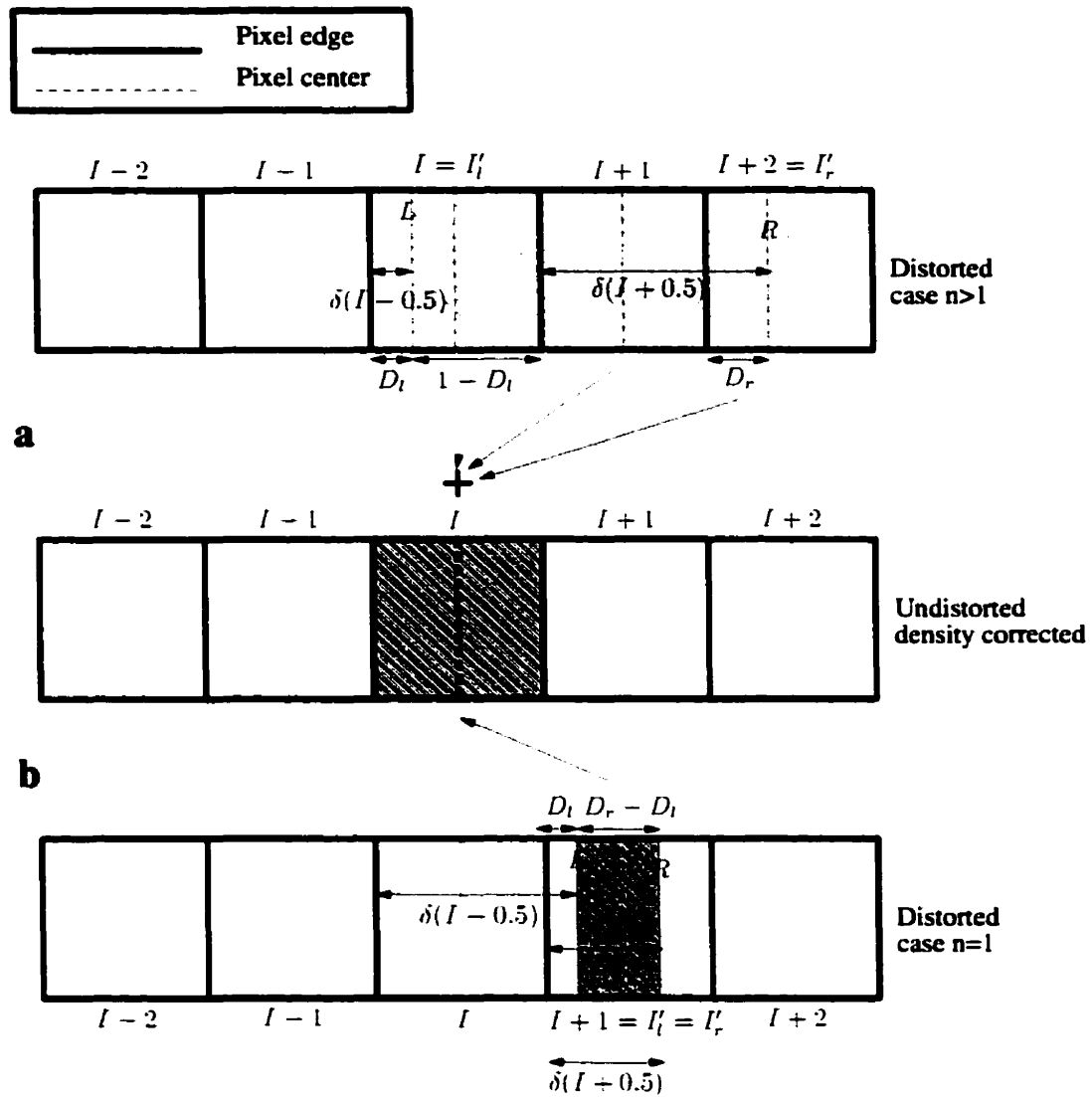


Figure 3.2: Weis's distortion correction method

*In this method, the value of an undistorted pixel is obtained by linear interpolation of the distorted pixel values between the left and the right edge of the distorted pixel. This allows for geometrical and intensity effects to be corrected at once. The algorithm must handle two distinct cases: a) the distorted pixel expands over more than one undistorted pixel and b) the distorted pixel is completely inside an undistorted pixel.*

The value of the undistorted pixel is obtained by the following interpolation:

$$M(I) = \begin{cases} (1 - D_l)M(I'_l) + \sum_{k=I'_l+1}^{I'_r-1} M(k) + D_r M(I'_r) & n > 1 \\ (D_r - D_l)M(I'_l = I'_r) & n = 1 \end{cases} \quad (3.14)$$

The intensity compensation is obtained as a by-product of this equation because this method independently deals with the left and the right edge of a distorted voxel.

One shortcoming of the two methods outlined above is the implicit assumption that the point-spread function is rectangular, i.e. the sinc-like character of the PSF is ignored. Violations of this assumption are small for high resolution imaging, but they become more apparent at low resolution, as is in the case of echo-planar imaging, for instance.

A number of other methods use geometrical interpolation to correct for distortion but they use calibration phantom images to derive a distortion map [90, 92, 91, 53, 24] and model the distortion map as a quadratic function, which may be inaccurate, especially when the inhomogeneity is susceptibility induced.

### k-space phase correction

Weisskoff et al. [108] proposed a correction method – which they apply to EPI images but that may be generalized to other spin-warp imaging – where phase corrects the k-space data, based on the knowledge of the field map. Given a distorted image profile  $M'_m$ , the k-space corrected data  $S_k$  are computed as follows:

$$S_k^w = \sum_{m=0}^{N-1} M'_m e^{-2\pi i k (\frac{m-\delta_m}{N})} \quad (3.15)$$

where  $N$  is the number of points in the profile and  $\delta_m$  is the distortion term (in pixel units) which is proportional the  $B_0$  inhomogeneity obtained from a field map ( $\delta_m = \gamma \Delta B_0 / (2\pi B W_{\text{pix}})$ ). The corrected image profile is obtained by IFT of the corrected k-space data  $S_k^w$ .

Recently, a similar method was proposed, but used reference scans rather than a  $B_0$  map [20].

### Conjugate Phase Reconstruction

Conjugate phase reconstruction [77] consists of “undoing” the unwanted phase variation due to field inhomogeneity. This is equivalent to reconstructing each pixel of an image separately with a demodulation frequency adjusted to the value given by the field map (Fig. 3.3). Mathematically, the conjugate phase corrected profile,  $M_m^{\text{CP}}$ , is given by:

$$M_m^{\text{CP}} = \sum_{k=0}^{N-1} S'_k e^{2\pi i k \left(\frac{m-\delta_m}{N}\right)}, \quad (3.16)$$

where  $S'_k$  is the corrupted k-space data

$$S'_k = \sum_{m=0}^{N-1} M_n e^{-2\pi i k \left(\frac{m-\delta_m}{N}\right)}. \quad (3.17)$$

The conjugate phase method may seem similar to the Weisskoff’s method at first sight, since both are based on phase correction in k-space. The difference can be clarified by comparing equations (3.15) and (3.17). The two equations have the same form except that Weisskoff’s equation involves the distorted, rather than the undistorted image profile and the opposite spatial distortion term ( $-\delta_m$ ) as compared to Eq. (3.17).

### 3.1.2 Double-gradient Methods

The most well known post-processing method that does not use  $B_0$  map information is that proposed by Chang and Fitzpatrick [18, 17]. Consider two images acquired with different readout gradients,  $G_x$  and  $G_x\alpha$ . Because of the relation between readout gradient amplitude and geometric distortion in readout direction, the two images

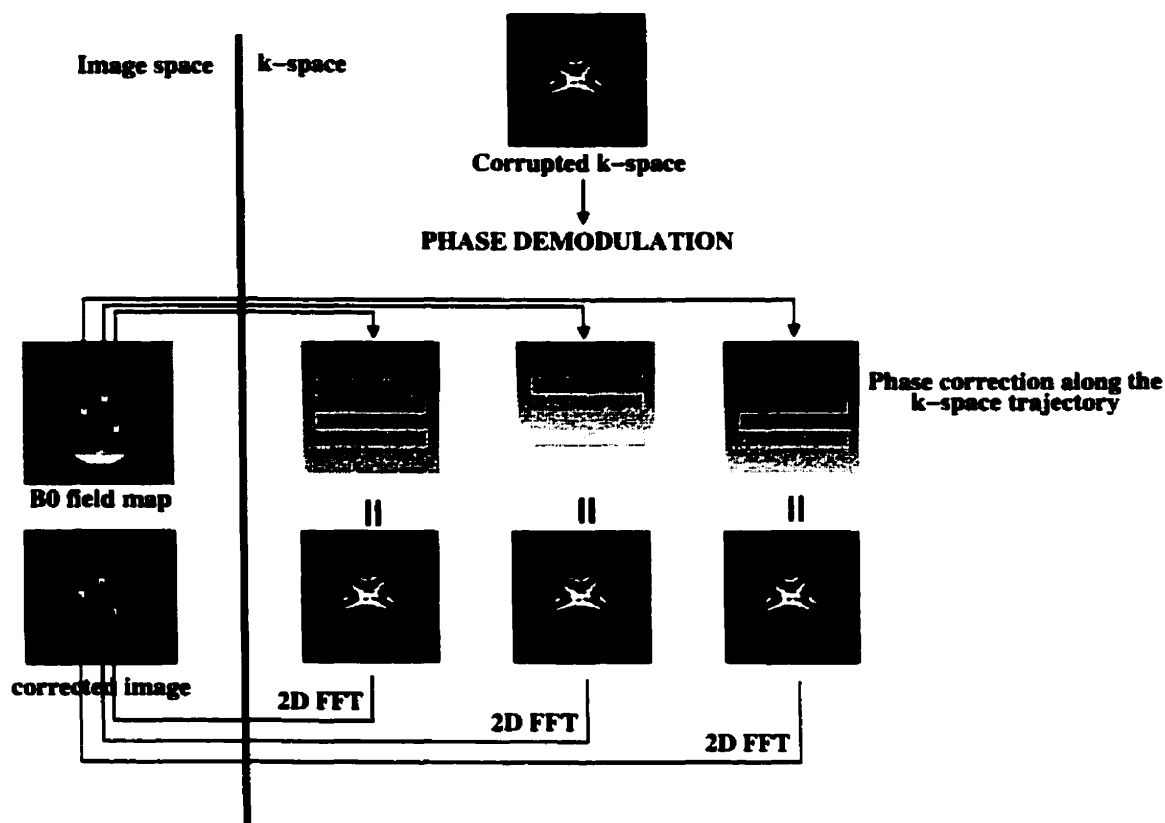


Figure 3.3: Conjugate Phase Reconstruction for an EPI image.

*The conjugate phase reconstruction is equivalent to performing a separate reconstruction for every pixel of an image. Prior to the reconstruction of a given pixel, the k-space data are demodulated with a function dependent on the k-space trajectory and the  $B_0$  inhomogeneity at the pixel position (centre row). For each reconstruction, only the pixel for which the exact demodulation was performed is kept in the final image (bottom row).*

will exhibit different amount of distortion. If  $x'_1$  and  $x'_2$  are the distorted spatial coordinates of each distorted image, and  $x$  is the coordinate system of the undistorted image, following Eq. 2.52, we may write according to Eq. (2.52):

$$M'_1(x'_1) = M(x) \left| \frac{dx'_1}{dx} \right|^{-1} \quad \text{and} \quad M'_2(x'_2) = M(x) \left| \frac{dx'_2}{dx} \right|^{-1}, \quad (3.18)$$

which can be combined as:

$$\frac{dx'_2}{dx'_1} = \frac{M'_1(x'_1)}{M'_2(x'_2)}. \quad (3.19)$$

Provided that at least a pair of corresponding points  $(x'_{10}, x'_{20})$  is known, the above differential equation can be solved to find the correspondence between  $x_2$  and  $x_1$ . Then, from Eq. (2.49),

$$x'_1 = x + \frac{\Delta B_0(x)}{G_x} \quad \text{and} \quad (3.20)$$

$$x'_2 = x + \alpha \frac{\Delta B_0(x)}{G_x}, \quad (3.21)$$

and the solution for  $x$  is:

$$x = \frac{\alpha x'_1 - x'_2}{\alpha - 1}. \quad (3.22)$$

This shows how to get the correction for the pixel displacement. It is intuitively easier to understand Eq. (3.22) when the gradients of the two images have the same amplitude but opposite polarities. In this case,  $\alpha = -1$  and  $x = (x_1 + x_2)/2$ , confirming that the real position is midway between the distorted position  $x_1$  and  $x_2$ .

For the intensity correction, one can take the derivative on both side of Eq. (3.22):

$$1 = \frac{1}{\alpha - 1} \left( \alpha \frac{dx'_1}{dx} - \frac{dx'_2}{dx} \right) \quad (3.23)$$

$$1 = \frac{1}{\alpha - 1} \left( \alpha \frac{M(x)}{M'_1(x'_1)} - \frac{M(x)}{M'_2(x'_2)} \right), \quad (3.24)$$

from which we find:

$$M(x) = (\alpha - 1) \frac{M'_1(x'_1)M'_2(x'_2)}{\alpha M'_2(x'_2) - M'_1(x'_1)}. \quad (3.25)$$

As stated above, an initial condition, a value of  $x'_2$  for which  $x'_1$  is known, is required for the solution of the differential equation (3.19). When the object does not extend over the whole field of view, this is typically achieved by identifying the first point of non-zero intensity on each distorted image, a task that can be performed automatically. In the other case, an arbitrary pair of matching points must be selected, and this usually require human intervention. In any case, the accuracy of the method depends on the accuracy with which the initial starting point is determined.

Moreover, this technique requires two images (or volumes) to achieve correction, hence doubling the acquisition time, making it prohibitively long for 3D imaging and fMRI studies.

An example of the application of this method is reported in [65]. This technique has also been proposed for the correction of EPI images [12]. A variant is presented in [55].

## 3.2 Modified Acquisitions

As opposed to post-processing methods, modified acquisition methods attempt to remove the effect of field inhomogeneities at the acquisition stage, by applying various modifications to the conventional acquisition strategies.

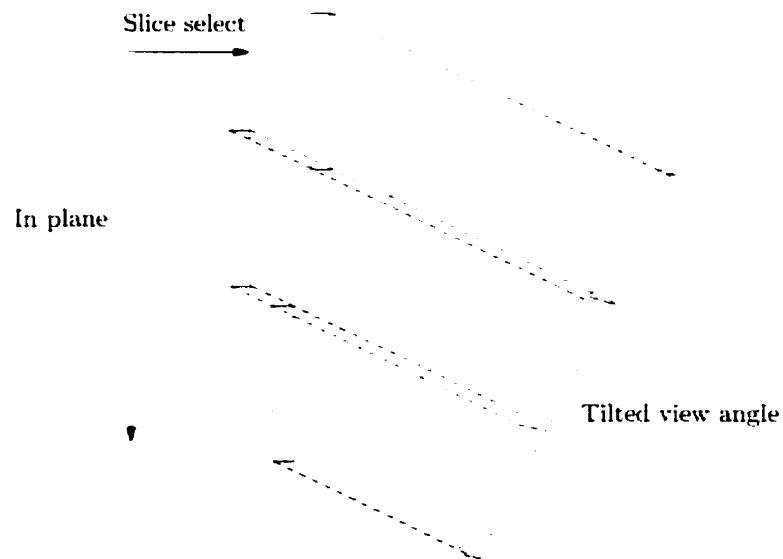


Figure 3.4: Illustration of the Tilted View Angle Technique.

*Because in-plane distortions are associated with proportional slice selection distortions, those distortions appear to vanish when the view angle is tilted. This is practically accomplished by applying a gradient in the slice select direction together with the usual readout gradient when sampling the signal.*

### 3.2.1 View angle tilting

In 1987, Cho et al [21] proposed a method based on view angle tilting. Their technique, applicable to 2D imaging, used the fact that geometrical distortions (including chemical shift) present in the frequency encoding direction are associated with proportional distortion of the slice profile. Then, by reading out the echoes with the slice selection gradient applied together with the frequency encoding gradient, they were able to obtain images free of distortion. This is equivalent to using an effective readout direction that is slightly tilted with respect to the direction of the desired readout gradient (fig 3.4).

In order to see how the distortion can be eliminated with the view angle tilting method, we write the signal equation in one dimension, including the slice selection direction ( $z$ ).

$$S(t) = \int_z \int_x M(x, z) e^{-2\pi i \gamma G_x t (x + \frac{\Delta B(x)}{G_x})} dx dz. \quad (3.26)$$

The heart of the method is to apply a gradient in the  $z$ -direction during signal readout together with the usual readout gradient in the  $x$ -direction.

$$S(t) = \int_z \int_x M(x, z) e^{-2\pi i \gamma G_z t z} e^{-2\pi i \gamma G_x t (x + \frac{\Delta B(x)}{G_x})} dx dz. \quad (3.27)$$

Applying the variable change

$$z = z' - \Delta B(x)/G_z, \quad (3.28)$$

$S(t)$  becomes:

$$S(t) = \int_{z'} \int_x M(x, z' - \Delta B(x)/G_z) e^{-2\pi i \gamma G_z t (z' - \frac{\Delta B(x)}{G_z})} e^{-2\pi i \gamma G_x t (x + \frac{\Delta B(x)}{G_x})} \left| \frac{dz}{dz'} \right| dx dz'. \quad (3.29)$$

Because the Jacobian of the transformation,  $dz/dz'$ , is unity and the terms in  $B(x)$  cancel, we finally find:

$$S(t) = \int_{z'} \int_x M(x, z' - \Delta B(x)/G_z) e^{-2\pi i \gamma G_z t z'} e^{-2\pi i \gamma G_x t x} dx dz'. \quad (3.30)$$

The application of the gradient in the slice select ( $z$ ) direction has the effect of tilting the view angle by  $\theta = \tan^{-1}(G_z/G_x)$ . The cancellation of the field inhomogeneity terms in Eq. 3.29 occurs because a distortion also occurs in the slice select direction and that this distortion is proportional to the distortion observed in the in-plane ( $x$ ) direction.

They also note that the images obtained are convolved with a narrow rect function that depends on the slice-selection bandwidth and the amplitude of the readout gradient. Because of the absence of slice selection in 3D imaging, this method is only applicable to 2D acquisition methods. The application of this technique to EPI would be difficult because two resonating gradients would have to be applied simultaneously.

### 3.2.2 Echo-projection and similar techniques.

A set of mutually similar techniques use an alternating readout gradient together with a train of  $180^\circ$  pulses. In these techniques, one data point is acquired at the centre of each inter-pulse interval (Fig. 3.5). This, ensures that any dephasing of the magnetization due to chemical shift or  $B_0$  inhomogeneity is refocused when data points are sampled, eliminating their effect on the reconstructed image. Combined with this periodic refocusing of the magnetization, the alternating readout gradient produces a k-space coverage which alternates between negative and positive k-space values. But since the effects the field inhomogeneity are eliminated in this type of sequence, the imaged object is assumed to be real, and a one-sided Fourier Transform is performed to reconstruct the signal.

Refocused gradient imaging (Miller et al) [70] and spin-inversion imaging (Wong et al) [109] use sinusoidal gradients while echo projection imaging (Bendel) [7] have been proposed with ramped linear gradients. The main disadvantages of these techniques is that they require high RF power and long imaging times, due to the limit on the sampling frequency achievable imposed by the duration of the  $180^\circ$  pulses.

### 3.2.3 Conclusion

Addressing the problem of field inhomogeneity-induced distortions involves a clear tradeoff between imaging time and post-processing time. Modified acquisition techniques tend to need longer acquisition times, which may not be compatible with certain applications. For instance, in 3D imaging, the acquisition time already approaches the reasonable limit (10-15 minutes for a whole head) and modified acquisition techniques would only make it worse. For dynamic EPI, time resolution constraints also put a limit on the acceptable acquisition time. Longer acquisition times are not only a problem with modified acquisitions methods. Some post-processing technique, such as the double gradient method, require two set of data to be acquired.  $B_0$  map-based methods also involves a increase in total scan time because of the need to measure a field map. But since  $B_0$  inhomogeneities typically have low spatial frequency content, they can be acquired with much smaller resolution than the image to be corrected. In 3D imaging for instance, a  $B_0$  at one quarter of the spatial resolution of the data set to be corrected will be acquired 4 times as fast. The  $B_0$  map measurement overhead is then only 25%.

The processing time is also a concern in distortion correction. Post-processing techniques must also be efficient, considering the large amount of data generated by 3D and dynamic EPI techniques. For instance, consider the computational burden of applying a one-dimensional correction method to a  $256 \times 256 \times 200$  3D volume. The

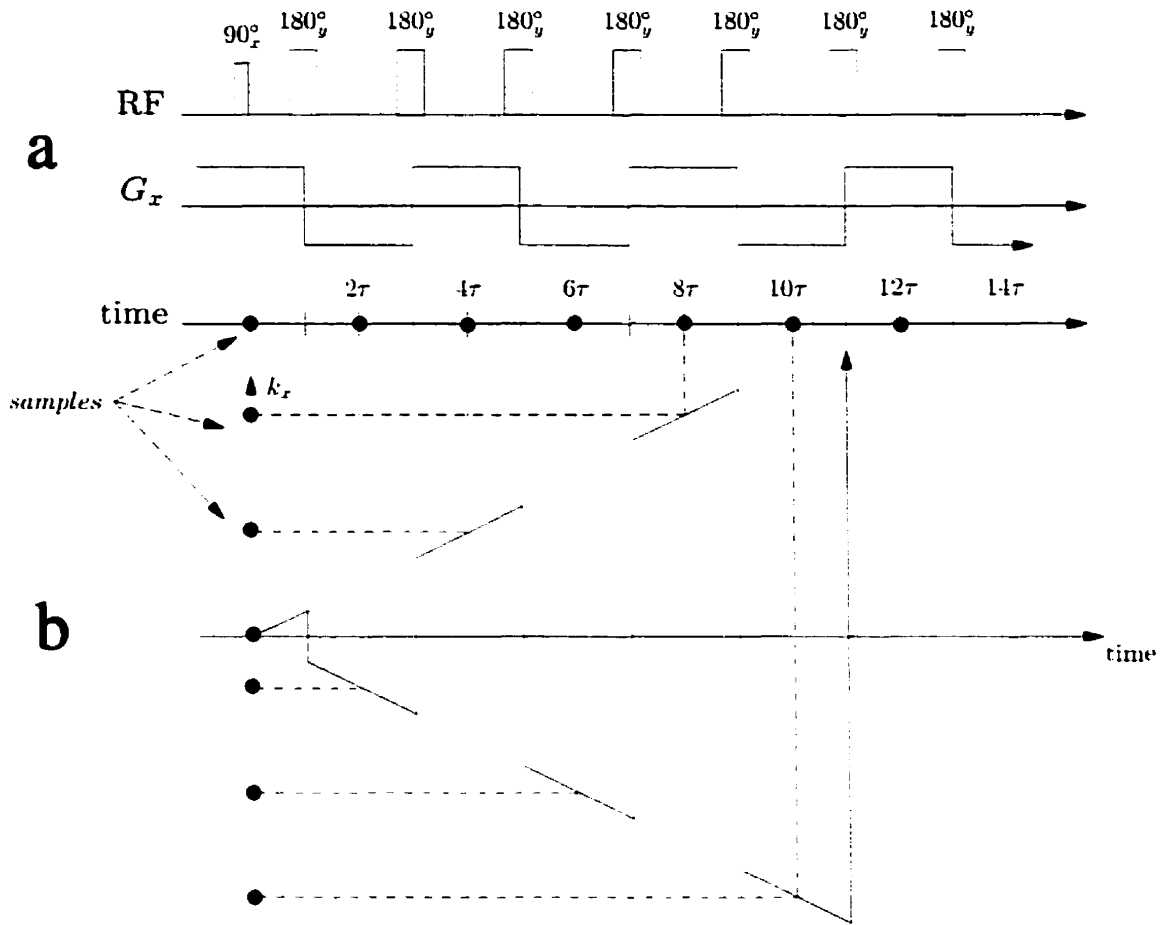


Figure 3.5: Echo Projection Imaging

*The Echo Projection Imaging pulse sequence (a), is composed of a train of  $180^\circ$  RF pulses with an alternating, periodic readout gradient. The periodic refocusing of the magnetization provided by the RF pulse train effectively removes  $B_0$  and chemical shift artifacts from the image, when data points are acquired at  $2\tau$  intervals. The  $k$ -space trajectory (b), alternates between positive and negative  $k$ -space values. Other methods, such as Refocused Gradient Imaging and Spin Inversion Imaging differ from Echo Projection imaging only by the waveform used for the alternating gradient.*

number of line corrections in this case would be  $256 \times 200 = 51200$  (assuming the first dimension is the readout direction). Assuming each line correction takes 1 sec., the total processing time would exceed 14 hours, which is hardly acceptable in a clinical situation. The acceptable processing may obviously vary. In a research context, long

processing times are certainly more common and tolerated than in a clinical context.

Another important point to be considered is the decoupling between the image data and the non ideal conditions giving rise to distortions in the reconstructed images. In the double gradient method no such decoupling occurs. This means that, even for different images acquired with the same conditions of  $B_0$  inhomogeneity, such as a set of dynamic fMRI images, two acquisitions would be needed for each image.  $B_0$  map-based techniques do not have this limitation. The separation between distorted image and non-ideal imaging conditions is the most evident for the inverse problem approach presented in this thesis.

## Chapter 4

# EPI correction as an image restoration problem

This chapter presents a formulation of the distortion correction of EPI images problem from the point of view of image restoration. Parts of this material, was published by the author of this thesis [73] and was the subject of an oral presentation in the Sixth Meeting of the International Society of Magnetic Resonance in Medicine (ISMRM), Sydney, Australia, in April 1998 [72].

As shown in the introduction chapter,  $B_0$ -induced degradations in EPI do not merely translate into geometrical distortions, they also cause some amount of ghosting. Although this ghosting may be small for small levels of  $B_0$  inhomogeneity, it becomes important as the field becomes less homogeneous and is very relevant for practical EPI.

Even if the general principles of image restoration are conceptually straightforward, their practical application is often challenging, due to the potentially large amount of data to be manipulated. In the general case, an  $N \times N$  problem involves a system of linear equations of size  $N^2 \times N^2$ , which may only be manipulated efficiently

if suitable approximations are made to reduce the amount of data to be processed. Another concern when dealing with image restoration problems is the computational complexity of the task. Any algorithm requiring days of computation time would only be of academic interest in a practical situation.

In the following, we discuss the discrete-discrete model of EPI image formation, and we develop approximations allowing solutions to be computed in a reasonable time.

## 4.1 EPI Imaging Equation

In the presence of  $B_0$  field inhomogeneity, the discrete data collected during a 2D MRI acquisition can be expressed as a linear transformation between the ideal  $M \times N$  image  $I_{m,n}$  and the measured signal  $S_{k,l}$  [75]:

$$S_{k,l} = \sum_{m=-\frac{M}{2}}^{\frac{M}{2}-1} \sum_{n=-\frac{N}{2}}^{\frac{N}{2}-1} I_{m,n} K_{m,n;k,l}, \quad (4.1)$$

with,

$$K_{m,n;k,l} = e^{-2\pi i \left( \frac{km}{M} + \frac{ln}{N} + \frac{\gamma}{2\pi} \Delta B_{m,n} t_{k,l} \right)}, \quad (4.2)$$

where  $m$  and  $n$  are the vertical and horizontal spatial indices,  $M$  and  $N$  are the vertical and horizontal image matrix dimensions.  $\Delta B_{m,n}$  is the spatially variant  $B_0$  field inhomogeneity while  $t_{k,l}$  is the time between the sampling of the  $k$ -space point  $(k, l)$  and the RF excitation (when the FID is sampled) or the centre of the echo (when the spin echo is sampled). This last parameter depends on the  $k$ -space trajectory which we assume to be perfect, i.e, the gradient timing and spatial linearity are assumed to be ideal.

Equation (4.1) can be transformed into a relation between the FT reconstructed image  $I'_{m',n'}$  and the ideal image  $I_{m,n}$  by taking the 2D DFT of  $K_{m,n;k,l}$  with respect

to  $k$  and  $l$  on both sides of equation (4.1) for each value of  $m$  and  $n$ . Mathematically,

$$I'_{m',n'} = \sum_{m=-\frac{M}{2}}^{\frac{M}{2}-1} \sum_{n=-\frac{N}{2}}^{\frac{N}{2}-1} I_{m,n} A_{m,n;m',n'}, \quad (4.3)$$

where  $A_{m,n;m',n'} = 2\text{D IDFT}(K_{m,n;k,l})$ , i.e.,

$$\begin{aligned} A_{m,n;m',n'} &= \sum_{k=-\frac{M}{2}}^{\frac{M}{2}-1} \sum_{l=-\frac{N}{2}}^{\frac{N}{2}-1} K_{m,n;k,l} e^{2\pi i \left( \frac{km'}{M} + \frac{ln'}{N} \right)} \\ &= \sum_{k=-\frac{M}{2}}^{\frac{M}{2}-1} \sum_{l=-\frac{N}{2}}^{\frac{N}{2}-1} e^{2\pi i \left( \frac{k(m'-m)}{M} + \frac{l(n'-n)}{N} - \frac{\gamma}{2\pi} \Delta B_{m,n;k,l} \right)}. \end{aligned} \quad (4.4)$$

We note that  $A_{m,n;m',n'}$  is the 2D spatially variant point spread function (PSF) associated with voxel  $(m, n)$ . Depending on the particular form of the point spread function, some simplifications to this equation may be possible. Using integral equation terminology, we refer to  $A_{m,n;m',n'}$  as the *kernel* of the EPI imaging equation.

We show below how this 4D equation can be solved directly using sparse matrices and the conjugate gradient method, leading to a general 2D correction approach. Also, we have demonstrated that the particular form of the EPI kernel will lead to an important simplification of this equation, allowing the 2D problem to be decomposed into a series of 1D problems.

## 4.2 EPI point spread function (PSF)

It is interesting to look at the effect of the phase errors in the EPI imaging process on the reconstruction of a point-object. Consider a point-object  $I_{m_0,n_0} = \delta_{m_0,m} \delta_{n,n_0}$ . From equation (4.3),

$$\begin{aligned} \text{PSF}_{m',n'}^{m_0,n_0} &= \sum_{m=-\frac{M}{2}}^{\frac{M}{2}-1} \sum_{n=-\frac{N}{2}}^{\frac{N}{2}-1} \delta_{m_0,m} \delta_{n,n_0} A_{m,n;m',n'} \\ &= A_{m_0,n_0;m',n'} \end{aligned}$$

$$= \sum_{k=-\frac{M}{2}}^{\frac{M}{2}-1} \sum_{l=-\frac{N}{2}}^{\frac{N}{2}-1} e^{2\pi i \left( \frac{k(m'-m_0)}{M} + \frac{l(n'-n_0)}{N} - \frac{\gamma}{2\pi} \Delta B_{m_0, n_0} t_{k,l} \right)}. \quad (4.5)$$

Fig. 4.1 illustrates the EPI PSF for several different frequency offset values caused by deviation of the main field ( $\Delta B_0$ ) from the nominal value  $B_0$ . Note that the PSF extends in both dimensions and four distinct effects can be observed:

- geometrical distortion, a consequence of the shift of the main peak in the phase encoding direction, which is proportional to the frequency offset. This is seen as the upwards shift of the imaged points in Fig. 4.1.
- blurring in the phase encoding direction, demonstrated by the spread of the main peak. This blurring is a consequence of the fact the sampling grid is not centred on the sinc PSF produced by k-space truncation.
- ghosting in the phase encoding direction, indicated by the presence of a secondary peak, which is increasingly evident as the frequency offset increases.
- blurring of the ghosts, mainly in the frequency encoding direction.

We note that ghosting in EPI may have other causes that can be more significant than the shape of the PSF. One of these factors is the misalignment of the analog to digital conversion (ADC) window with the time varying gradients [14]. A misalignment of even a fraction of the inter-sample spacing can cause significant ghosting of the image. The origin of the  $N/2$ -ghost is due to the fact that ADC misalignment results in a shift of even k-space lines in one direction, and of odd k-space lines in the other direction. Because a shift in k-space translates as a phase modulation in the image space, the images resulting from the odd and even k-space lines of k-space, which are aliased by  $N/2$ , because of undersampling by a factor of 2, are affected by different phase shifts. In a perfect situation, when the ADC is correctly aligned, the

aliases in the odd and even images cancel out completely. But when the two images are affected by different phase shifts, this cancellation does not occur, hence the  $N/2$  ghosts.

An important characteristic of the EPI PSF is that it does not merely shift as the field offset increases due to the presence of the ghosting component. For small field offset, the ghosting component amplitude is only a few percent of the main peak amplitude. However, for larger field offsets, it becomes larger relative to the main peak.

While the PSF is two-dimensional, it can be approximated by a one-dimensional function for small field offsets (e.g.  $< 50$  Hz). This fact will be exploited later to justify 1D processing. A similar 1D analysis was performed in [54].

Another simple way to understand the particular shape of the EPI PSF is to note that an EPI image can be considered as the sum of two images composed of the odd and even k-space lines separately (Fig. 4.2). These images are both aliased over half the FOV and they are distorted in opposite directions in the readout direction. In the real EPI image, being the sum of these two aliased images, the cancellation of the ghosts is not complete because of the different distortions affecting them in the readout direction.

### 4.3 Matrix formulation

In order to solve the 4D imaging equation (4.3), it must be restated in the form of a matrix equation. If  $\tilde{\mathbf{I}}'$  and  $\tilde{\mathbf{I}}$  are the  $MN \times 1$  vectors formed by reformatting  $I'_{m',n'}$  and  $I_{m,n}$  into vectors formed by the concatenation of their columns, i.e:

$$\tilde{\mathbf{I}}_{m+Mn+M/2} = I_{mn} \quad (4.6)$$

$$\tilde{\mathbf{I}}'_{m'+Mn'+M/2} = I'_{m'n'} \quad (4.7)$$

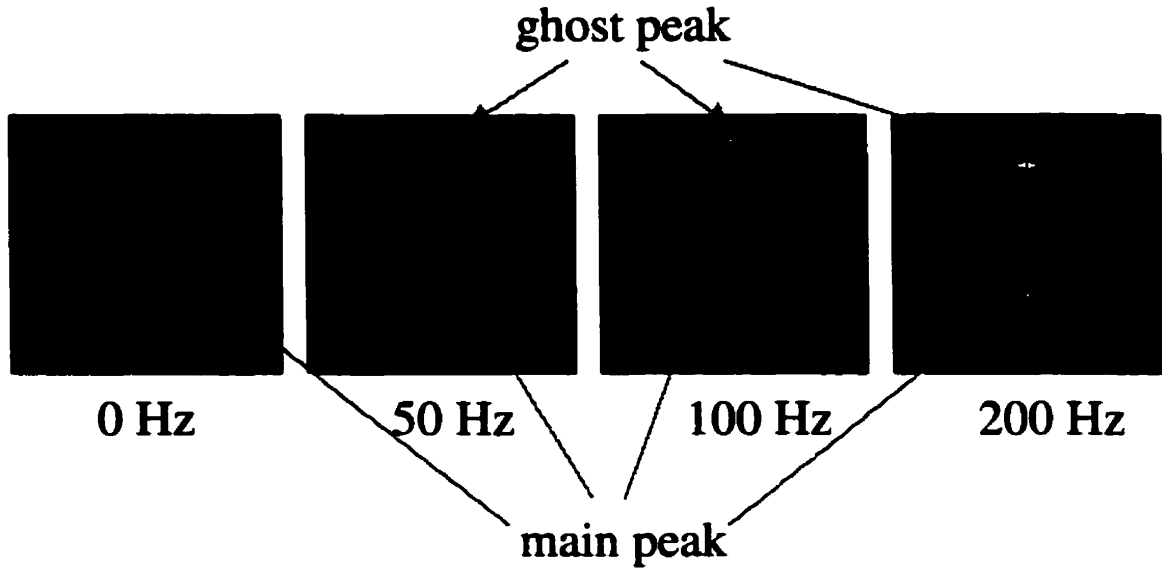


Figure 4.1: The EPI point spread function

The EPI point-spread function is obtained with Eq. (4.5). Here are examples of the PSF for  $B_0$  fields offsets of a) 0 Hz, b) 50 Hz, c) 100 Hz and d) 200 Hz, for an impulse object at the centre of the field-of-view ( $m_0 = n_0 = 0$ ). The EPI parameters are: matrix size =  $128 \times 128$ ,  $TE = 65$  ms,  $T_{acq} = 123$  ms. The horizontal and vertical directions correspond to the frequency and phase encoding directions respectively. The main characteristic of the EPI PSF is the presence of the “ghost” peak alias from the main peak by half the field-of-view. Note how the magnitude of this ghost peak increases as the field offset becomes larger.

$$\bar{\mathbf{I}} = \begin{pmatrix} I_{-\frac{M}{2}, -\frac{N}{2}} \\ I_{-\frac{M}{2}+1, -\frac{N}{2}} \\ \vdots \\ I_{\frac{M}{2}-1, -\frac{N}{2}} \\ I_{-\frac{M}{2}, -\frac{N}{2}+1} \\ \vdots \\ I_{\frac{M}{2}-1, \frac{N}{2}-1} \end{pmatrix} \quad \bar{\mathbf{I}}' = \begin{pmatrix} I'_{-\frac{M}{2}, -\frac{N}{2}} \\ I'_{-\frac{M}{2}+1, -\frac{N}{2}} \\ \vdots \\ I'_{\frac{M}{2}-1, -\frac{N}{2}} \\ I'_{-\frac{M}{2}, -\frac{N}{2}+1} \\ \vdots \\ I'_{\frac{M}{2}-1, \frac{N}{2}-1} \end{pmatrix} \quad (4.8)$$

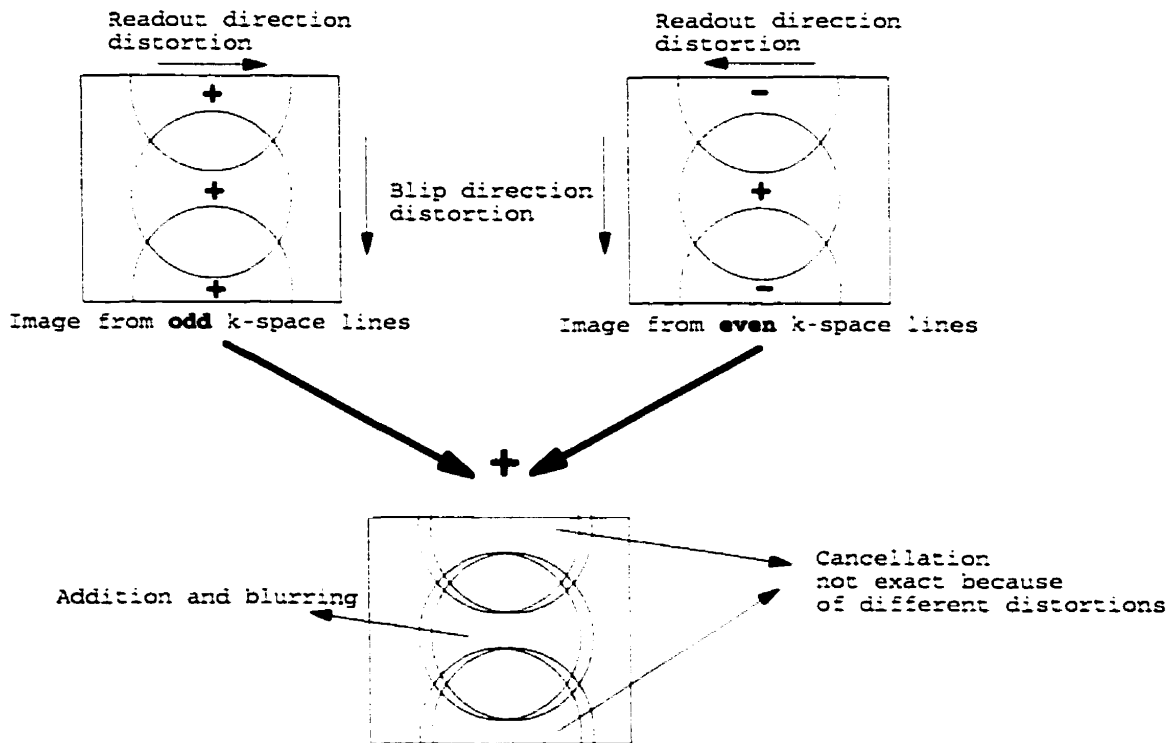


Figure 4.2: Illustration of the origin of field-inhomogeneity related ghosts.

*If only odd or even lines of k-space are reconstructed, an aliased image is obtained. Because of the nature of the EPI trajectory, the distortions in the phase encoding direction is the same for the images reconstructed from odd k-space lines and that obtained from even k-space lines. However, the distortions on the frequency encoding direction are in opposite directions because k-space data are acquired with different polarities of the readout gradient. Because of this, the images do not exactly overlap when added to form the complete EPI image.*

and  $\tilde{\mathbf{A}}$  is the  $MN \times MN$  matrix defined by

$$\tilde{\mathbf{A}} = \begin{pmatrix} A_{-\frac{M}{2}, -\frac{N}{2}; -\frac{M}{2}, -\frac{N}{2}} & A_{-\frac{M}{2}+1, -\frac{N}{2}; -\frac{M}{2}, -\frac{N}{2}} & \cdots & A_{\frac{M}{2}-1, \frac{N}{2}-1; -\frac{M}{2}, -\frac{N}{2}} \\ A_{-\frac{M}{2}, -\frac{N}{2}; -\frac{M}{2}+1, -\frac{N}{2}} & A_{-\frac{M}{2}+1, -\frac{N}{2}; -\frac{M}{2}+1, -\frac{N}{2}} & \cdots & A_{\frac{M}{2}-1, \frac{N}{2}-1; -\frac{M}{2}+1, -\frac{N}{2}} \\ \vdots & \vdots & \vdots & \vdots \\ A_{-\frac{M}{2}, -\frac{N}{2}; \frac{M}{2}-1, \frac{N}{2}-1} & A_{-\frac{M}{2}+1, -\frac{N}{2}; \frac{M}{2}-1, \frac{N}{2}-1} & \cdots & A_{\frac{M}{2}-1, \frac{N}{2}-1; \frac{M}{2}-1, \frac{N}{2}-1} \end{pmatrix}, \quad (4.9)$$

equation (4.3) takes the form of the  $MN \times MN$  linear system:

$$\tilde{\mathbf{I}}' = \tilde{\mathbf{A}}\tilde{\mathbf{I}}. \quad (4.10)$$

This is illustrated in Fig. 4.3. In absence of field inhomogeneity, the matrix  $\tilde{\mathbf{A}}$  is the

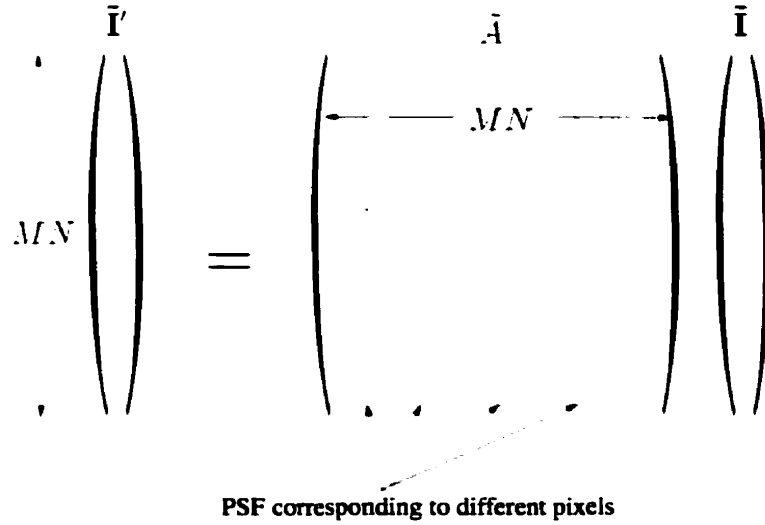


Figure 4.3: The 4D tensor equation in matrix form.

*The 4D tensor equation describing the EPI imaging process may be expressed as a matrix equation where the  $M \times N$  distorted and undistorted images are stretched into  $MN \times 1$  vectors, and the  $M \times N \times M \times N$  4D kernel is re-arranged as a  $MN \times MN$  matrix.*

identity matrix. It is easy to see that with a small amount of inhomogeneity,  $\tilde{\mathbf{A}}$  will be close to the identity matrix and consequently sparse. This can be better appreciated by noting that each column of  $\tilde{\mathbf{A}}$  is the column rescanning [84] of the two-dimensional

EPI point spread function corresponding to one pixel of the ideal image. A look at Fig. 4.1 shows that this vector contains a small number of significant values, and so is sparse to a high degree.

We also note that the geometrical distortion is reflected by a vertical shift of the diagonal elements of the  $\tilde{\mathbf{A}}$  matrix.

### 4.3.1 Low rank approximation of the kernel

Computation of the kernel  $\tilde{\mathbf{A}}$  can be performed by computing the PSF for each pixel of the ideal image. We develop here a practical simplification of the PSF that allows the kernel to be calculated more efficiently.

Because of the particular shape of the EPI k-space trajectory, it is possible to show that the EPI PSF can in fact be approximated very closely by a rank-2 matrix.

In order to see this, we first note that the trajectory itself may be well approximated by a rank 2 matrix. This is because the EPI trajectory is composed of two main trends: the back and forth behaviour produced by the oscillating gradient and the linear motion in the  $k_y$  (phase encoding) due to the blip phase encoding gradient. This is performed as follows.

Let  $\mathbf{U}$ ,  $\lambda$ , and  $\mathbf{V}$  be the singular value decomposition of the trajectory matrix  $\mathbf{t}$ . Because this matrix is typically of rank 2. it can be expressed as

$$\mathbf{t} = \lambda^1 \mathbf{U}^1 \mathbf{V}^{1'} + \lambda^2 \mathbf{U}^2 \mathbf{V}^{2'} \quad (4.11)$$

where  $\mathbf{U}^1$ ,  $\mathbf{U}^2$  and  $\mathbf{V}^1$ ,  $\mathbf{V}^2$  are the first and second singular vectors of  $\mathbf{U}$  and  $\mathbf{V}$  respectively (assuming the singular values and singular vectors are sorted in decreasing order of magnitude.)

The vector  $\mathbf{U}^1$  depends only on  $\mathbf{k}$  and represents the linear time increase along the blip encoding direction. The vector  $\mathbf{V}^1$  has a constant value  $V^1$ .  $\mathbf{U}^2$  alternates

between two values:  $+U^2$  for even k-space lines and  $-U^2$  for odd k-space lines.  $V^2$  represents the ADC sampling along the frequency encoding direction.

The benefit of this formulation is that, when considering odd and even trajectory lines separately, the kernel becomes separable with respect to  $k$  and  $l$ , i.e., the PSF can be computed with three 1D DFT'S instead of one full 2D DFT.

To show this, we write the PSF, for a pixel in the center of the FOV, as a sum of two terms: one over the even k's and the other over the odd k's.

$$\begin{aligned} \text{PSF}_{m,n}^{0,0} &= \sum_{k=-\frac{M}{4}}^{\frac{M}{4}-1} \sum_{l=-\frac{N}{2}}^{\frac{N}{2}-1} e^{2\pi i \left( \frac{2km}{M/2} + \frac{ln}{N} - \frac{\gamma}{2\pi} \Delta B [\lambda^1 U_k^{1e} V^1 + \lambda^2 U^2 V_l^2] \right)} + \\ &e^{2\pi i \frac{m}{N}} \sum_{k=-\frac{M}{4}}^{\frac{M}{4}-1} \sum_{l=-\frac{N}{2}}^{\frac{N}{2}-1} e^{2\pi i \left( \frac{2km}{M/2} + \frac{ln}{N} - \frac{\gamma}{2\pi} \Delta B [\lambda^1 U_k^{1o} V^1 - \lambda^2 U^2 V_l^2] \right)} \end{aligned} \quad (4.12)$$

which may be written

$$\begin{aligned} \text{PSF}_{m,n}^{0,0} &= \sum_{k=-\frac{M}{4}}^{\frac{M}{4}-1} e^{2\pi i \left( \frac{2km}{M/2} - \frac{\gamma}{2\pi} \Delta B \lambda^1 U_k^{1e} V^1 \right)} \sum_{l=-\frac{N}{2}}^{\frac{N}{2}-1} e^{2\pi i \left( \frac{ln}{N} - \frac{\gamma}{2\pi} \Delta B \lambda^2 U^2 V_l^2 \right)} + \\ &e^{2\pi i \frac{m}{N}} \sum_{k=-\frac{M}{4}}^{\frac{M}{4}-1} e^{2\pi i \left( \frac{2km}{M/2} - \frac{\gamma}{2\pi} \Delta B \lambda^1 U_k^{1o} V^1 \right)} \sum_{l=-\frac{N}{2}}^{\frac{N}{2}-1} e^{2\pi i \left( \frac{ln}{N} + \frac{\gamma}{2\pi} \Delta B \lambda^2 U^2 V_l^2 \right)}, \end{aligned} \quad (4.13)$$

where  $U_k^{1o}$  and  $U_k^{1e}$  represent the odd and even elements of  $U_k^1$ .

If we define:

$$\begin{aligned} p_m^1 &= \sum_{k=-\frac{M}{4}}^{\frac{M}{4}-1} e^{2\pi i \left( \frac{2km}{M/2} - \frac{\gamma}{2\pi} \Delta B \lambda^1 U_k^{1e} V^1 \right)} + e^{2\pi i \frac{m}{N}} \sum_{k=-\frac{M}{4}}^{\frac{M}{4}-1} e^{2\pi i \left( \frac{2km}{M/2} - \frac{\gamma}{2\pi} \Delta B \lambda^1 U_k^{1o} V^1 \right)} \\ &= \sum_{k=-\frac{M}{2}}^{\frac{M}{2}-1} e^{2\pi i \frac{km}{M}} e^{-2\pi i \frac{\gamma}{2\pi} \Delta B \lambda^1 U_k^1 V^1} \\ &= \text{IDFT} \left\{ e^{-2\pi i \frac{\gamma}{2\pi} \Delta B \lambda^1 U_k^1 V^1} \right\} \\ p_m^2 &= \sum_{k=-\frac{M}{4}}^{\frac{M}{4}-1} e^{2\pi i \left( \frac{2km}{M/2} - \frac{\gamma}{2\pi} \Delta B \lambda^1 U_k^{1e} V^1 \right)} - e^{2\pi i \frac{m}{N}} \sum_{k=-\frac{M}{4}}^{\frac{M}{4}-1} e^{2\pi i \left( \frac{2km}{M/2} - \frac{\gamma}{2\pi} \Delta B \lambda^1 U_k^{1o} V^1 \right)} \\ &= \sum_{k=-\frac{M}{2}}^{\frac{M}{2}-1} (-1)^k e^{2\pi i \frac{km}{M}} e^{-2\pi i \frac{\gamma}{2\pi} \Delta B \lambda^1 U_k^1 V^1} \end{aligned} \quad (4.14)$$

$$= \text{IDFT} \left\{ (-1)^k e^{-2\pi i \frac{\gamma}{2\pi} \Delta B \lambda^1 U_k^1 V^1} \right\} \quad (4.15)$$

$$\begin{aligned} q_n^1 &= \sum_{l=-\frac{N}{2}}^{\frac{N}{2}-1} e^{2\pi i \left( \frac{ln}{N} - \frac{\gamma}{2\pi} \Delta B \lambda^2 U^2 V_l^2 \right)} + \sum_{l=-\frac{N}{2}}^{\frac{N}{2}-1} e^{2\pi i \left( \frac{ln}{N} + \frac{\gamma}{2\pi} \Delta B \lambda^2 U^2 V_l^2 \right)} \\ &= 2 \sum_{l=-\frac{N}{2}}^{\frac{N}{2}-1} e^{2\pi i \frac{lm}{N}} \cos(\gamma \Delta B \lambda^2 U^2 V_l^2) \\ &= \text{IDFT} \left\{ \cos(\gamma \Delta B \lambda^2 U^2 V_l^2) \right\} \end{aligned} \quad (4.16)$$

$$\begin{aligned} q_n^2 &= \sum_{l=-\frac{N}{2}}^{\frac{N}{2}-1} e^{2\pi i \left( \frac{ln}{N} - \frac{\gamma}{2\pi} \Delta B \lambda^2 U^2 V_l^2 \right)} - \sum_{l=-\frac{N}{2}}^{\frac{N}{2}-1} e^{2\pi i \left( \frac{ln}{N} + \frac{\gamma}{2\pi} \Delta B \lambda^2 U^2 V_l^2 \right)} \\ &= -2i \sum_{l=-\frac{N}{2}}^{\frac{N}{2}-1} e^{2\pi i \frac{lm}{N}} \sin(\gamma \Delta B \lambda^2 U^2 V_l^2), \\ &= \text{IDFT} \left\{ \sin(\gamma \Delta B \lambda^2 U^2 V_l^2) \right\} \end{aligned} \quad (4.17)$$

we get:

$$\text{PSF}_{m,n}^{0,0} = p_m^1 q_n^1 + p_m^2 q_n^2 \quad (4.18)$$

In order to compute the PSF for an arbitrary point  $(m_0, n_0)$ , the equations (4.14) to (4.18) are modified to take the following form:

$$p_m^1 = \text{IDFT} \left\{ e^{\frac{2\pi m_0 k}{N}} e^{-2\pi i \frac{\gamma}{2\pi} \Delta B \lambda^1 U_k^1 V^1} \right\} \quad (4.19)$$

$$p_m^2 = \text{IDFT} \left\{ e^{\frac{2\pi m_0 k}{N}} (-1)^k e^{-2\pi i \frac{\gamma}{2\pi} \Delta B \lambda^1 U_k^1 V^1} \right\} \quad (4.20)$$

$$q_n^1 = \text{IDFT} \left\{ e^{\frac{2\pi n_0 l}{N}} \cos(\gamma \Delta B \lambda^2 U^2 V_l^2) \right\} \quad (4.21)$$

$$q_n^2 = \text{IDFT} \left\{ e^{\frac{2\pi n_0 l}{N}} \sin(\gamma \Delta B \lambda^2 U^2 V_l^2) \right\} \quad (4.22)$$

$$\text{PSF}_{m,n}^{m_0,n_0} = p_m^1 q_n^1 + p_m^2 q_n^2 \quad (4.23)$$

We note that this decomposition actually involves only three 1D DFT's since  $\mathbf{p}^1$  and  $\mathbf{p}^2$  are simply related by a  $N/2$  circular shift. Figs. 4.6 and 4.7 shows an example of these vectors.

An interesting side effect of this decomposition of the kernel is that the first term,  $\mathbf{p}^1\mathbf{q}^1$  represents the main peak of the PSF, while the second term,  $\mathbf{p}^2\mathbf{q}^2$  corresponds to the ghost component.

Figures 4.4 and 4.5 show the singular value decomposition of a typical k-space trajectory and Fig. 4.8 displays the decomposition of a typical EPI PSE into vertical and horizontal components.

## 4.4 Implementation of 2D correction

### 4.4.1 $B_0$ map processing

Since the  $B_0$  map is essentially a phase image, we have seen before that it is affected by full-scale noise in background regions. In other words, the field map is meaningless in the background regions and its value must not be considered in the image correction. However, the field map is generally different from zero in the neighbourhood of the interface between the image and the background. An expeditious way of handling this would be to set the field map to zero in regions where the magnitude image is smaller than a certain threshold value. However, this creates discontinuities in the field map that translate into artifacts in the reconstructed images. An alternative approach is to perform a 2D spline fitting on the field map, where only the meaningful field map values are considered and to let the splines extend over the background region. This produces a  $B_0$  map with the correct value over the regions where there is signal and which is continuous at the object boundaries. Furthermore, such fitting helps to reduce the field map noise.

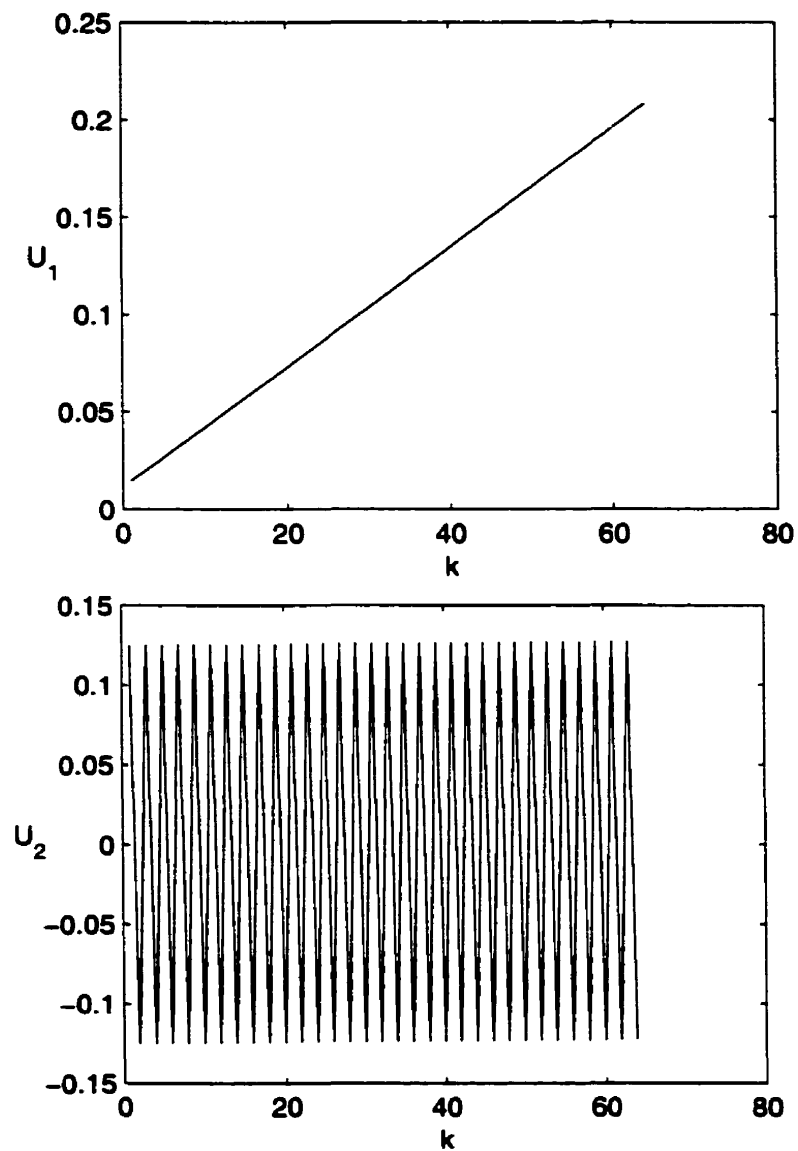


Figure 4.4: Line component of the EPI  $k$ -space trajectory.

*The  $k$ -space trajectory, because of its particular form in EPI, can be approximated by a rank-2 matrix, i.e., it can be expressed as a sum of two outer products  $U_{1k}V_{1l} + U_{2k}V_{2l}$ . This figure shows the components depending on  $k$ , the line index of the trajectory matrix.  $U_1$  accounts for the time increase during the “descent” of  $k$ -space.  $U_2$  describes the fact that the direction of  $k$ -space traversal is alternated at every  $k$ -space line.*

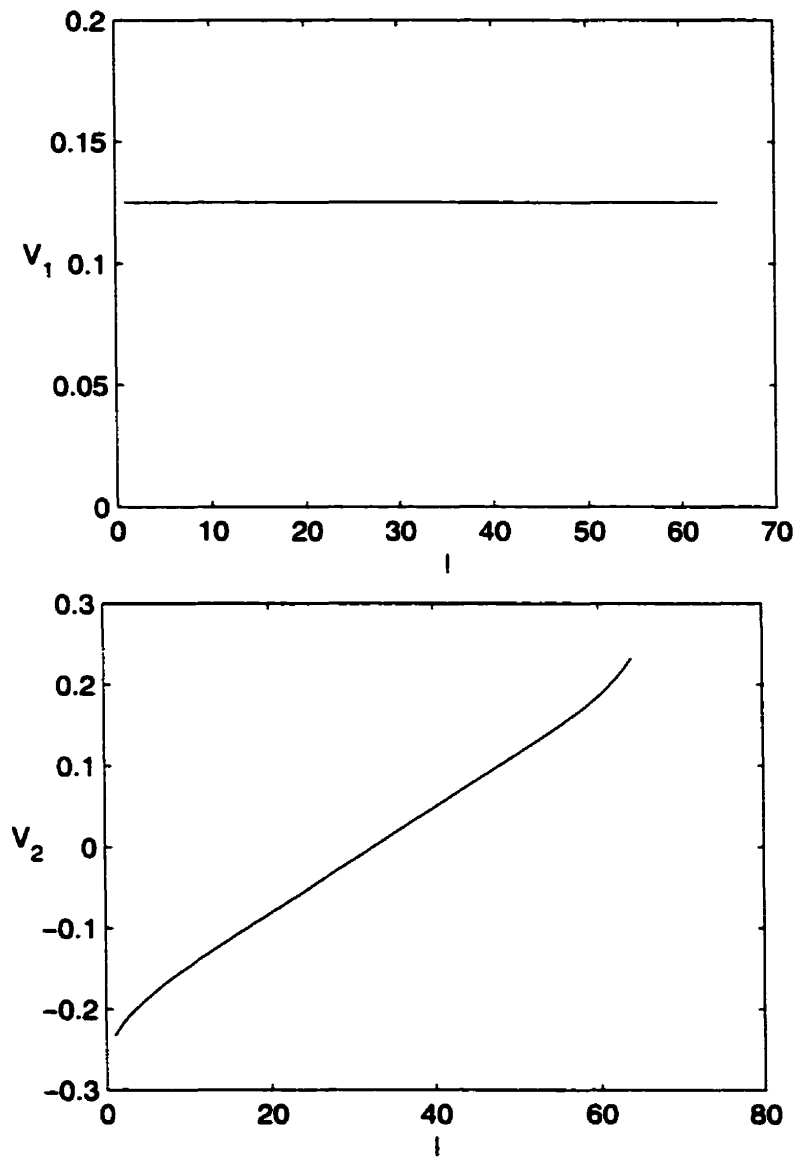


Figure 4.5: Column component of the EPI k-space trajectory.

*This figure shows the components depending on  $l$ , the column index of the trajectory matrix.  $V_1$  is constant, meaning that the phase accrual along any column of the k-space trajectory is the same.  $V_2$  reflects the non-uniform sampling pattern that is used for every line of k-space. The non-uniform sampling is necessary to obtain equally spaced k-space samples when data are acquired in the presence of a non constant readout gradient.*

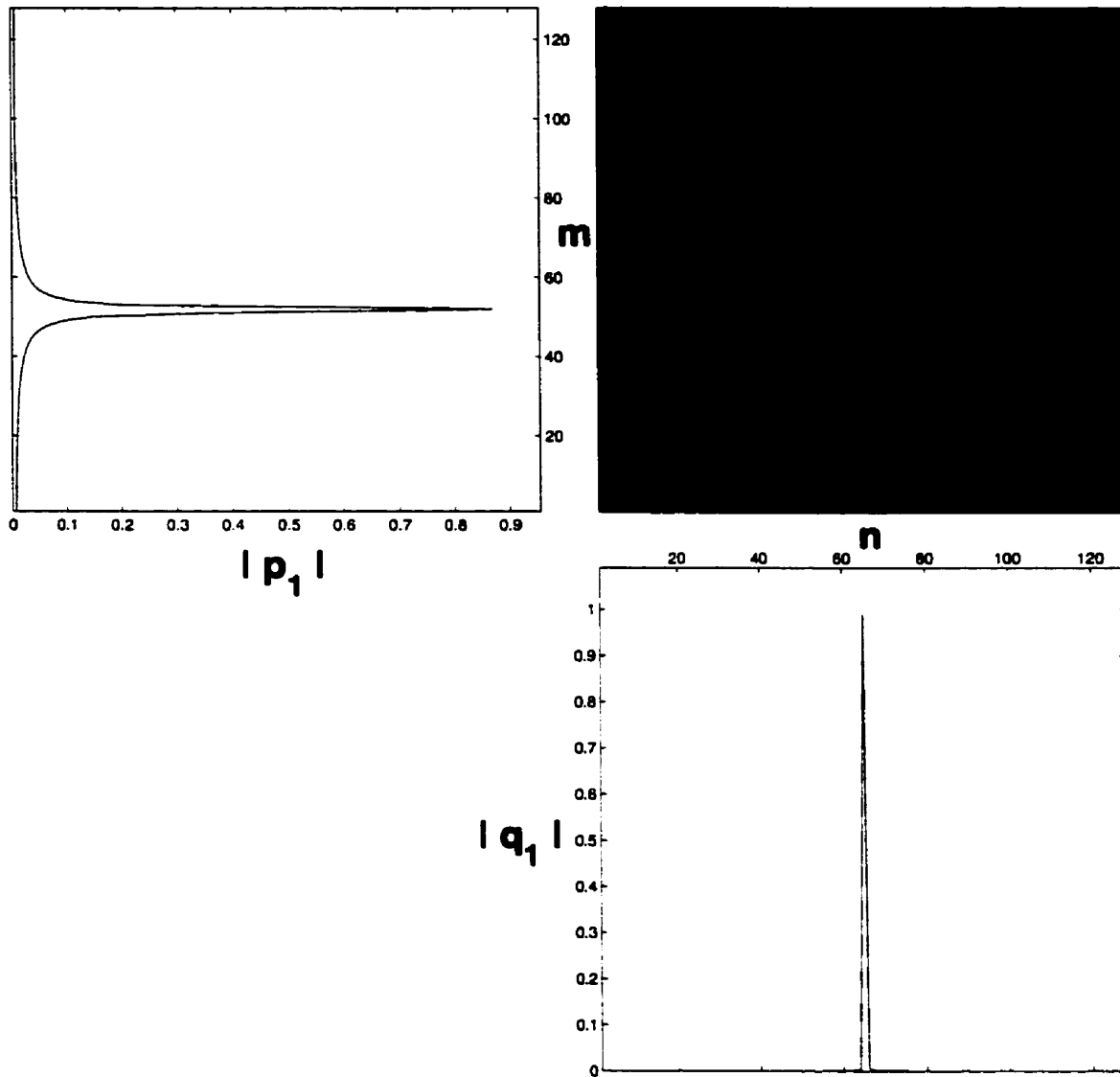


Figure 4.6: Main component of the EPI point spread function.

*Because the  $k$ -space trajectory is a rank-2 matrix, the EPS PSF can be also approximated with a rank-2 matrix (details in the text). The PSF is completely determined by the four vectors:  $\mathbf{p}_{1m}$ ,  $\mathbf{p}_{2m}$ ,  $\mathbf{q}_{1n}$  and  $\mathbf{q}_{2n}$ . The product  $\mathbf{p}_{1m}\mathbf{q}_{1n}$  corresponds to the main component of the PSF, i.e. that which accounts for the distortion in the phase encoding direction.*

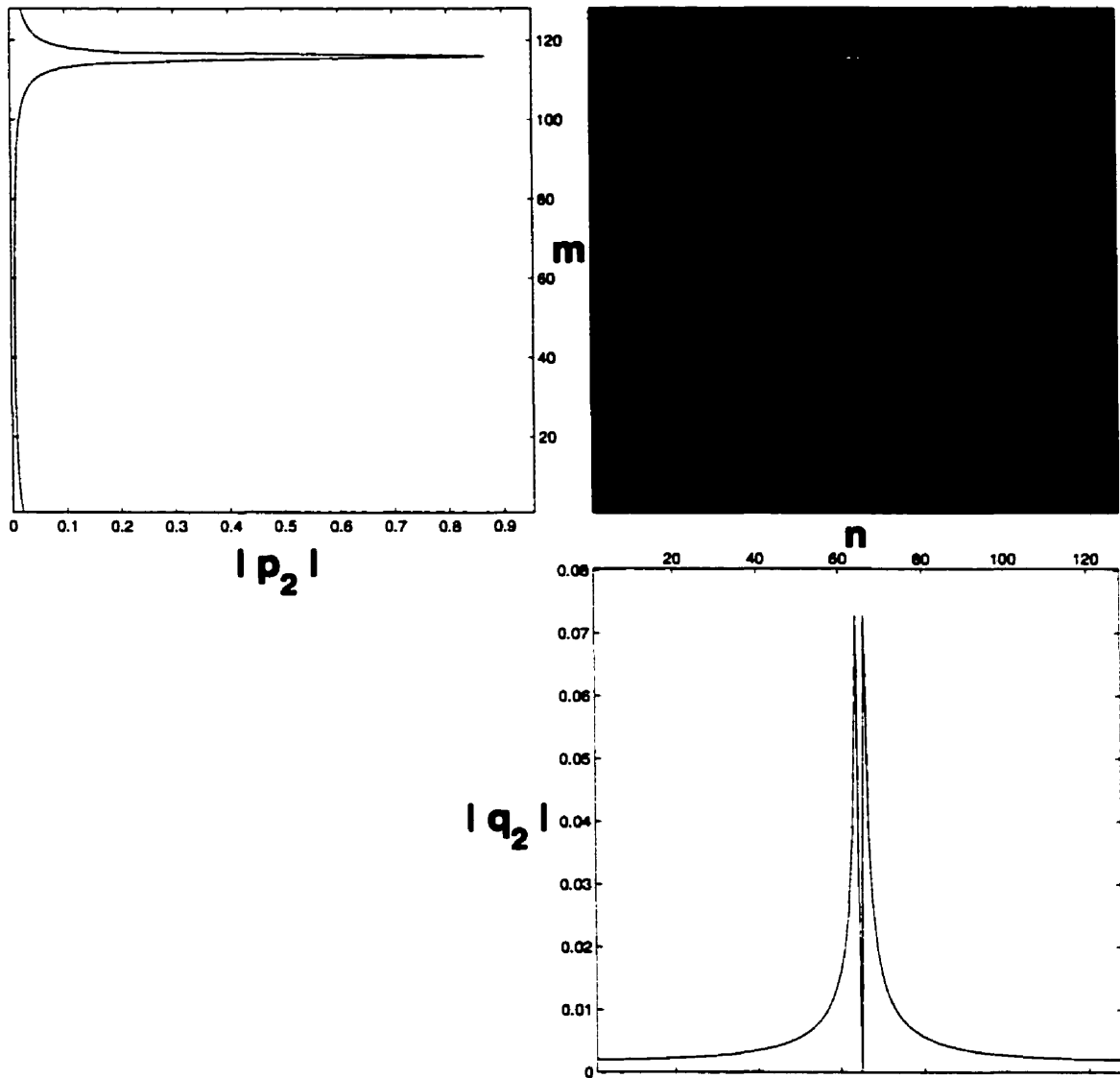


Figure 4.7: Ghost component of the EPI point spread function.

*The product  $p_{2m}q_{2n}$  represents to the ghost component of the PSF, i.e. that which accounts for the  $N/2$  ghost component in the readout direction.*

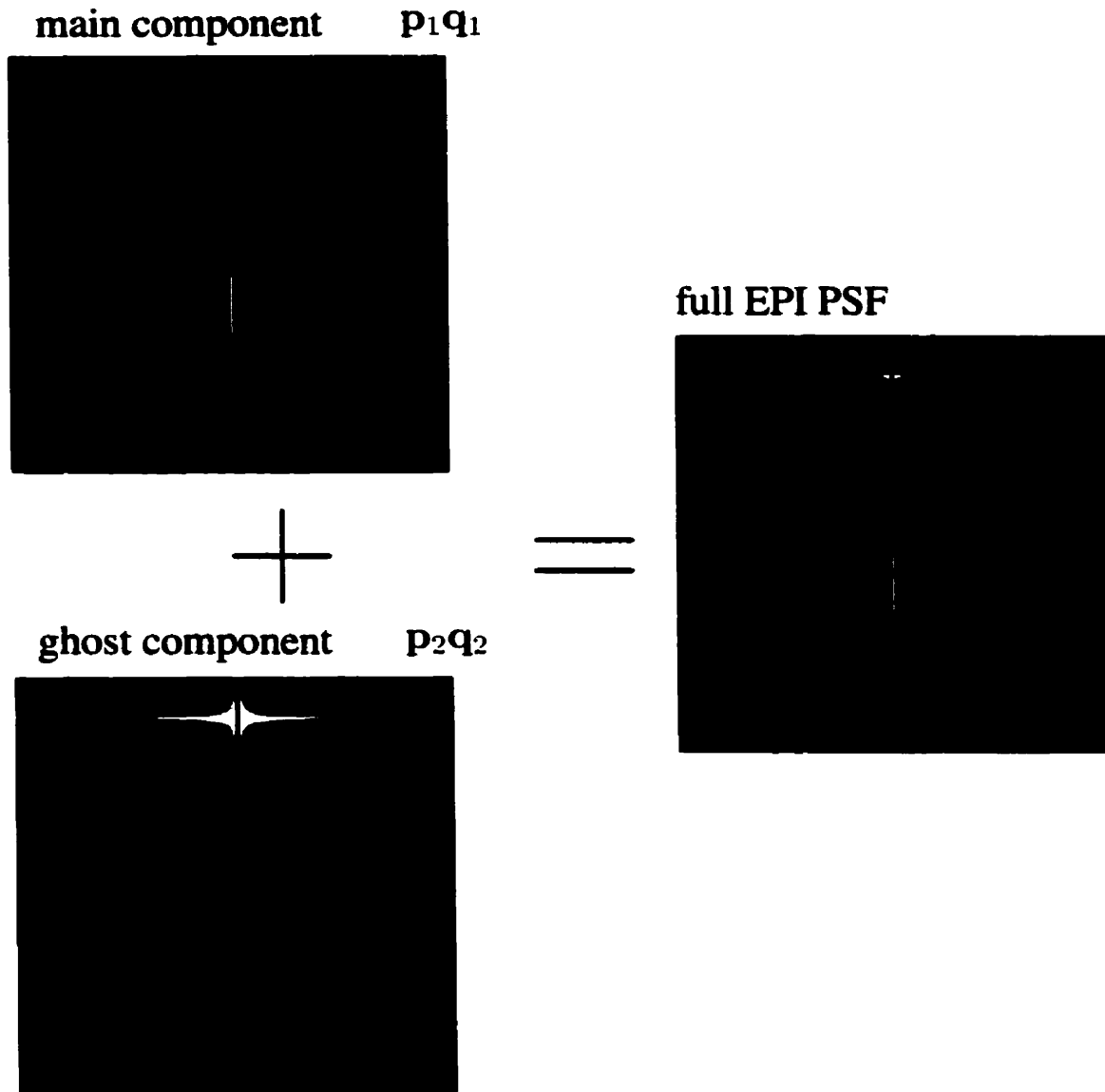


Figure 4.8: The two components of the EPI PSF

*The decomposition of the EPI trajectory allows the EPI PSF to be separated in two components: the main part and the ghost part. The main point in performing this separation is to speed up the computation of the 4D kernel. It may be computed in 3 1D FFTs instead of 1 2D FFT.*

### 4.4.2 4D kernel computation

Since the column of the kernel  $\tilde{\mathbf{A}}$  is formed by the EPI PSF corresponding to a given image location, it was computed column-wise using the rank-2 approximation discussed above. In order to make it sparse, the negligible elements of the PSF, based on a fixed threshold, were set to zero. This threshold, which may be considered as a free parameter of the correction method, allows the sparsity, i.e. the number of non-zero values in the sparse kernel, to be adjusted. The implications of the choice of this threshold will be discussed in the next chapter. The detailed algorithm to compute the 4D kernel is given in Fig. 4.9.

```

compute the matrices  $\mathbf{U}$ ,  $\mathbf{S}$ , and  $\mathbf{V}$ , the SVD of the k-space trajectory.
for ( $i = 0$  to  $N - 1$ )
  for ( $j = 0$  to  $N - 1$ )
    - compute the vectors  $\mathbf{p}^1$ ,  $\mathbf{p}^2$ ,  $\mathbf{q}^1$ ,  $\mathbf{q}^2$  from Eq. (4.19) to (4.22)
    - compute PSF for pixel  $(i, j)$  using Eq. (4.23)
    - reshape the PSF into a column vector
    - discard elements of PSF smaller than threshold
    - store in sparse form in the column  $i + Nj$  of the sparse matrix  $\tilde{\mathbf{A}}$ 
  end for  $j$ 
end for  $i$ 

```

Figure 4.9: Algorithm for the computation of the 4D kernel  $\tilde{\mathbf{A}}$

### 4.4.3 Solution of the 4D linear system

Once the sparse 4D kernel is obtained, the CG method may be applied to the normal equations

$$\tilde{\mathbf{A}}^\dagger \tilde{\mathbf{M}}' = \tilde{\mathbf{A}}^\dagger \tilde{\mathbf{A}} \tilde{\mathbf{M}}, \quad (4.24)$$

where the tilde again refers to the rescanned versions of the 4D kernel and the 2D images. This is done by slightly modifying the standard CG algorithm (2.83) as follows:

$$\begin{aligned} \mathbf{b} &= \mathbf{x}_0 = \tilde{\mathbf{M}}' \\ \mathbf{r}_0 &= \mathbf{A}^\dagger(\mathbf{b} - \mathbf{A}\mathbf{x}_0) \\ \mathbf{p}_0 &= \mathbf{r}_0 \\ \left\{ \begin{array}{l} \mathbf{q}_n &= \mathbf{A}^\dagger \mathbf{A} \mathbf{p}_n \\ \alpha_n &= \frac{\mathbf{r}'_n \mathbf{r}_n}{\mathbf{p}'_n \mathbf{q}_n} \\ \mathbf{x}_{n+1} &= \mathbf{x}_n + \alpha_n \mathbf{r}_n, \\ \mathbf{r}_{n+1} &= \mathbf{r}_n - \alpha_n \mathbf{A} \mathbf{q}_n, \\ \beta_{n+1} &= \frac{\mathbf{r}'_{n+1} \mathbf{r}_{n+1}}{\mathbf{r}'_n \mathbf{r}_n} \\ \mathbf{p}_{n+1} &= \mathbf{r}_{n+1} + \beta_{n+1} \mathbf{d}_n \end{array} \right. \quad (4.25) \end{aligned}$$

We stress again the fact that the matrix  $\tilde{\mathbf{A}}^\dagger \tilde{\mathbf{A}}$  never needs to be computed explicitly, because the product  $\mathbf{q}_n = \mathbf{A}^\dagger \mathbf{A} \mathbf{p}_n$  can be computed as two sparse matrix-vector multiplications, i.e.  $\mathbf{q}_n = \mathbf{A}^\dagger(\mathbf{A} \mathbf{p}_n)$ .

## 4.5 1D correction approximation

The goal of this section is to demonstrate that, under small field inhomogeneity conditions, the 2D correction can be approximated by a series of 1D corrections. A similar

analysis was recently independently reported by Kadah and Hu [54].

The particular form of the EPI PSF suggests that, in the case where field offsets are relatively small, one dimensional processing can be performed on each column of an image. This approximation, conceptually corresponding to the case where the “ghost” part of the PSF is ignored, has many advantages. First, the solution of the large 4D linear system is replaced by a set of smaller and more manageable 2D linear systems.

The 4D tensor equation (Eq. 4.1) can be simplified by making the approximation that  $t_{k,l}$  depends only on  $k$ . Eq. (4.1) then becomes

$$S_{k,l} = \sum_{m=0}^{M-1} \sum_{n=0}^{N-1} I_{m,n} e^{-2\pi i \left( \frac{km}{N} + \frac{ln}{N} + \frac{\gamma}{2\pi} \Delta B_{m,n} t_k \right)}. \quad (4.26)$$

Performing an inverse DFT with respect to  $l$ , we obtain:

$$\begin{aligned} S'_{k,n'} &= \sum_{l=0}^{N-1} \sum_{m=0}^{M-1} \sum_{n=0}^{N-1} I_{m,n} e^{-2\pi i \left( \frac{km}{M} + \frac{l(n-n')}{N} + \frac{\gamma}{2\pi} \Delta B_{m,n} t_k \right)} \\ &= \sum_{m=0}^{M-1} \sum_{n=0}^{N-1} I_{m,n} e^{-2\pi i \left( \frac{km}{N} + \frac{\gamma}{2\pi} \Delta B_{m,n} t_k \right)} \sum_{l=0}^{N-1} e^{-2\pi i \frac{(n-n')l}{N}} \\ &= \sum_{m=0}^{M-1} \sum_{n=0}^{N-1} I_{m,n} e^{-2\pi i \left( \frac{km}{N} + \frac{\gamma}{2\pi} \Delta B_{m,n} t_k \right)} \delta_{n'n} \\ &= \sum_{m=0}^{M-1} I_{m,n'} e^{-2\pi i \left( \frac{km}{M} + \frac{\gamma}{2\pi} \Delta B_{m,n'} t_k \right)}, \end{aligned} \quad (4.27)$$

which can be expressed in matrix form as

$$\mathbf{S}_n = \mathbf{K}_n \mathbf{I}_n, \quad n = 0 \dots N-1, \quad (4.28)$$

where  $\mathbf{S}_m$  and  $\mathbf{I}_m$  are the  $m^{\text{th}}$  column of  $S'_{kn}$  and  $I_{mn}$  respectively and  $\mathbf{K}_n$  is the  $M \times M$  matrix defined by:

$$[K_n]_{km} = e^{-2\pi i \left( \frac{km}{M} + \frac{\gamma}{2\pi} \Delta B_{m,n} t_k \right)}. \quad (4.29)$$

This approximation effectively decouples the  $MN \times MN$  linear system into  $N$  linear systems of size  $M \times M$ .

As in the 4D case, Eq. (4.29) may be expressed in terms of the distorted image by performing a 1D inverse DFT with respect to  $k$  on both sides of the equation, leading to:

$$\mathbf{I}_n = \mathbf{A}_n \mathbf{I}_n, \quad n = 0 \dots N - 1 \quad (4.30)$$

where  $\mathbf{A}_n = \mathbf{F}^\dagger \mathbf{K}_n$ , and  $\mathbf{F}$  is the discrete Fourier Transform matrix  $F_{mn} = e^{-2\pi i \frac{mn}{M}}$ . The  $\dagger$  represents the hermitian transposition (complex conjugation plus transposition).

This recasting of the 2D problem into a series of 1D problems allows us to look at the use of the conjugate gradient method for 1D correction. Because of the simpler form of the 1D problems, analytical expressions for the kernel may be obtained. To show this, we rewrite the matrix  $\mathbf{K}$  in terms of a quantity  $\Delta_m$  which corresponds to the pixel shift in pixel units.

$$K_{km} = e^{-2\pi i \frac{k(m+\Delta_m)}{N}}, \quad k, m = -N/2 \dots N/2 - 1. \quad (4.31)$$

It is useful to adopt the convention that the vectors and matrices are  $-N/2$ -based, i.e., that their first index is  $-N/2$ . The reason for this choice is that  $K_{km}$  does not have the circular symmetry (i.e.  $K_{k+N, m+N} \neq K_{km}$ ) as is the case for the discrete Fourier transform matrix.

The matrix  $\mathbf{A}$  is the Discrete Fourier transform of  $\mathbf{K}$  and can be written:

$$\begin{aligned} A_{m'/m} &= \sum_{k=-N/2}^{N/2-1} K_{km} e^{2\pi i \frac{km'}{N}} \\ &= \sum_{k=-N/2}^{N/2-1} e^{2\pi i \frac{k(m'-m-\Delta_m)}{N}}. \end{aligned} \quad (4.32)$$

An analytical expression for the elements of the matrix  $\mathbf{A}$  can be derived by explicitly performing the inverse DFT: Using the fact that the summation can be expressed as

a geometric progression of the form

$$\sum_{k=0}^{N-1} r^k = \frac{1 - r^N}{1 - r} \quad (4.33)$$

we can write

$$\begin{aligned} A_{m'm} &= e^{-\pi i(m'-m)} e^{\pi i \Delta_m} \frac{1 - e^{2\pi i(m'-m-\Delta_m)}}{1 - e^{2\pi i(m'-m-\Delta_m)/N}} \\ &= e^{-\pi i(m'-m)} e^{\pi i \Delta_m} \frac{1 - e^{-2\pi i \Delta_m}}{1 - e^{2\pi i(m'-m)/N} e^{-2\pi i \Delta_m/N}} \\ &= e^{-\pi i(m'-m-\Delta_m)/N} \frac{\sin(\pi(m'-m-\Delta_m))}{\sin(\pi(m'-m-\Delta_m)/N)}. \end{aligned} \quad (4.34)$$

We may check that when there is no field inhomogeneity,  $\Delta_m = 0$  and Eq. (4.34) gives  $A_{m'm} = \delta_{m'm}$ , i.e. the reconstructed and measured images are related by the identity matrix.

Because of the form of the normal equation 4.24, it is also useful to consider the related problem

$$\mathbf{K}'\mathbf{S} = \mathbf{K}'\mathbf{K}\mathbf{M} = \mathbf{P}\mathbf{M} \quad \text{with } \mathbf{P} = \mathbf{K}'\mathbf{K} = \mathbf{A}^\dagger\mathbf{A}. \quad (4.35)$$

Using a procedure similar to that leading to equations (4.34) it can be shown that the elements of  $\mathbf{P}$  are given by:

$$\begin{aligned} P_{m'm} &= e^{-\pi i(m'-m'+\Delta_{m'}-\Delta_m)} \frac{1 - e^{2\pi i(\Delta_{m'}-\Delta_m)}}{1 - e^{2\pi i(m'-m)/N} e^{2\pi i(\Delta_{m'}-\Delta_m)/N}} \\ &= e^{-\pi i(m'-m'+\Delta_{m'}-\Delta_m)/N} \frac{\sin(\pi(m'-m+\Delta_{m'}-\Delta_m))}{\sin(\pi(m'-m+\Delta_{m'}-\Delta_m)/N)}. \end{aligned} \quad (4.36)$$

The closed form solutions (4.34) and (4.36) allow the matrices  $\mathbf{A}$  and  $\mathbf{A}^\dagger\mathbf{A} = \mathbf{P}$  to be computed directly, without a 2D DFT. Moreover, it has the advantage of allowing the matrix  $\mathbf{A}$  to be obtained efficiently by computing only the elements close to the diagonal.

Fig. 4.10 give an example of how the different matrices may appear.

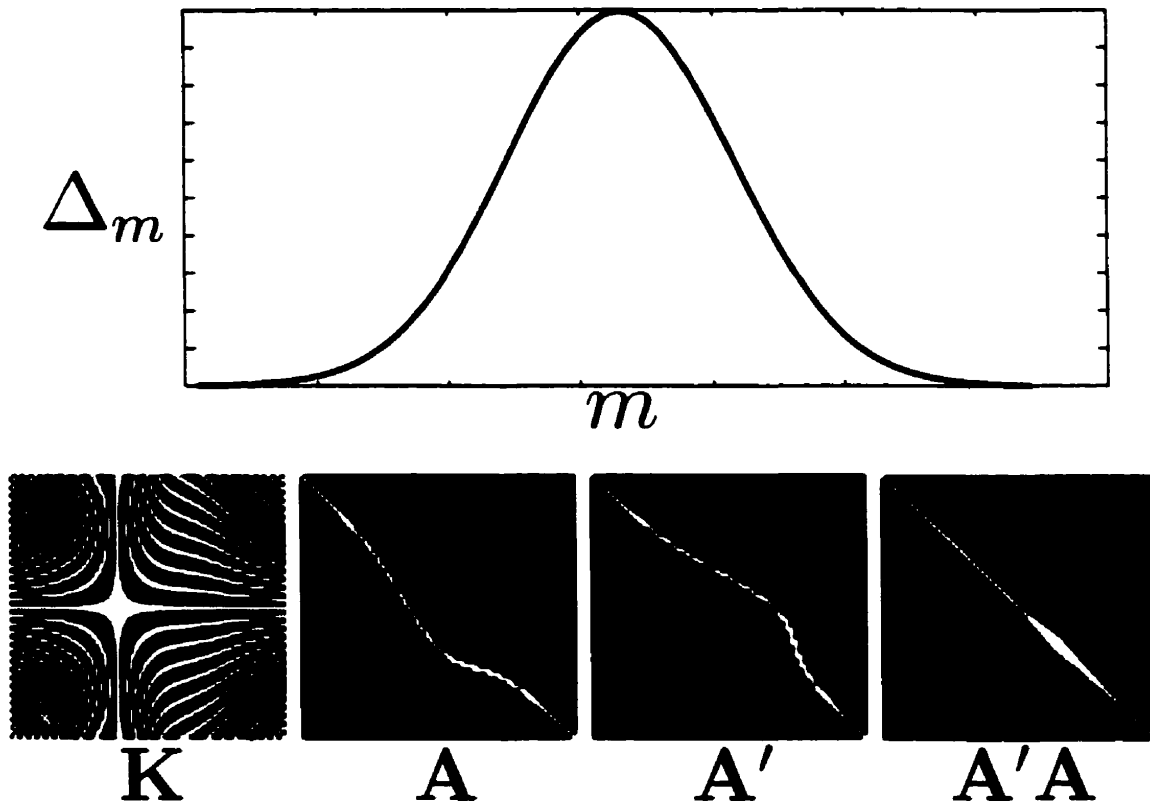


Figure 4.10: Various matrices involved in 1D correction.

*Illustration of the matrices  $\mathbf{K}$  from Eq. (4.31),  $\mathbf{A}$  from Eq. (4.34),  $\mathbf{A}'$  and  $\mathbf{A}'\mathbf{A} = \mathbf{P}$  from Eq. (4.36) computed from the 1D Gaussian field map shown on the top graph. Although it may be difficult to intuitively understand the meaning of  $\mathbf{K}$ , it is much clearer to look at its Fourier Transform  $\mathbf{A}$  which relates the distorted and ideal images. The curved diagonal of  $\mathbf{A}$  reflects the fact that the ideal becomes distorted when transformed by  $\mathbf{A}$ . One can also see how the conjugate phase methods, which attempt to correct by multiplying the distorted image by the complex conjugate of  $\mathbf{A}$ ,  $\mathbf{A}'$ , undoes the effect of the matrix  $\mathbf{A}$  regarding to pixel displacement. The matrix  $\mathbf{A}'\mathbf{A}$  represents the relationship between the conjugate phase reconstruction and the ideal image, and shows how the two images differ in amplitude.*

### 4.5.1 Solution of the 2D linear systems

In the case of 1D processing, the linear system

$$\mathbf{A}_n^\dagger \mathbf{I}_n = \mathbf{A}_n^\dagger \mathbf{A}_n \mathbf{I}_n \quad (4.37)$$

is solved for every column of the EPI image. The matrices  $\mathbf{A}_n$  are computed using equation [4.34]. The fact that  $\mathbf{A}$  has a closed form expression allows the computing requirement to be relaxed by considering only a certain number of the matrix elements on each side of the main diagonal.

It was found in practice, that in both 2D and 1D cases, a small number of iterations (2-3) was sufficient to yield a good solution. Not only did a larger number of iterations not help to significantly reduce the error, it may actually increase it and produce artifacts in the reconstructed image. The next chapter considers this point further.

## 4.6 Summary

This chapter has exposed the mathematical foundations underlying the core of the thesis. First, the EPI imaging equation problem was stated in terms of a 4D tensor equation. The EPI imaging process was also studied, and its point-spread function was shown to exhibit ghosting artifacts, in addition to the expected geometrical shift in the phase encoding direction.

The solutions of system of equation representing the EPI imaging process was shown to be practically achievable by transforming it in such a way as to get a sparse linear system. A full 2D correction method, based on the solution of the sparse linear system by the Conjugate Gradient algorithm, was developed, along with a computational simplification based on the low-rank characteristics of the EPI k-space trajectory.

Finally, it was demonstrated that the 4D tensor equation decouples into a set of smaller 2D problems when the k-space trajectory is approximated as varying in one direction only. A special case of above full 2D algorithm was derived from this simplification, leading to a 1D algorithm.

# Chapter 5

## Computer simulations and techniques comparisons

### 5.1 Introduction

This chapter investigates various aspects of the application of the CG-based correction method presented in the previous chapter, by means of computer simulations and compares the performance of different correction methods under different imaging conditions in the context of EPI imaging. Although these simulations can not take all aspects of an actual situation into account, they have the advantage of allowing the specific effects of various parameters to be observed.

The first section, (Section 5.2), introduces various aspects of the simulations. The Results and Discussion sections (Sections 5.3 and 5.4) are separated in two parts. The first deals with simulations performed to evaluate the impact of certain parameters of the CG method on the quality of the reconstruction. The second section presents a comparison, again by computer simulations, of the different  $B_0$ -map based methods.

## 5.2 Methods

### 5.2.1 Analytic phantom

In real experiments, it is often difficult to evaluate the performance of correction techniques due to the absence of an absolute “gold standard” against which to compare the results. In simulations, this gold standard is given *a-priori* and simulated experimental data are derived from it.

In this whole chapter, the reference image (i.e. the “gold standard”) is an analytic phantom (Fig. 5.1). It comes from an idealized analytic object known at infinite resolution. In this case, the object is a circle, with smaller squares inside. Because the continuous Fourier Transform of those shapes is known analytically, one can calculate the exact k-space signal that such an object would generate. The analytical phantom image is then obtained by evaluating the analytic Fourier Transform of the object onto a rectangular discrete grid (which is equivalent to sampling the k-space signal of the object) and performing an inverse discrete Fourier transform (IDFT) on this discrete data set. The analytic phantom used in this chapter was sampled onto a  $64 \times 64$  grid.

The advantage of using an analytic phantom, instead of an *a-priori* sampled image, is that the truncation (ringing) artifacts in the analytic phantom reflect more closely what is observed on an actual MR image.

### 5.2.2 EPI k-space trajectory

All simulations in this chapter assume the following parameters for the EPI sequence: Echo time of  $TE = 35\text{ms}$ , total acquisition time  $T_{\text{acq}} = 61\text{ms}$ . The readout period for a single line of k-space is  $T = 960\mu\text{s}$ . So, the bandwidth per pixel in the readout direction is  $1/T \approx 1\text{kHz}$  and the effective bandwidth in the phase encoding direction

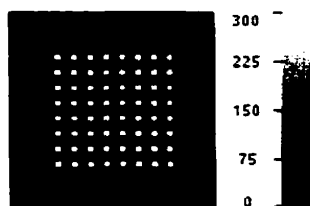


Figure 5.1: Analytic phantom used in the simulation

*The analytic phantom is computed by evaluating the analytic Fourier Transform of an object (in this case a circle with squares inside) onto a rectangular discrete grid of  $64 \times 64$  points, and performing an IFFT of this set of discrete data. This image is considered as the “gold standard” in the simulations of this chapter.*

is  $1/T_{\text{acq}} \approx 16\text{Hz}$ .

The readout gradient is constant, except for the ramp up and ramp down portions that are sinusoidal. In order to keep a constant sampling distance between k-space points, the ADC sampling timing must be non-uniform during the non-constant portions of the readout gradient (ramp-up and ramp-down portions). This is taken into account in the k-space trajectory matrix.

### 5.2.3 Simulation of EPI images

Given a  $B_0$ -map and a k-space trajectory, a simulated EPI image can be obtained by using the EPI imaging equation (4.1). Note that in distorted EPI image simulations, the kernel need not be explicitly stored in memory, so all the kernel values are used in the computation of the simulated EPI image. Fig. 5.2 shows three examples of simulated EPI images. The detailed algorithm for the computation of simulated EPI images is displayed in Fig. 5.3. The k-space trajectory is described in section 5.2.2.

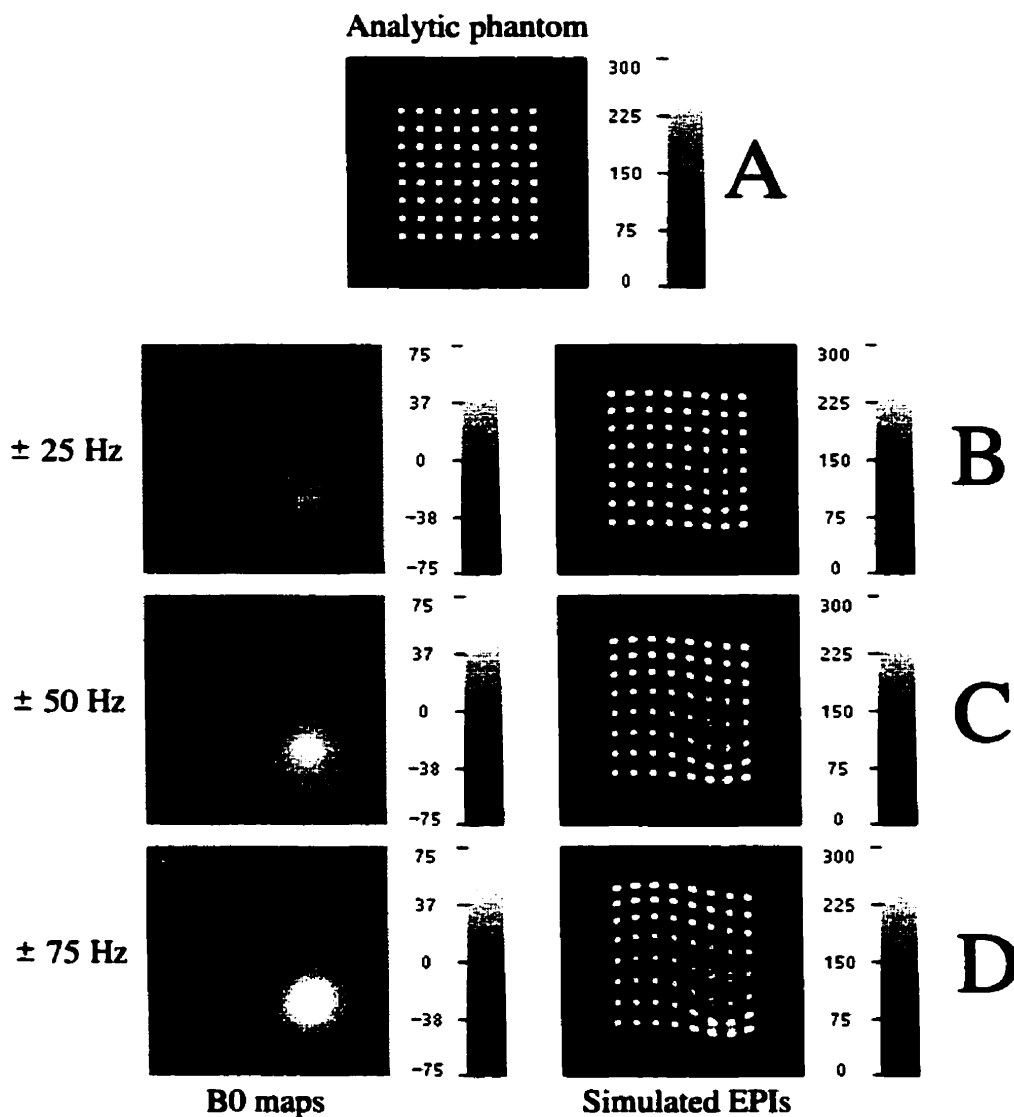


Figure 5.2: Simulated EPI images and  $B_0$  maps used in the simulations  
*Each of the simulations in this chapter uses one of the  $B_0$  field maps above (left, B, C and D). For each field map, a corresponding simulated EPI image (right, B, C and D) is computed from the analytic phantom (A) using the algorithm of Fig. 5.3. The  $k$ -space trajectory described in Section 5.2.2 is used for all simulations. The field map is composed of two Gaussian blobs with opposite amplitudes and different FWHM.*

---

input:    **I**    The  $M \times N$  undistorted image.  
           **B**    The  $M \times N$   $B_0$  map.  
           **t**    The  $M \times N$  k-space trajectory.

output:  **I'**    The  $M \times N$  simulated EPI image.

**for** ( $k = 0$  to  $M - 1$ )  
   **for** ( $l = 0$  to  $N - 1$ )  
       $S'(k, l) = 0$   
      **for** ( $m = 0$  to  $M - 1$ )  
          **for** ( $n = 0$  to  $N - 1$ )  
               $S'(k, l) = S'(k, l) +$   
                   $I(m, n) * \exp \{ -2\pi i * (km/M + ln/N + B(m, n) * t(k, l)) \}$   
              **end for**  $n$   
          **end for**  $m$   
      **end for**  $l$   
  **end for**  $k$   
**return**  $I' = 2D \text{ IFFT } (S')$

---

Figure 5.3: Algorithm for the calculation of the simulated EPI image.

### 5.2.4 Validation methodology

The experiments described in this chapter consist of correcting simulated distorted EPI images. Once the correction is done, one is interested in quantitatively comparing the corrected image and the original gold-standard (i.e. the analytic phantom). Since the presence of field inhomogeneity manifests itself as two distinct effects on an image, namely geometrical distortion and intensity distortion (section 2.2.3), it would be instructive to decouple the two effects on the distorted image and measure the amount of correction of the two effects separately. However, such a procedure is not easy to design and may introduce some artificial bias in the measurement of the amount of correction. Because of this, we use a much simpler metric, the root mean square (RMS) difference between the simulated image and the corrected image. Note however that this has the disadvantage of giving only a global measure of correction, regardless of the relative importance of geometrical versus intensity effects. We nevertheless believe that such a measure is meaningful as the ultimate goal of distortion correction is to produce a corrected image that is as close as possible to the image that would have been obtained had the field been perfectly homogeneous. Moreover, this measure can be made more robust and significant by computing the RMS difference only over pixels that have significant intensity, and in the present case, we fixed the threshold at 10% of the maximum pixel value, eliminating the contribution of background pixels in the measure. A negative aspect of this measure is that it is sensitive to any bias that may be introduced by a correction method. However, the reader will be able to check in the Results section (5.3) that the RMS differences give a good indication of how different two images are from each other and generally agrees with the visual perception of “closeness”.

More precisely, the measure of correction error is given by:

$$\text{RMS Difference} = \sqrt{\frac{1}{N^2} \sum_i \sum_j (|I_{\text{ph}}(i, j)| - |I_{\text{corr}}(i, j)|)^2} \quad (5.1)$$

where  $I_{\text{ph}}(i, j)$  and  $I_{\text{corr}}(i, j)$  are the complex values of the analytic phantom and the corrected image at pixel  $(i, j)$  respectively, and where  $i, j$  run over the pixel positions that have a significant signal intensity (larger than 10% of the maximum intensity of the analytic phantom).

### 5.2.5 Implementation of the CG algorithm for EPI correction

#### 2D

The 2D Conjugate Gradient method is implemented in two steps: The first is the computation of the sparse matrix representing the 4D kernel  $\tilde{\mathbf{A}}$  from the field map and the k-space trajectory, using algorithm shown in Fig. 4.9. One free parameter of the kernel computation is the threshold at which values are considered sufficiently small to be ignored. The number of elements in the sparse kernel increases as this threshold is reduced. This parameter has direct effects on the computational cost of the CG iterations because the sparse matrix-vector multiplication cost is directly proportional to the number of non-zero elements in the sparse matrix. In addition, it clearly has direct implications on the memory storage required for the kernel. One of the simulations presented in this chapter investigates the effect of this parameter on the reconstruction.

The second step is to apply the modified CG algorithm (4.25) using as input the kernel  $\tilde{\mathbf{A}}$  computed as described above and the distorted image reshaped into a column vector  $\tilde{\mathbf{M}}'$ . Then the iterations in Eq. (4.25) are performed, leading to an estimate of the correct image.

In some implementations of the CG algorithm, the iterations are performed until a condition on the residual is met, e.g. until the residual is smaller than a predetermined tolerance. This approach may lead to unpredictable computation times since the convergence may differ depending on the condition number of the linear system. In the implementation used in this thesis, the number of iterations is fixed, which ensures a predictable computation time. Moreover, depending on the nature of the linear system, the desired tolerance may not be achievable. Note, that the number of iterations directly affects the computational cost of the CG solution.

The total computational cost of the whole correction process, i.e. kernel computation and CG iterations, is therefore determined both by the sparsity of the kernel and the number of iterations. For the correction of one EPI image only, the kernel computation time is much larger than the time required for the CG iterations. Since the kernel computation time is independent of either of the two parameters, the total computation time is only weakly affected by them. On the other hand, when correction is applied to a large set of images all sharing the same k-space trajectory and  $B_0$  map, for instance in a fMRI study, then the number of iterations may be the most important factor determining the total correction time.

## 1D

The 1D version of the CG algorithm, like the 2D version, is performed in two steps. The main difference is that the 1D version is applied to every column of the distorted image to yield the corrected image.

For every column (or row, depending on the phase encoding direction) of the image, the matrix  $A_{m'm}$  is computed according to Eq. (4.34), and the system of equations (4.30) is solved with the modified Conjugate Gradient algorithm (4.25). Because the matrix  $A_{m'm}$  is close to diagonal, some computing time may be saved by

only computing the elements in a diagonal band. One of the simulations presented later will give an idea of the influence of the width of the diagonal band.

### 5.2.6 Noise and EPI images

In the simulations that compare the different correction methods, the effect of noise in the distorted input image is evaluated. Following the discussion in Chapter 2 on noise in MRI, complex Gaussian noise is added to the distorted simulated EPI image. The level of noise is adjusted in the simulations by changing the standard deviation of the noise added. The standard deviation  $\sigma$  of the noise to be added to an image for a given target SNR is:

$$\sigma = \frac{\langle m \rangle}{\text{SNR}}, \quad (5.2)$$

where  $\langle m \rangle$  is the mean image magnitude over the non-background regions. The SNR definition is given by Eq. (2.36). This relationship is valid when the image intensity is large because in this case, the noise obeys the Rician distribution which tends to the normal distribution with standard deviation  $\sigma$  with the signal amplitude goes to infinity. We note that violations of the Gaussian assumption of the signal noise distribution may cause an error in the estimation of the complex noise variance required for a given magnitude SNR, but does not imply that the noise distribution in the magnitude image is wrong.

### 5.2.7 Noise and $B_0$ map

In one of the simulations to be described later in this chapter, noise is added to the  $B_0$  field map. Because in a real situation the  $B_0$  map is derived from the phase difference between two images acquired with different echo times (see Section 2.4), the  $B_0$  map noise is stated in terms of the SNR of one or another of the two images.

The  $B_0$  map noise is computed as follows: First the phase noise is computed from Eq. (2.67), with the value of  $\sigma$  determined by Eq. (5.2). Note that this phase noise does not have the same probability distribution depending on the position. The phase noise in background regions is uniformly distributed between  $-\pi$  and  $\pi$ , and normally distributed in regions where there is signal. Second, the phase noise is converted into frequency by multiplying with the factor  $\sqrt{2}/(2\pi \Delta t)$  where  $\Delta t$  is the echo time difference of the field mapping sequence. We assume the value  $\Delta t = 4.48\text{ms}$ . The  $\sqrt{2}$  factor arises because the  $B_0$  map is obtained from a difference of two phase image and the standard deviation of the phase difference is  $\sqrt{2}$  times larger than the standard deviation of the individual phase images.

### 5.2.8 Computer hardware

All simulations in this chapter were performed on a PC equipped with an Intel Pentium 180 MHz processor and 128 MB of RAM, running the Linux Mandrake 7.0 operating system. The simulations were performed in the Matlab version 5.3 (The Mathworks, MA, USA) environment. Some algorithms, especially those involving intensive explicit looping, were coded in C (mex functions), but called from Matlab. The Matlab and C source code for all algorithms used in this chapter, together with the scripts running the simulations are included as an appendix.

## 5.3 Results

### 5.3.1 Effect of CG parameters

#### 2D

Simulations have been performed in order to investigate the effect of two important parameters of the CG method: the number of iterations, and the number of elements retained in the sparse kernel. In each case, the simulated EPI images and corresponding  $B_0$  maps shown in Fig. 5.2C were used.

In the first simulation, 5 reconstructions were performed using a unique kernel matrix, but with different numbers of iterations (0, 1, 2, 3 and 4). Results are shown in Fig. 5.4.

In a second simulation, 5 reconstructions were performed with a fixed number of iterations (3), but different numbers of non-zero elements in the kernel matrix. Results are shown in Fig. 5.5. The kernel density factor is defined as the percentage of non-zero elements in the kernel with respect to the kernel maximum size, i.e., if  $n$  is the number of non-zero elements, the sparsity factor is  $(100n/N^4) \%$ . For instance, a sparsity factor of 1% for a matrix size of  $64 \times 64$  means that the number of non-zero elements in the sparse kernel is  $1/100 * 64^4 = 167772$ .

#### 1D

Simulations were also run in a similar fashion to that described above, but with the 1D version of the algorithm. In the first (Fig. 5.6), the distorted EPI image was reconstructed with different numbers of iterations (0, 1, 2, 3 and 4). In the second (Fig. 5.7), the number of iterations was kept fixed, but the width of the diagonal band of  $A_{m'm}$  was set to 2, 4, 8, 16 and 32.

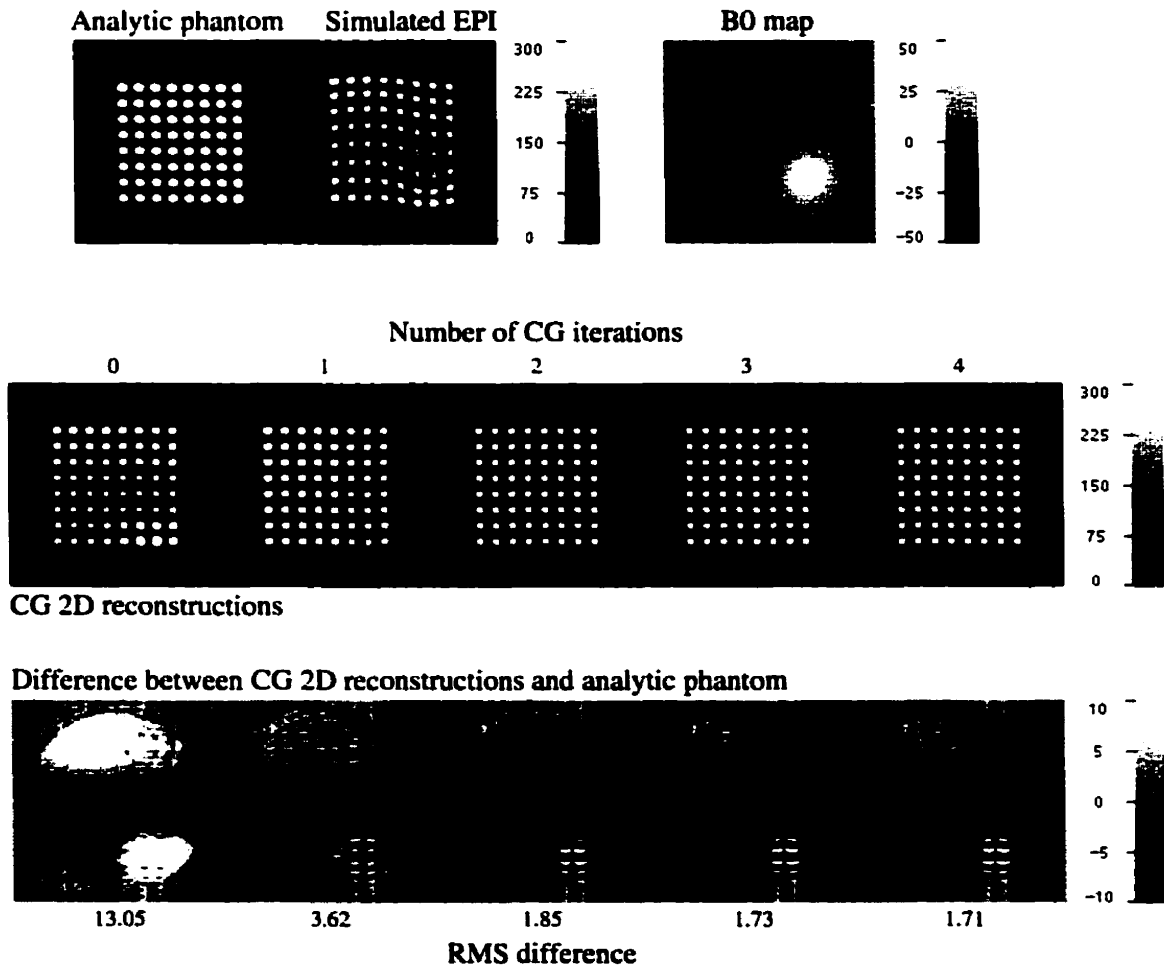


Figure 5.4: Effect of the number of iterations in the 2D CG algorithm. *Five reconstructions were performed with the same kernel, but with different numbers of CG iterations (center row). The difference images between the reconstructed images and the analytic phantom together with the RMS differences is shown on the bottom row.*

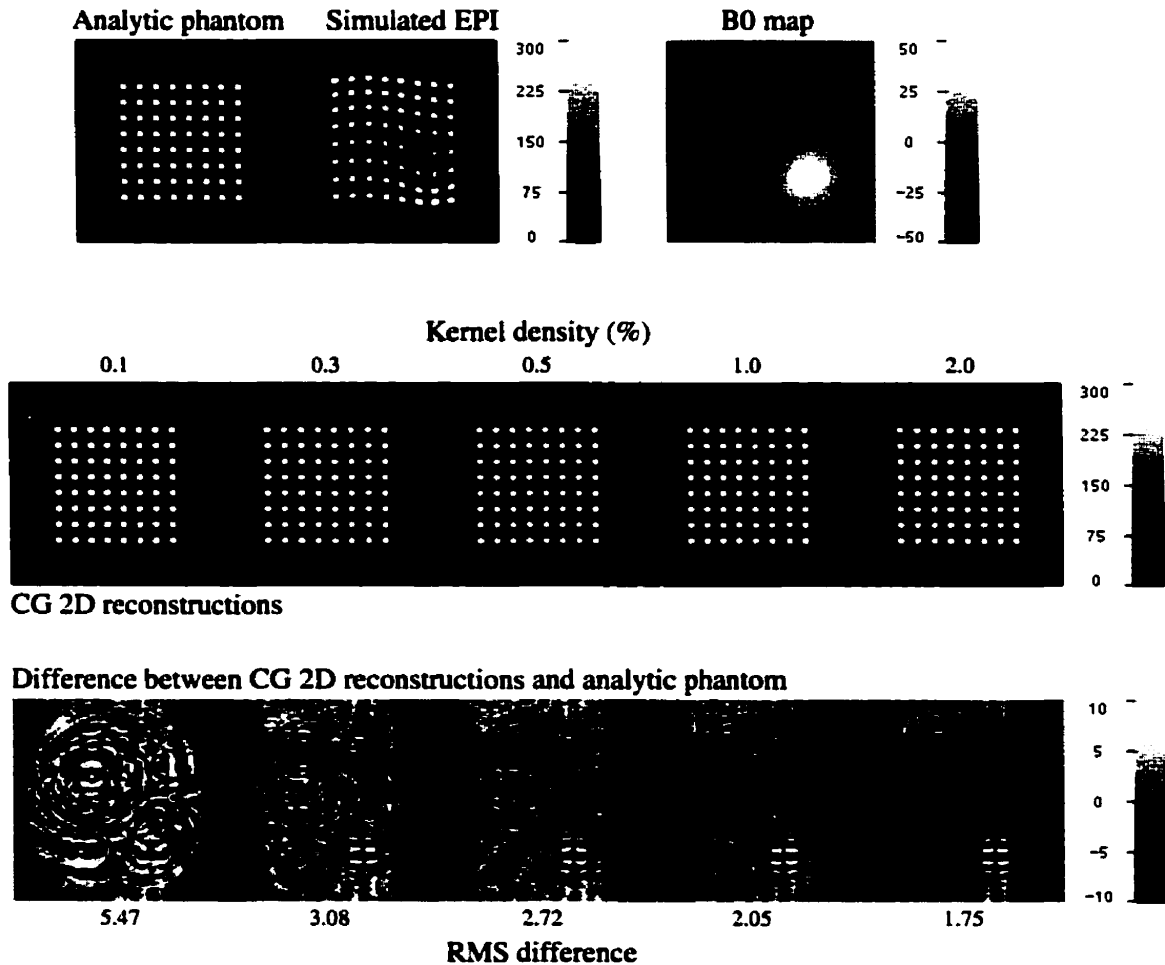


Figure 5.5: Effect of the sparsity level of the kernel in the 2D CG algorithm.

*Five reconstructions were performed with the same number of iterations, but with kernels having different numbers of non-zero elements. The difference images between the reconstructed images and the analytic phantom together with the RMS differences is shown on the bottom row. The sparsity factor is defined as the percentage of non-zero elements in the kernel with respect to the kernel size, i.e., if  $n$  is the number of non-zero elements, the sparsity factor is  $(100n/N^4)$  %.*

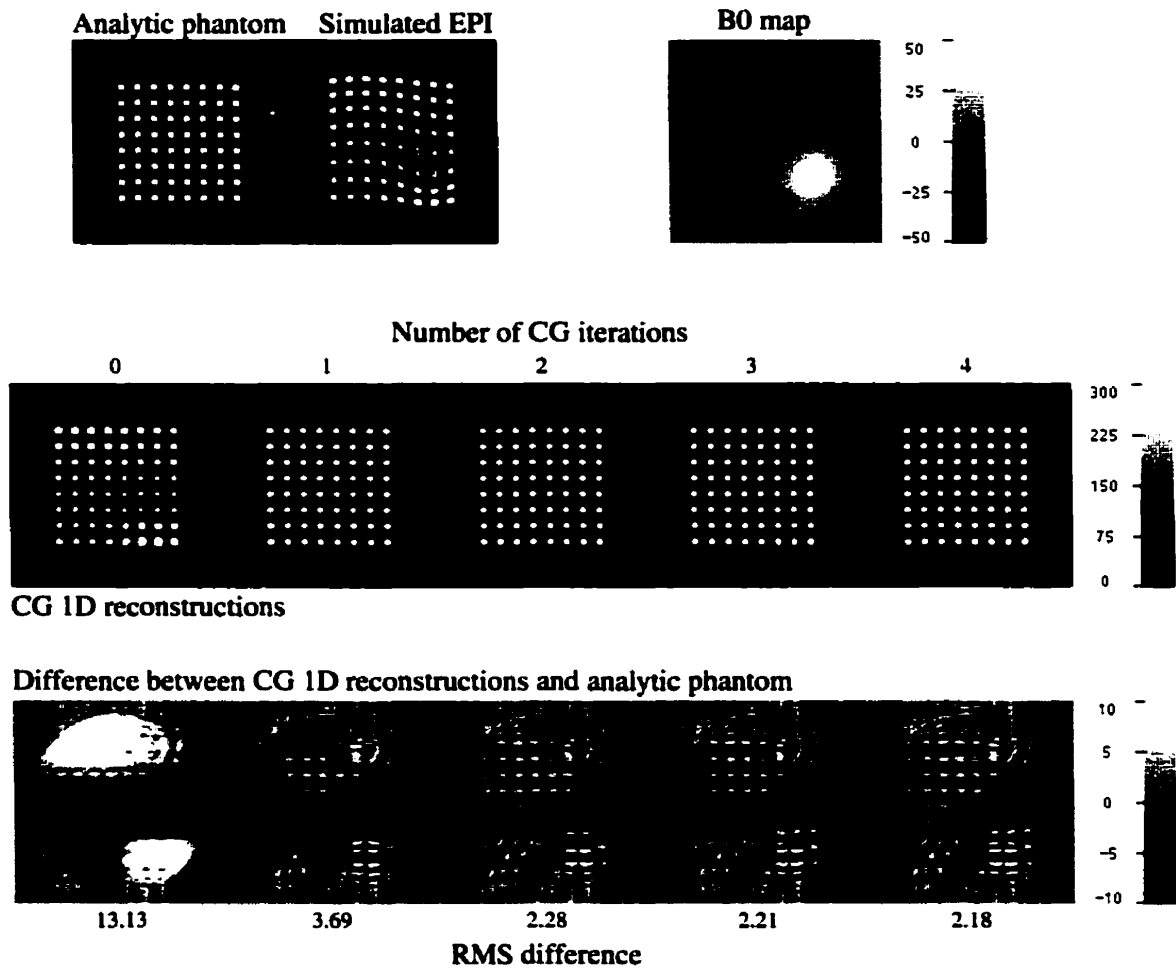


Figure 5.6: Effect of the number of iterations in the 1D CG algorithm  
*Five reconstructions were performed with the same kernel, but with different numbers of CG iterations (center row). The difference images between the reconstructed images and the analytic phantom together with the RMS differences is shown on the bottom row.*

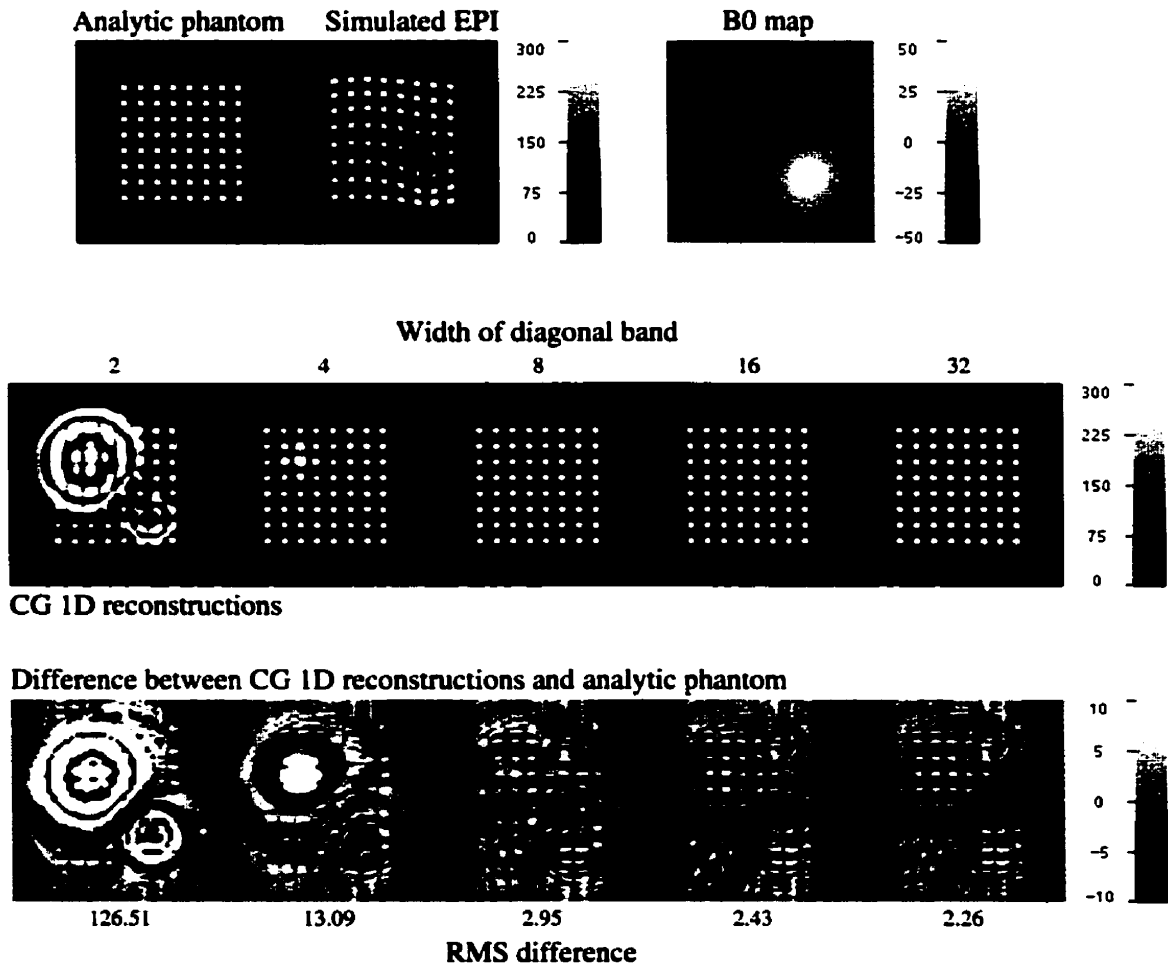


Figure 5.7: Effect of the sparsity of the kernel in the 1D CG algorithm.

*Five reconstructions were performed with the same number of iterations, but with kernels with a diagonal band having different widths. The difference images between the reconstructed images and the analytic phantom (bottom row) together with the RMS differences is shown on the bottom row. The sparsity factor is defined as the percentage of non-zero elements in the kernel with respect to the kernel size, i.e., if  $n$  is the number of non-zero elements, the sparsity factor is  $(100n/N^4) \%$*

### 5.3.2 Comparison between the different methods for EPI correction

In this section, we describe simulations whose goal was to evaluate the relative performance of the different correction methods in EPI. The aspects studied are the effect of noise on the input EPI images and the effect of noise in the  $B_0$  map.

#### On the distortion correction methods simulated

The methods compared are Conjugate Gradient (CG), Conjugate Phase (CP) Pure Geometric Interpolation (PGI), Intensity Corrected Geometrical Interpolation (ICGI) and K-Space Correction (KSC).

As discussed in the literature review chapter (section 3.1.1), the PGI and ICGI methods do not take the sinc-like aspect of the PSF into account. As a consequence, it was found that the performance of those methods can be significantly degraded for small matrix sizes due to partial volume effects. This can be improved however by interpolating the distorted profile over a smaller pixel size prior to the application of those correction methods [48]. For this reason, we implemented the two methods in two different manners: one where the correction was applied directly to the distorted image profile (labelled as PGI and ICGI), and the other where the correction was applied on a sinc-interpolated distorted profile (labelled as SI-PGI and SI-ICGI). The resulting corrected profiles were interpolated back to the original pixel size after correction.

To summarize, the different correction methods compared are:

- 2D Conjugate gradient (CG2D)
- 1D Conjugate gradient (CG1D)
- 2D Conjugate phase (CP2D)

- K-space correction (KSC)
- Pure Geometric Interpolation (PGI)
- Sinc Interpolated Pure Geometric Interpolation (SI-PGI)
- Intensity Corrected Geometrical Interpolation (ICGI)
- Sinc Interpolated Intensity Corrected Geometrical Interpolation (SI-ICGI)

### **Effect of image noise**

The purpose of these simulations is to evaluate the effect of noise in the EPI image upon the correction process. Each correction method is applied to a distorted EPI image to which noise was added. The EPI image SNR in the simulations are  $\infty$  (no noise), 70, 50, 30 and 10. Moreover, each simulation was performed with different levels of distortions (B, C and D on Fig. 5.2). In order to reduce and assess the effect of statistical fluctuations, the simulations were run 10 times for each level of image noise, and the RMS differences were averaged. The details of these simulations are shown in Fig. 5.8.

Figs. 5.9, 5.10 and 5.11 show the quantitative results of the simulations for each distortion levels. Figs. 5.12 to 5.20 show examples of corrections at image noise levels  $\infty$ , 70, and 50, and at different levels of distortion.

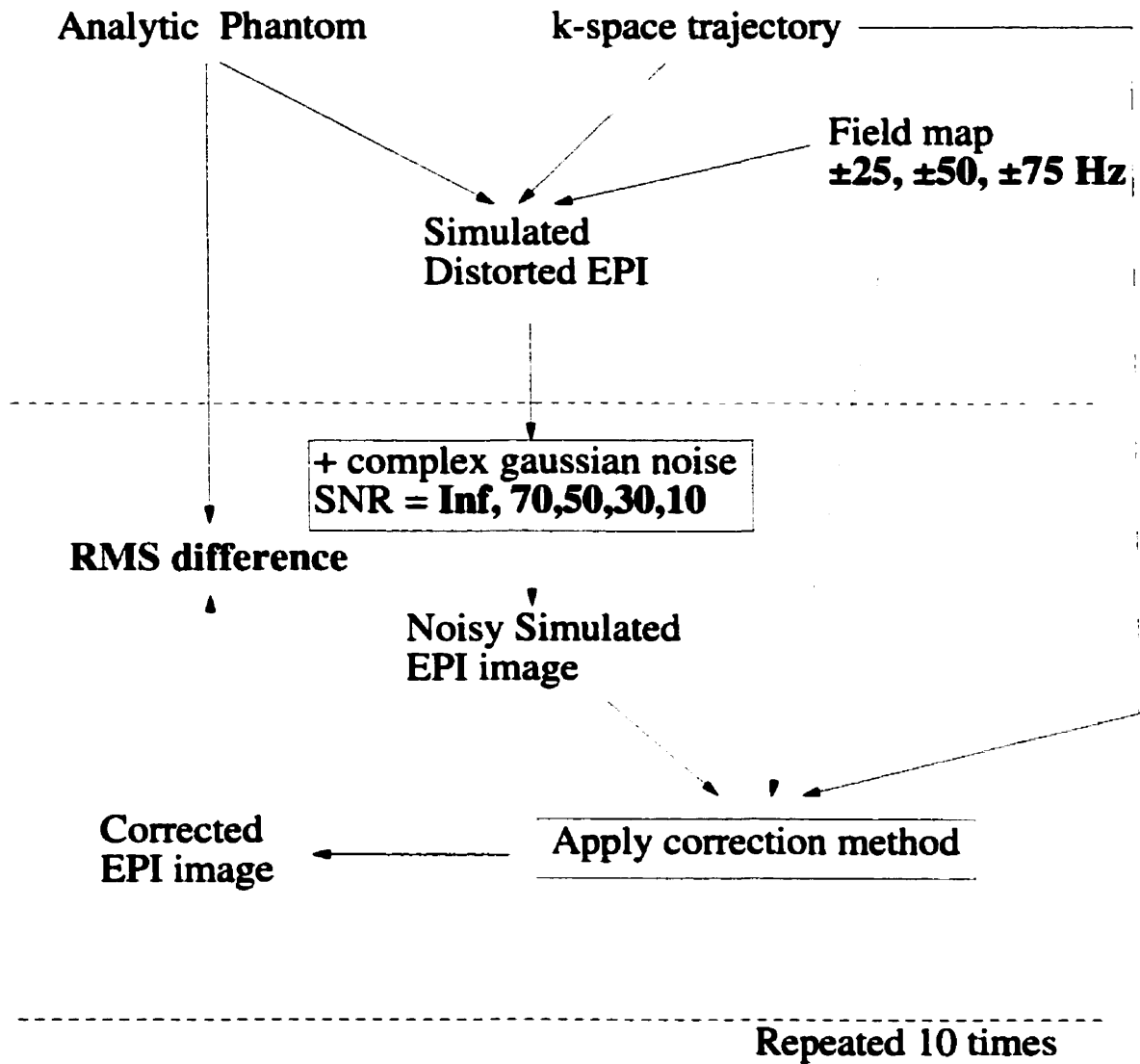


**Figure 5.8: Simulations of the effect of EPI image noise**

*A simulated distorted EPI was computed from an analytic phantom image, a k-space trajectory matrix and a field map. Then, the following was repeated 10 times: Noise was added to the simulated EPI image and formed a noisy EPI image. Then the various correction methods were applied to the noisy EPI image, using the k-space trajectory and the field map used previously for the creation of the simulated EPI image. Finally, the corrected image was compared with the original analytic phantom by computing the RMS difference between the two images.*

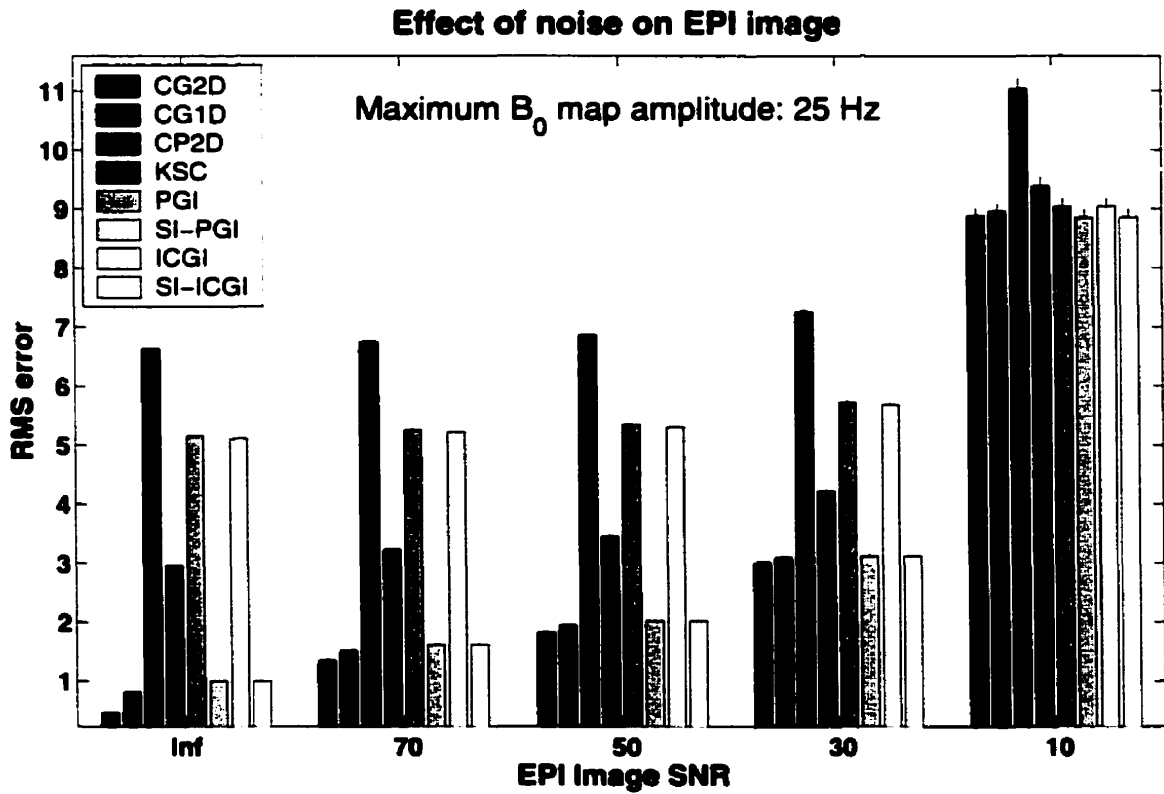


Figure 5.9: Effect of EPI image noise. Maximum  $B_0$  amplitude =  $\pm 25$  Hz. RMS difference between images corrected with the different methods and the analytic phantom. The small lines on top of the bars represent the standard deviation over 10 identical trials. Some of them are too small to be visible on the graph.

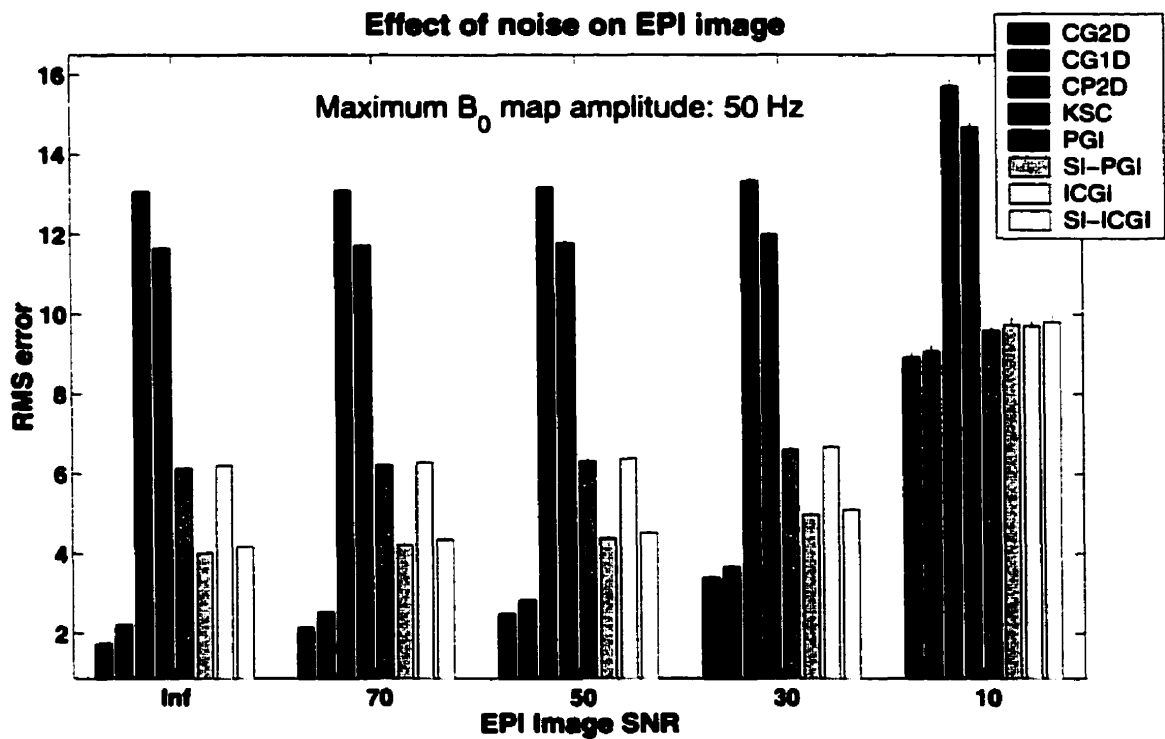


Figure 5.10: Effect of EPI image noise. Maximum  $B_0$  amplitude =  $\pm 50$  Hz. RMS difference between images corrected with the different methods and the analytic phantom. The small lines on top of the bars represent the standard deviation over 10 identical trials. Some of them are too small to be visible on the graph.

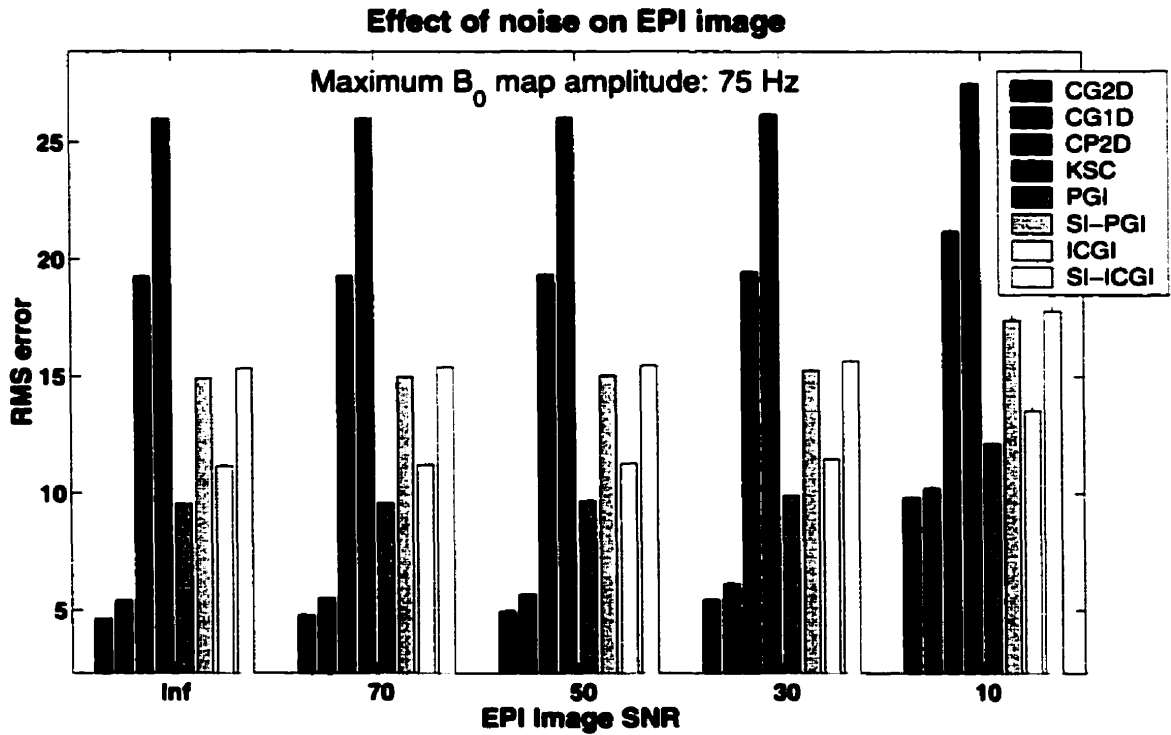


Figure 5.11: Effect of EPI image noise. Maximum  $B_0$  amplitude =  $\pm 75$  Hz. RMS difference between images corrected with the different methods and the analytic phantom. The small lines on top of the bars represent the standard deviation over 10 identical trials. Some of them are too small to be visible on the graph.

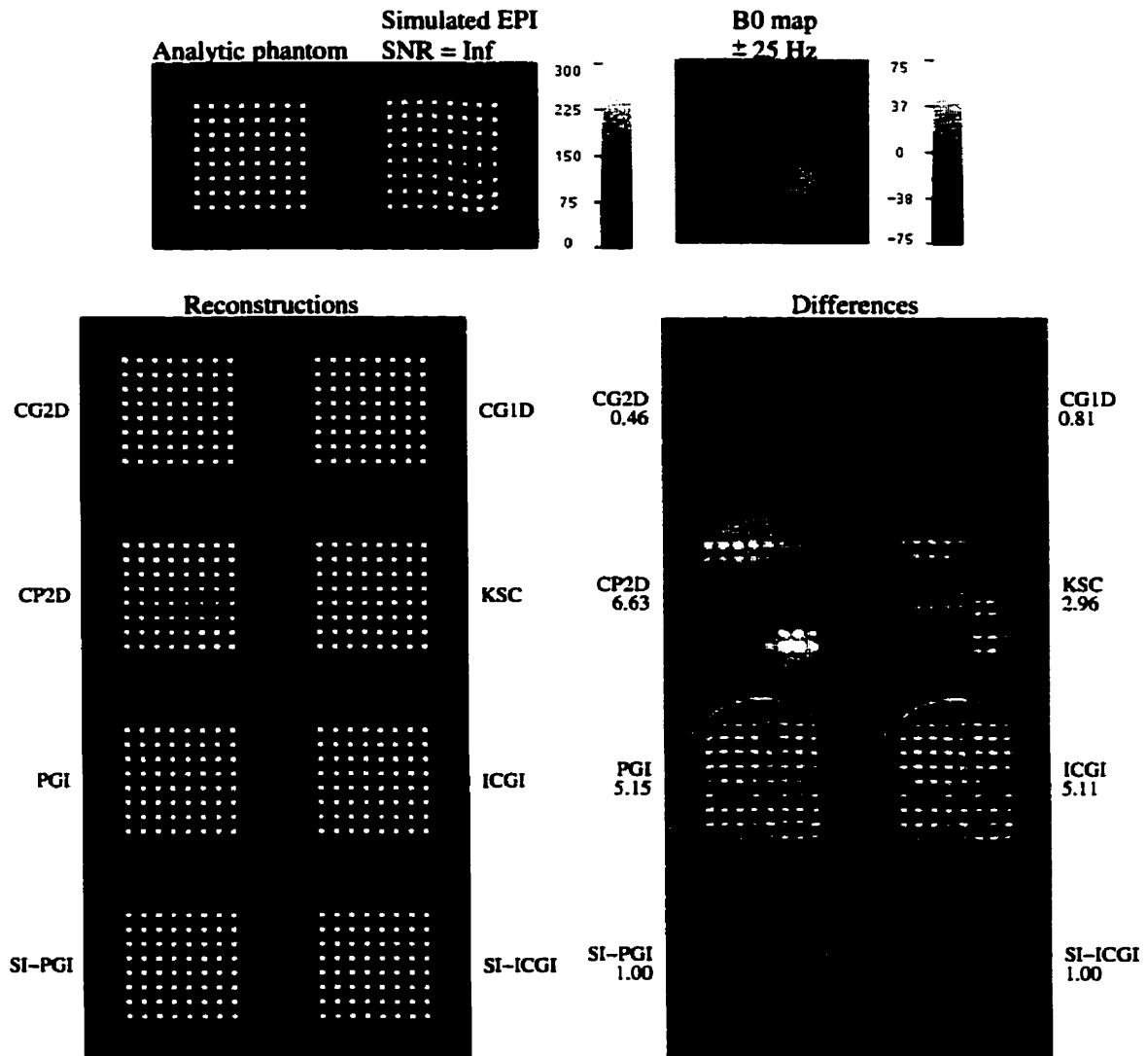


Figure 5.12: Correction with EPI  $\text{SNR}=\infty$ , and  $B_0$  max. amplitude =  $\pm 25$  Hz.

The images on top are the analytic phantom image (top left), the simulated EPI (top center) and the  $B_0$  field map (top right). The images in the left part of the figure are the images reconstructed with the various correction methods (see 5.3.2). The images in the right portion of the figure represent the difference between the reconstructed images and the analytic phantom. A perfect correction would yield a zero difference image. The numbers close the the difference images are the RMS errors for the respective methods. The grayscale map of the difference images runs from -25 to +25. The next figures are built on the same model.

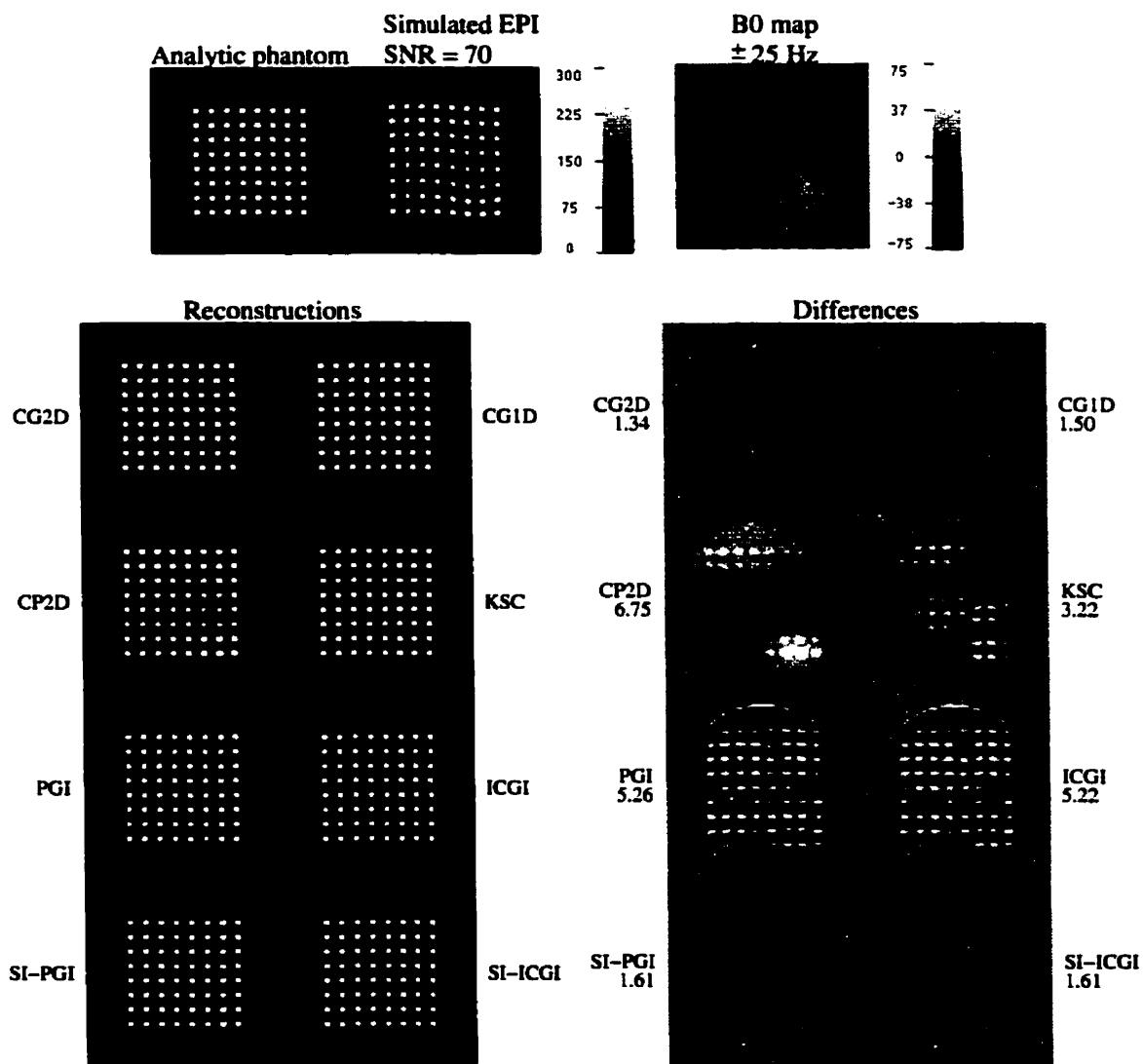


Figure 5.13: Correction with EPI SNR=70, maximum  $B_0$  amplitude =  $\pm 25$  Hz.

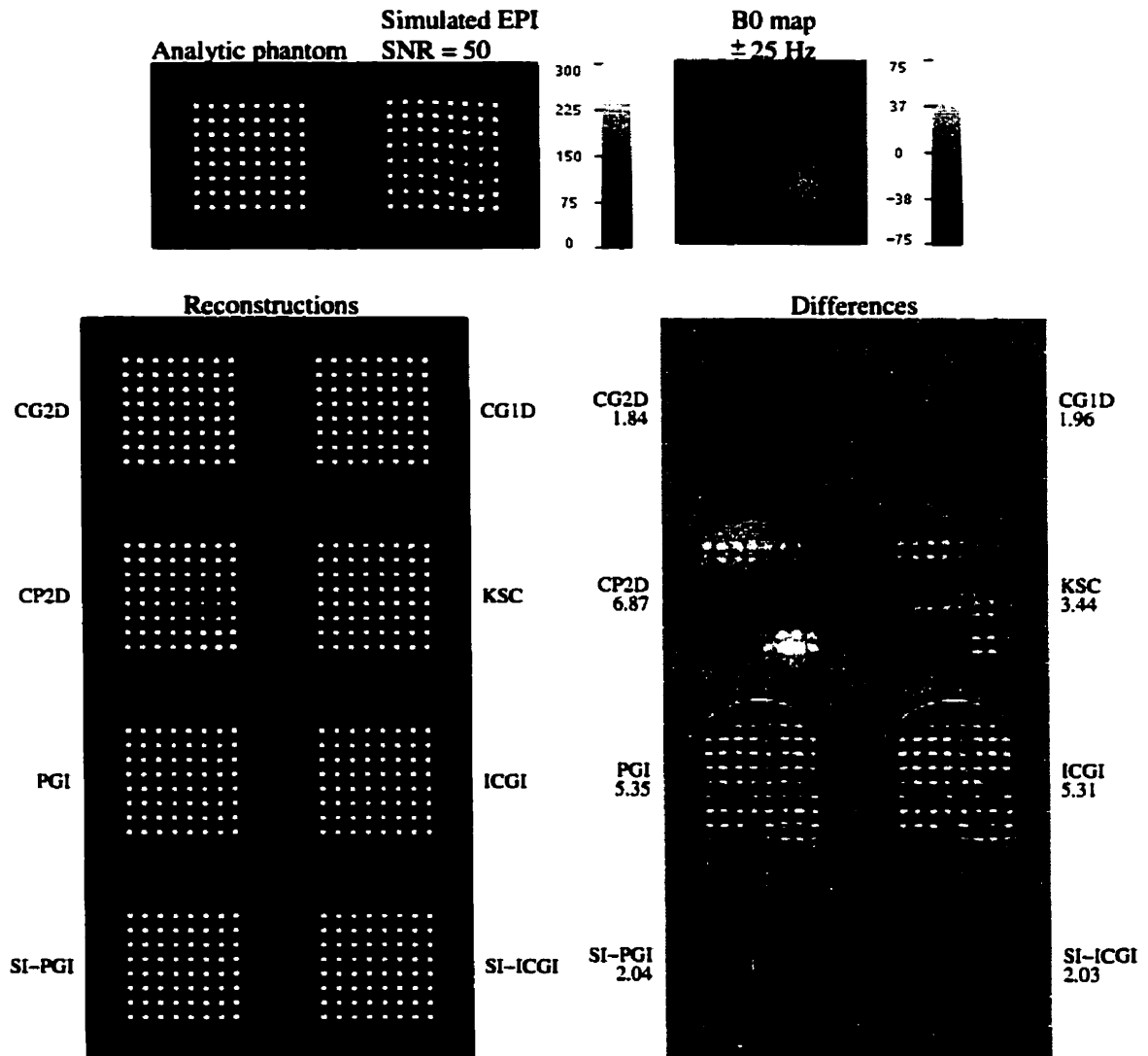


Figure 5.14: Correction with EPI SNR=50, maximum  $B_0$  amplitude =  $\pm 25$  Hz.

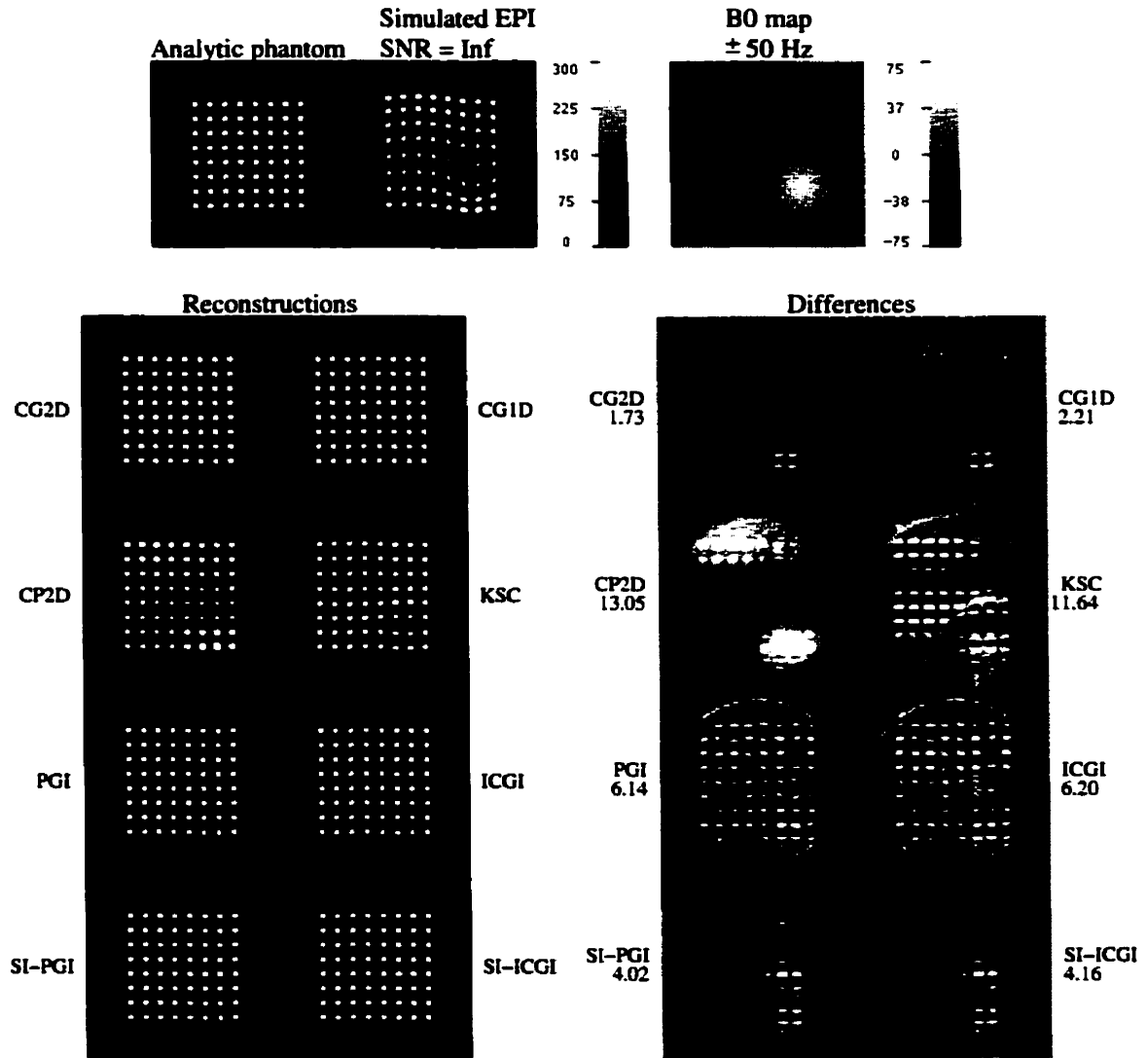


Figure 5.15: Correction with EPI  $\text{SNR}=\infty$ , maximum  $B_0$  amplitude =  $\pm 50$  Hz.

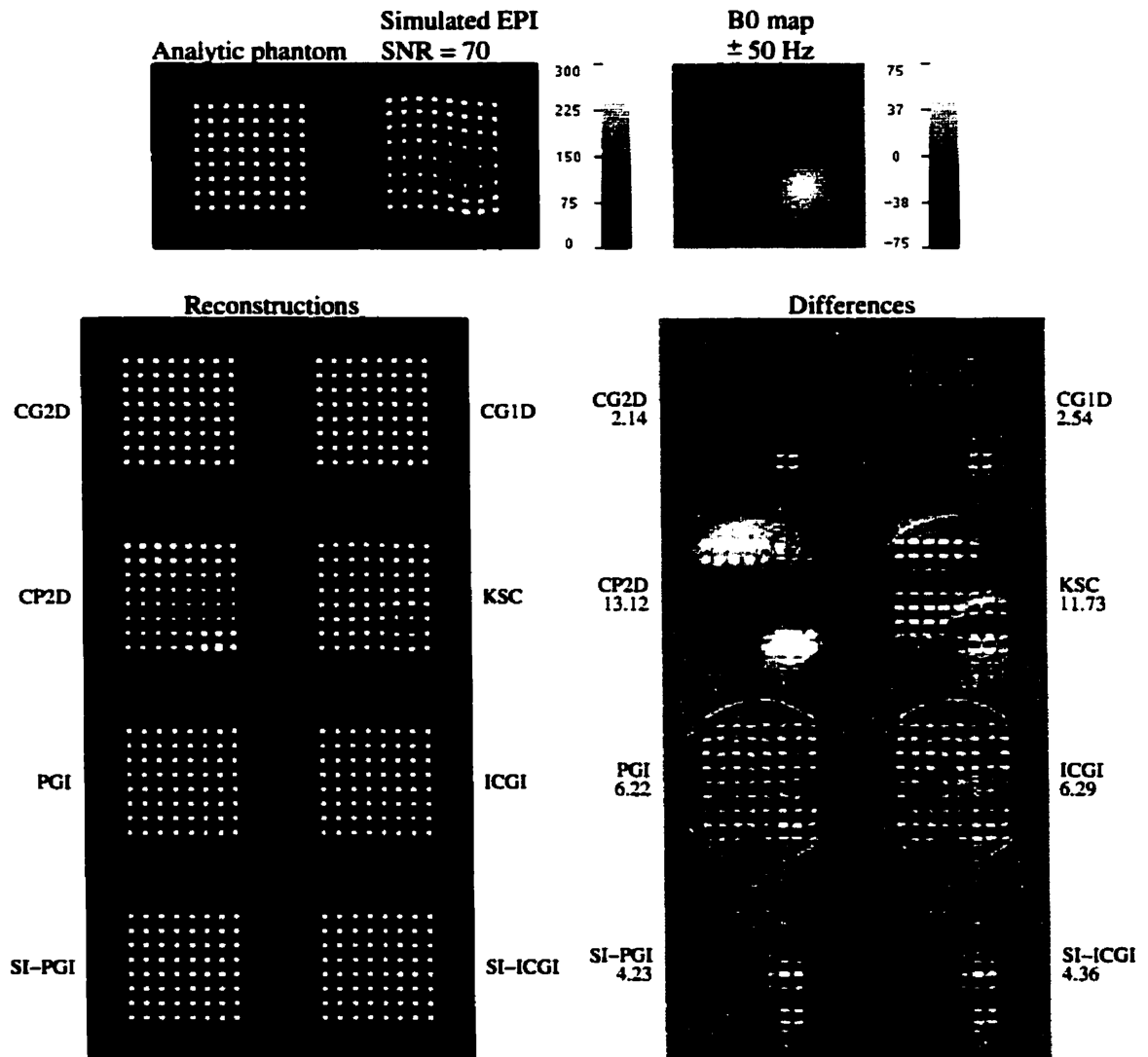


Figure 5.16: Correction with EPI SNR=70, maximum  $B_0$  amplitude =  $\pm 50$  Hz.

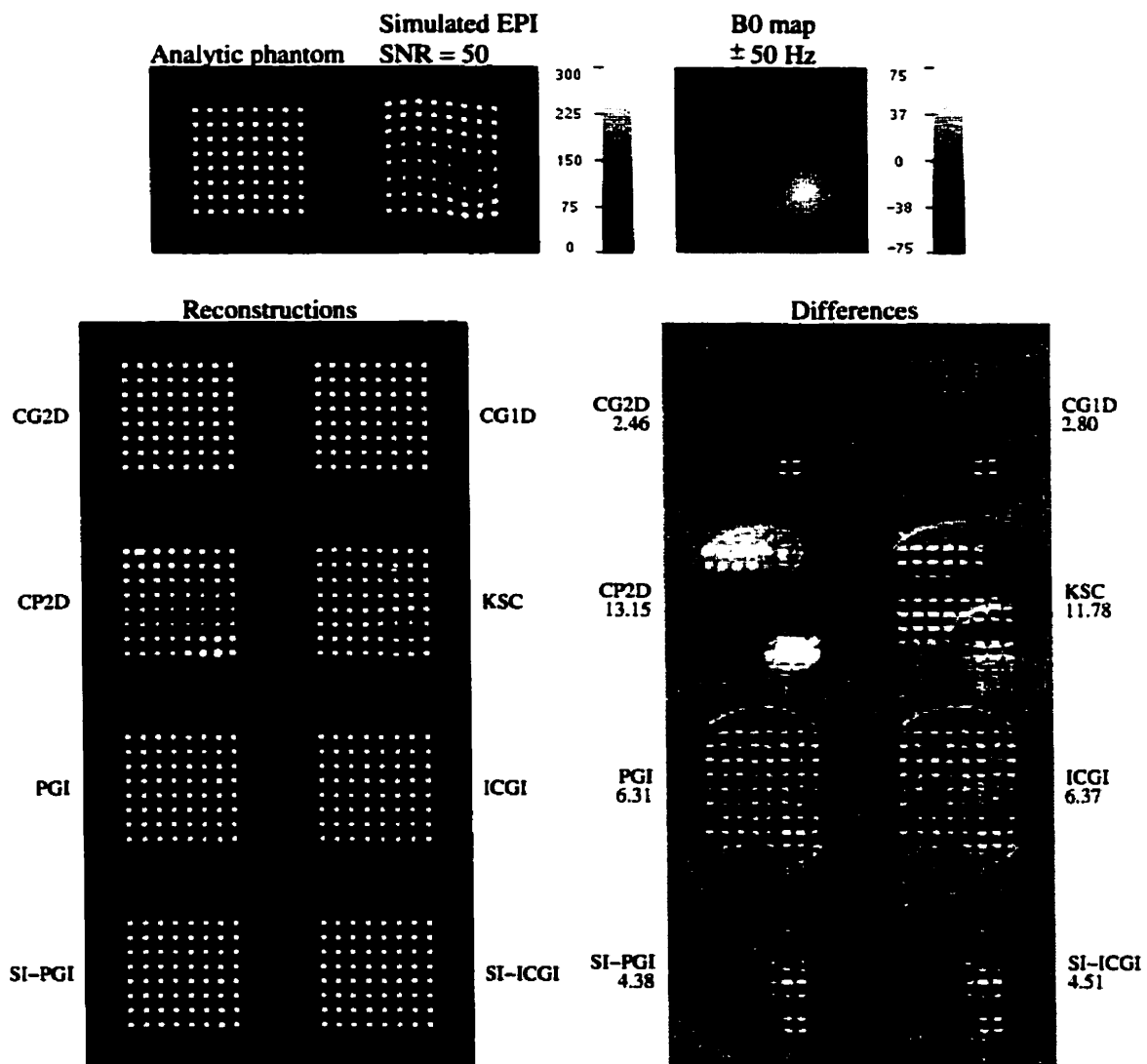


Figure 5.17: Correction with EPI SNR=50, maximum  $B_0$  amplitude =  $\pm 50$  Hz.

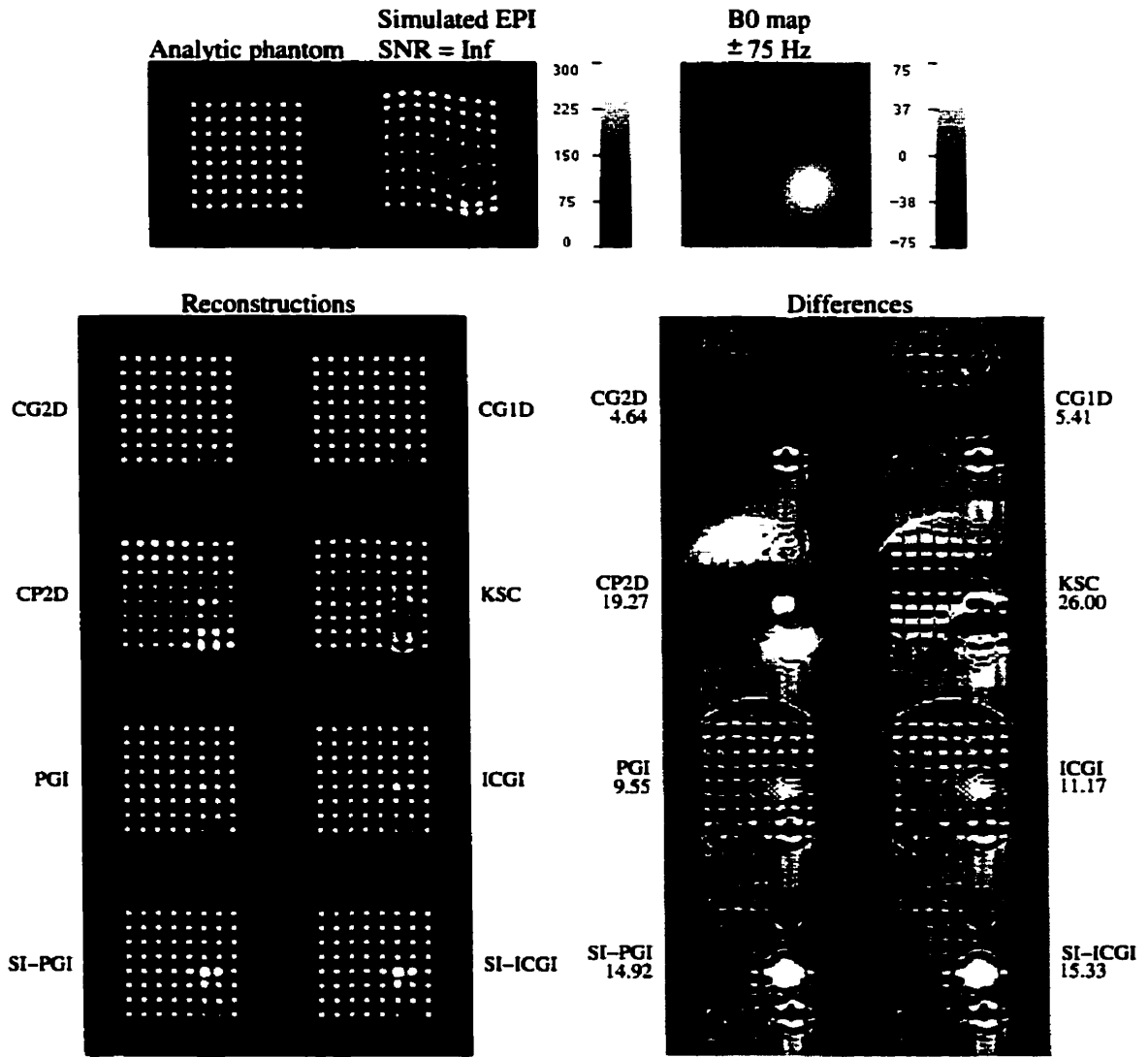


Figure 5.18: Correction with EPI SNR=∞, maximum B<sub>0</sub> amplitude = ± 75 Hz.

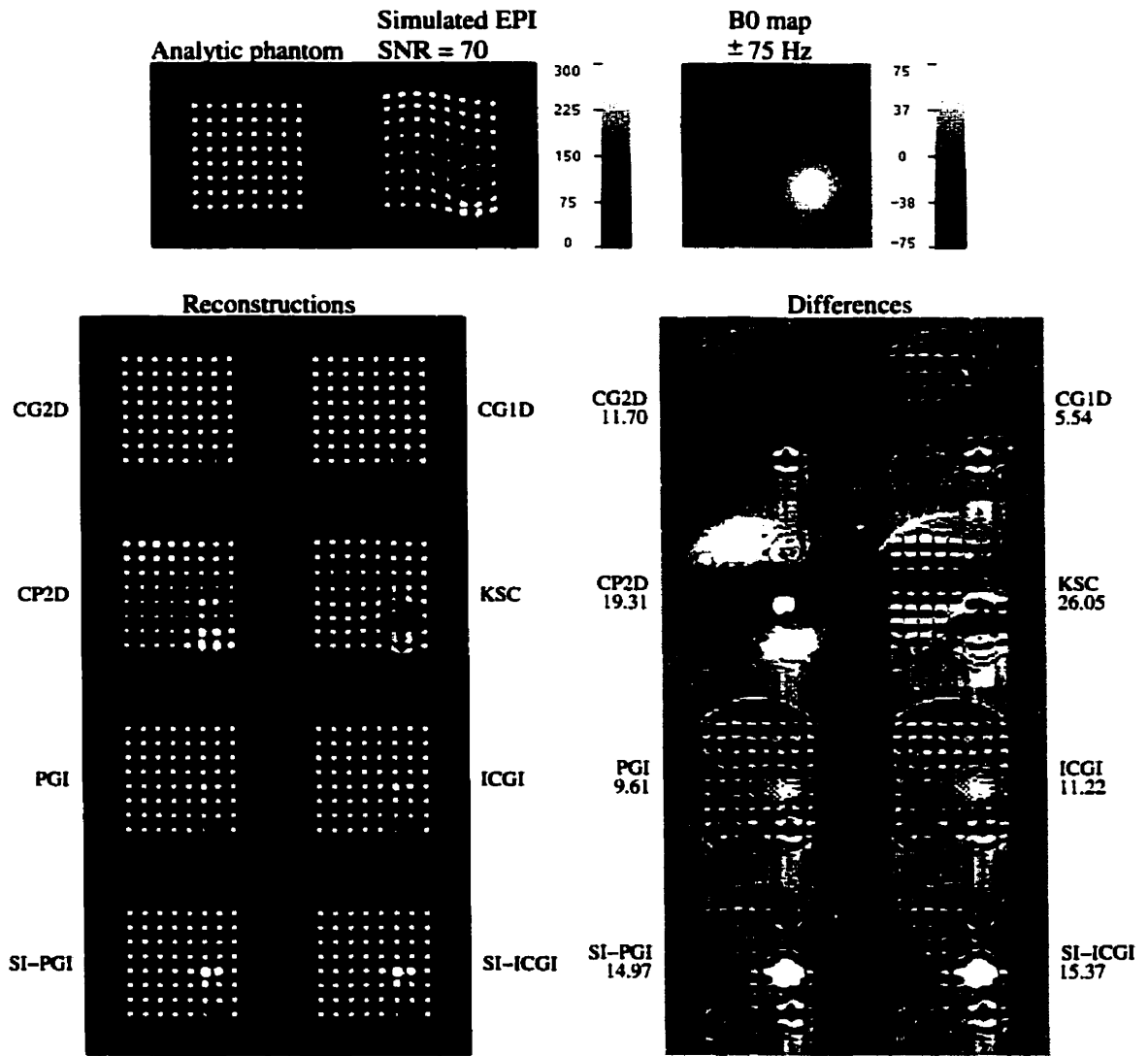


Figure 5.19: Correction with EPI SNR=70, maximum  $B_0$  amplitude =  $\pm 75$  Hz.

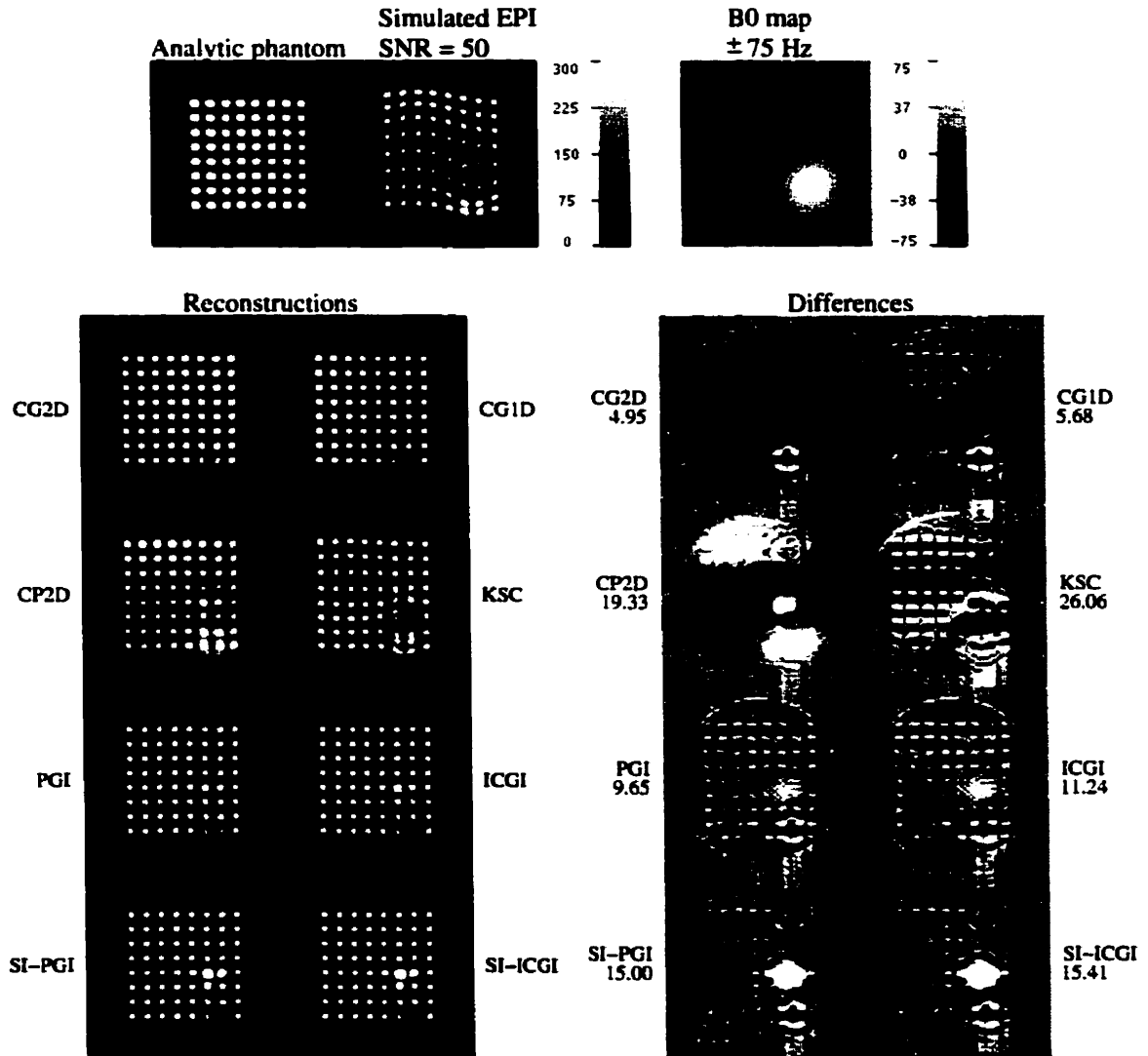


Figure 5.20: Correction with EPI SNR=50, maximum  $B_0$  amplitude =  $\pm 75$  Hz.

### Effect of $B_0$ map noise

The purpose of these simulations was to evaluate the effect of  $B_0$ -map noise on the correction process. Each correction method was applied to a distorted noiseless simulated EPI image, with noisy  $B_0$  maps. The  $B_0$  map SNR in the simulations were 70 and 50. In these simulations, the noise was added to the  $B_0$  map, according to the description in Section 5.2.7, and was then spline-smoothed. The simulations were run 10 times for each level of  $B_0$  map noise, and the RMS differences were averaged. The details of these simulations are shown in Fig. 5.21. The need for processing the  $B_0$  map may be better appreciated by looking at Fig. 5.25, where a reconstruction was performed with a  $B_0$  map that was not processed at all (only the background values were masked), or at Fig. 5.26, where the field map had the meaningless background pixels masked out.

Fig. 5.22 shows the quantitative results of the simulations for each method and each noise level. Figs. 5.23 and 5.24 show examples of corrections at  $B_0$  noise levels 50 and 10.

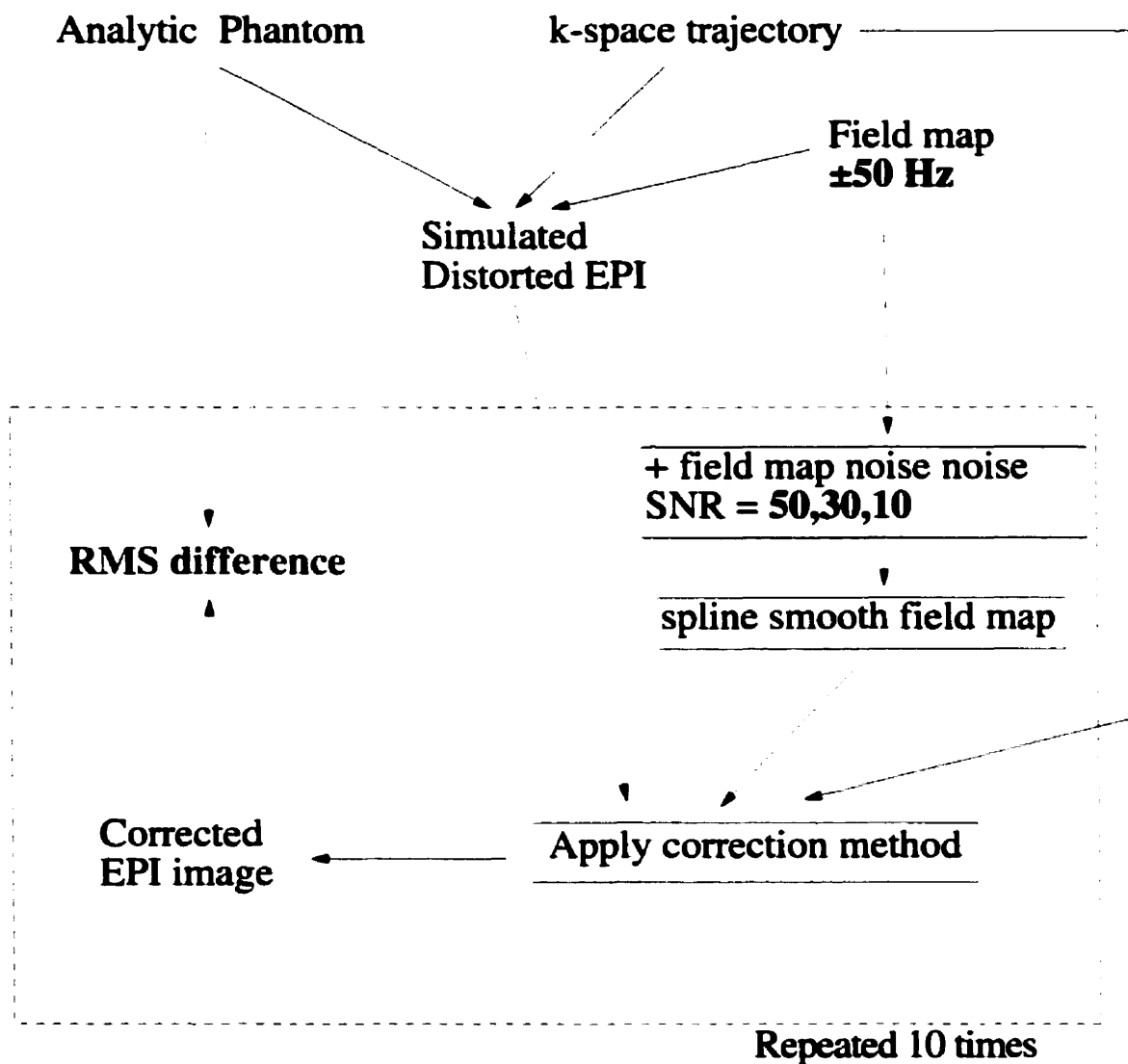


Figure 5.21: Simulations of the effect of  $B_0$  map noise

*A simulated distorted EPI was computed from an analytic phantom image, a k-space trajectory matrix and a field map. Then, the following was repeated 10 times: Noise was added to the  $B_0$  map according to the description of section 5.2.7. The resulting noisy  $B_0$  map was then spline-smoothed and the various correction methods were applied to the EPI image, using the k-space trajectory and the spline-smoothed field map. Finally, the corrected image was compared with the original analytic phantom by computing the RMS difference between the two images.*

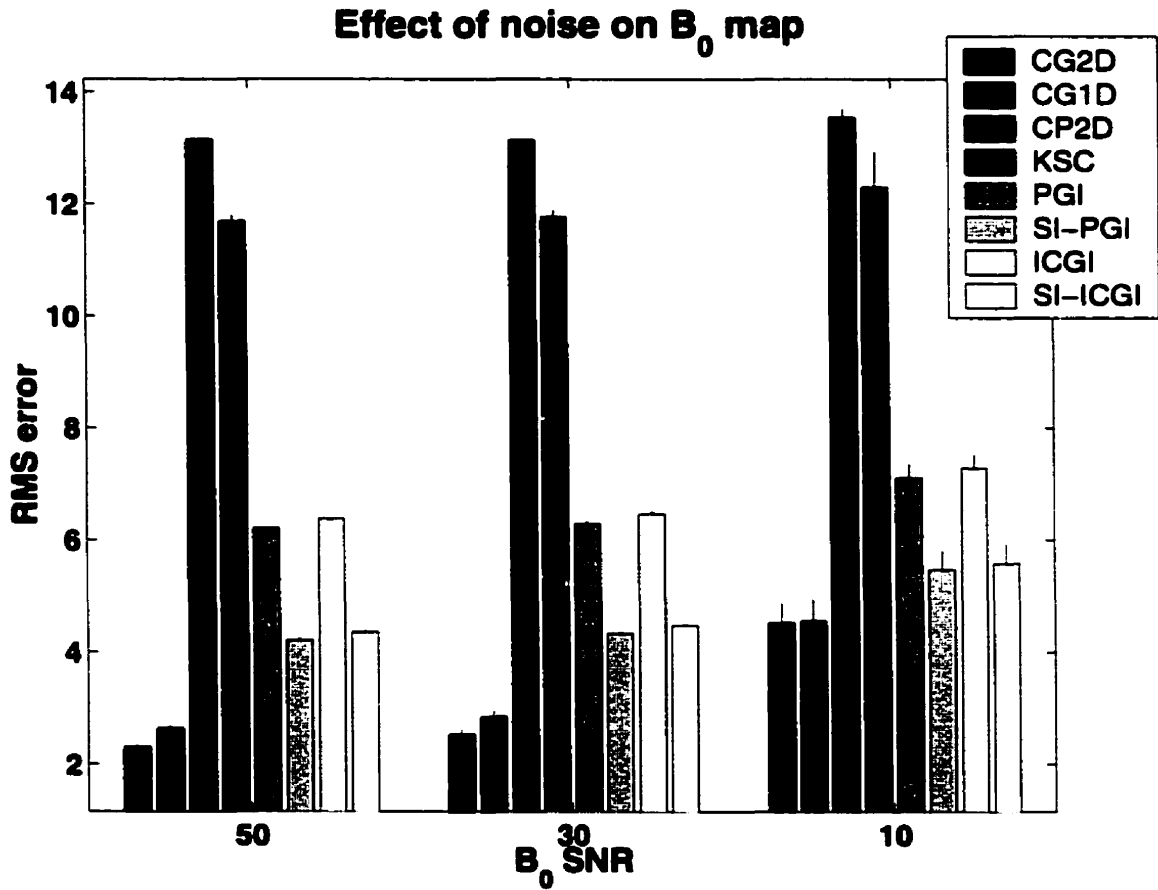


Figure 5.22: Effect of  $B_0$  map noise

*RMS difference between images corrected with the different methods and the analytic phantom. The small lines on top of the bars represent the standard deviation over 5 identical trials.*

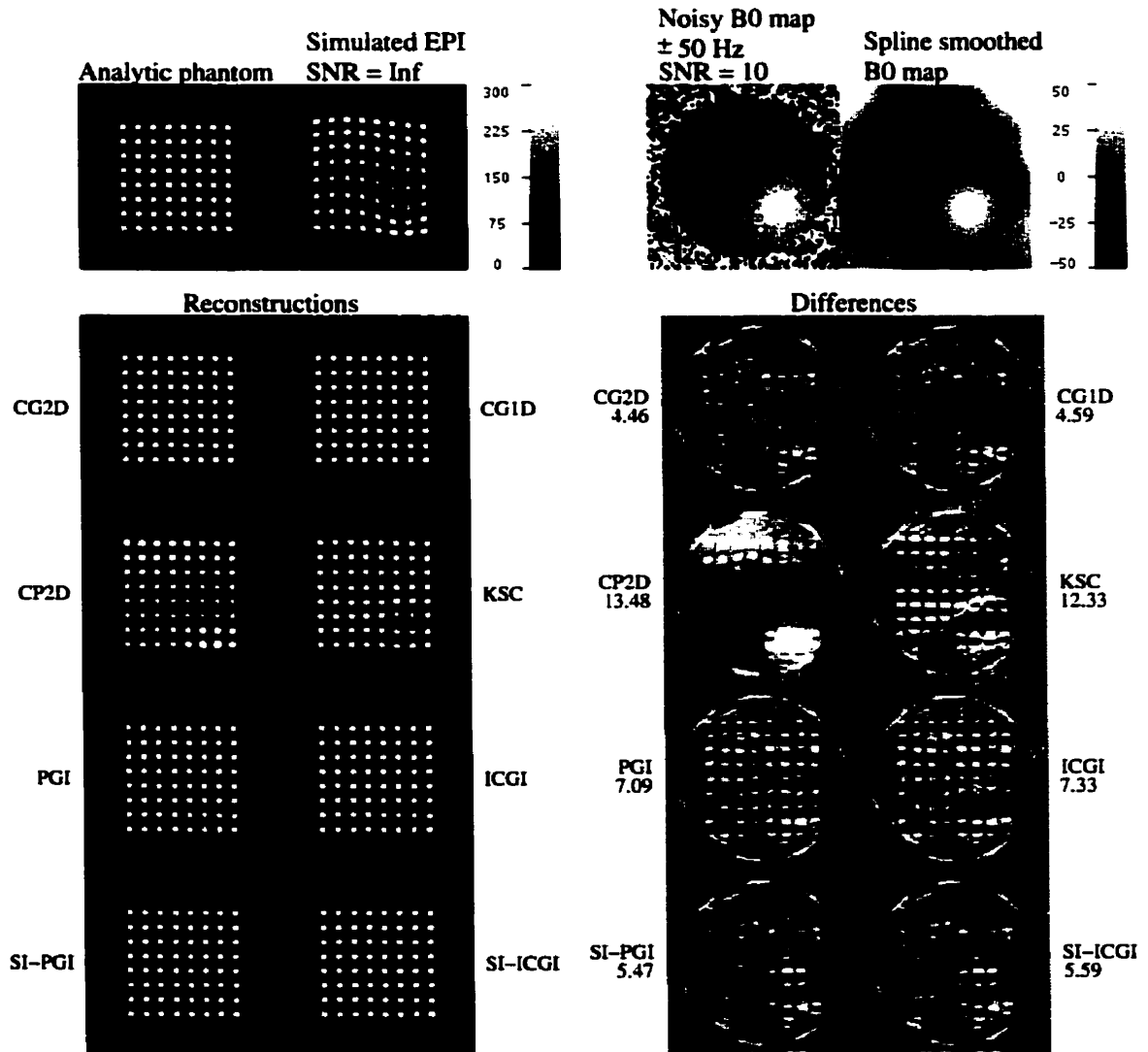


Figure 5.23: Correction with  $B_0$  SNR=10, maximum  $B_0$  amplitude =  $\pm 50$  Hz.

The images on top are the analytic phantom (top left) and the simulated EPI (top right). The images in the lower left part of the figure are reconstructed with the various correction methods (see 5.3.2). The images in the lower right portion of the figure represents the difference between the reconstructed images and the analytic phantom. A perfect correction would yield a zero difference image. The numbers close to the difference images are the RMS errors for the respective methods.

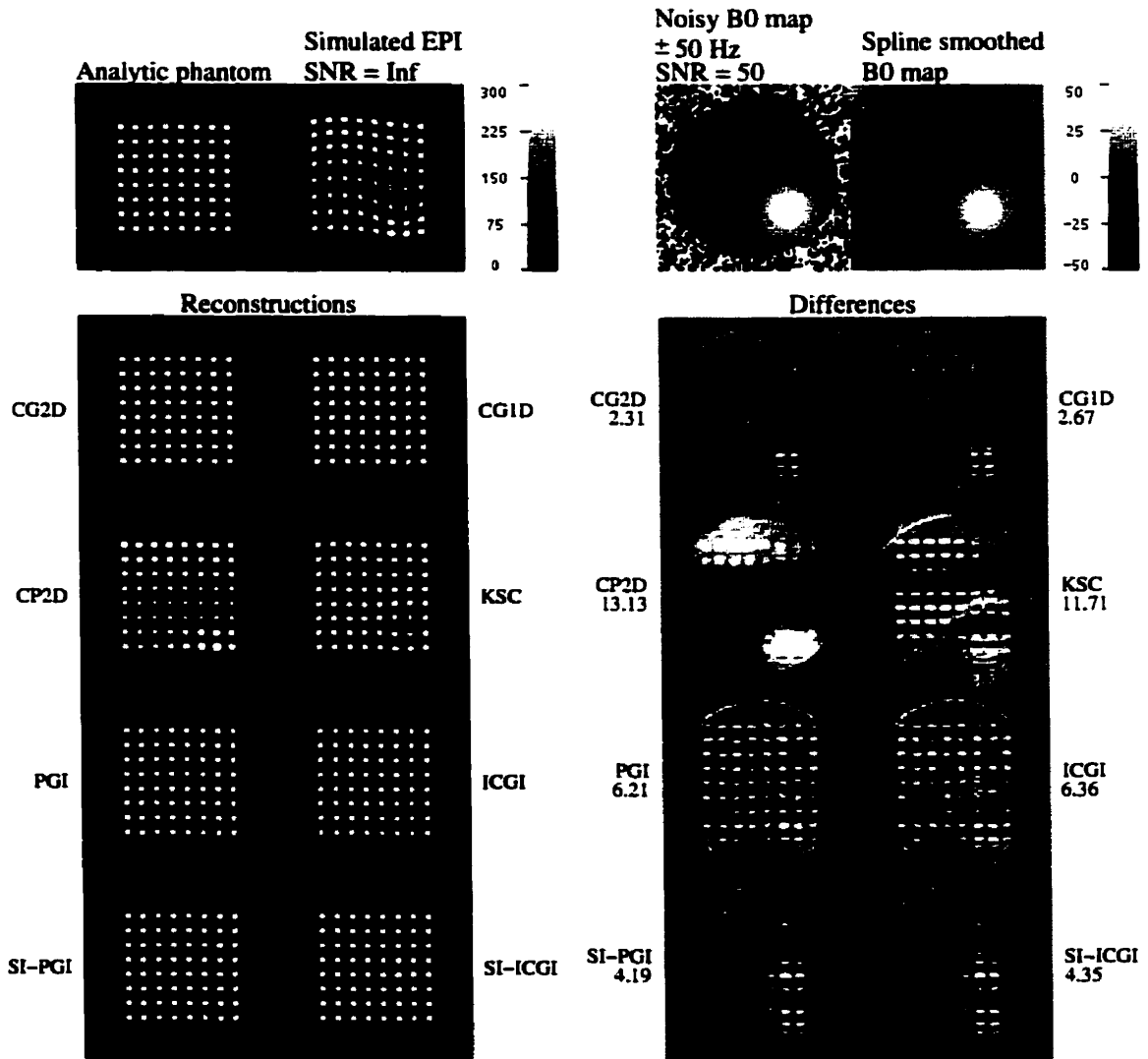


Figure 5.24: Correction with  $B_0$  SNR=50, maximum  $B_0$  amplitude =  $\pm 50$  Hz.

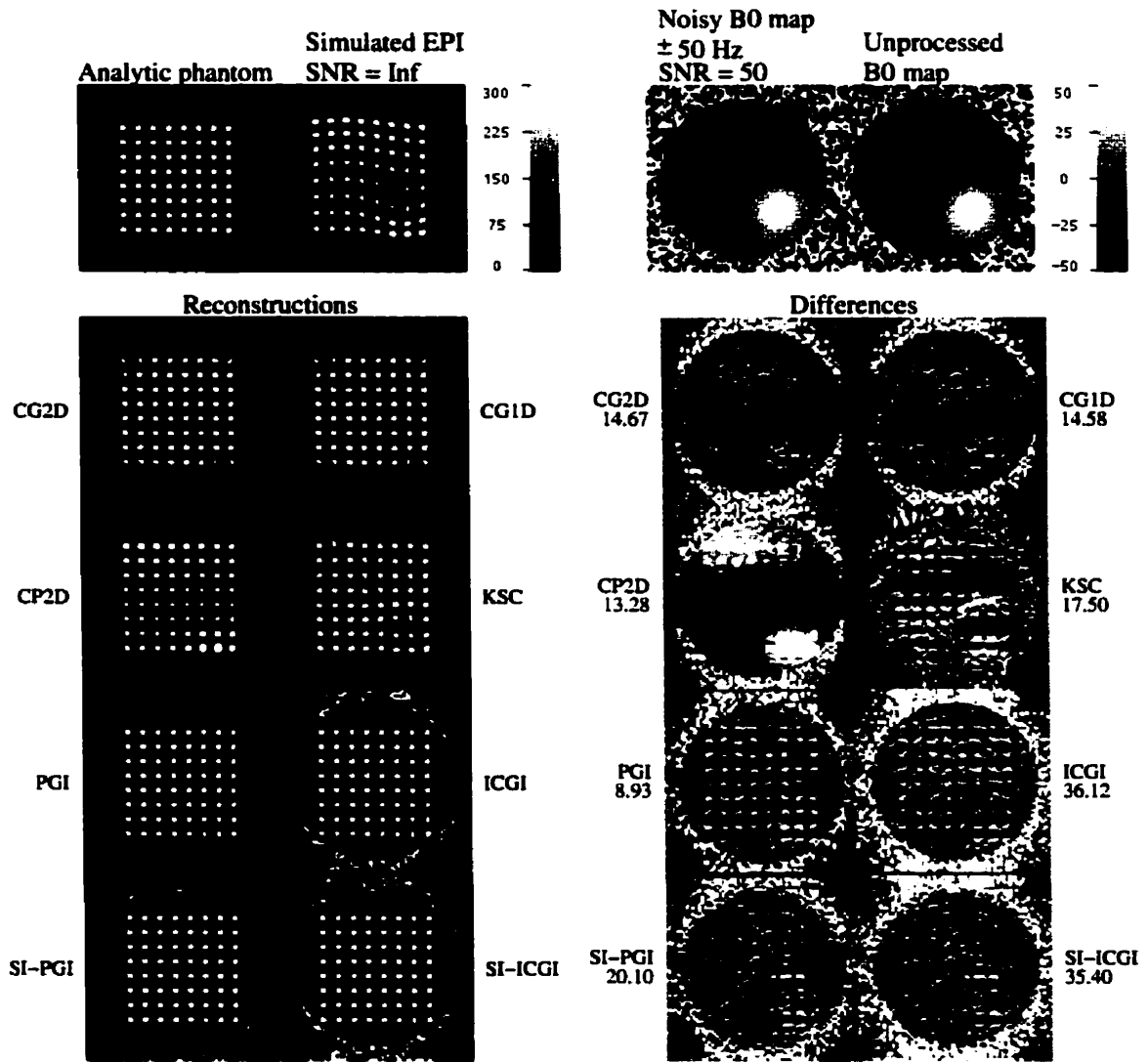


Figure 5.25: Correction with a noisy, unprocessed  $B_0$  map.

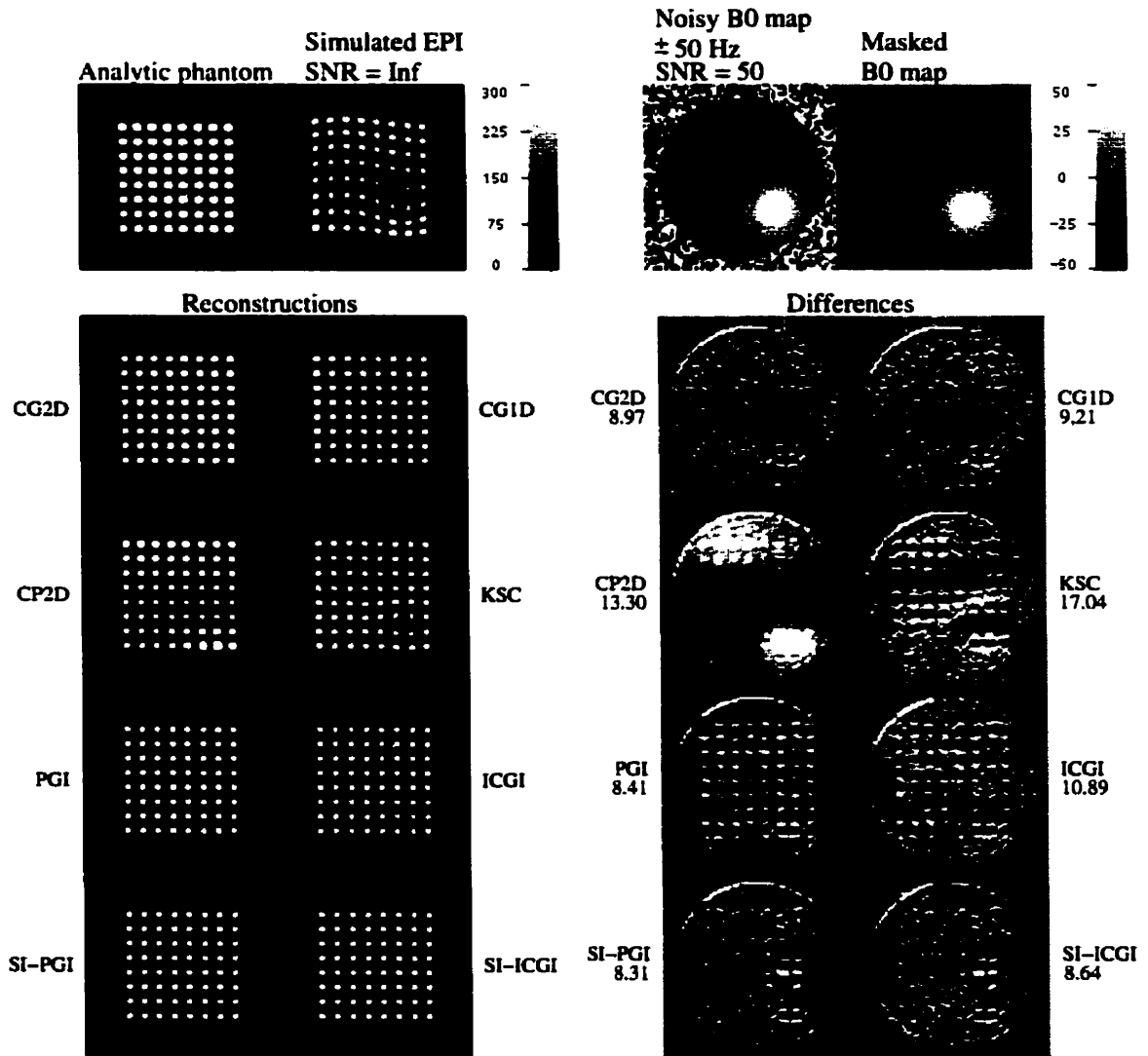


Figure 5.26: Correction with a noisy, masked  $B_0$  map.

## 5.4 Discussion

### 5.4.1 Effect of CG parameters

Figure 5.4 shows how the CG2D correction performs with different numbers of iterations. The 0 iteration case, which corresponds to the conjugate phase reconstruction, shows complete correction for distortion, but reveals important intensity errors. The most interesting fact is that with only one CG iteration, this intensity error almost completely disappears. Performing more iterations does little to improve the reconstruction, as seen by the slow decrease of the RMS errors after the first and the subsequent iterations. From the RMS errors, we can conclude that using 2 or 3 iterations is a good compromise between computation time and the level of correction.

The number of elements retained in the sparse kernel has a less obvious importance, as demonstrated by the fact that each reconstruction in Fig. 5.5 has a relatively small RMS error. However, using a larger number of elements helps to reduce the  $B_0$  induced ghost artifacts, as the difference images show. Note that the actual density needed for adequate ghost reduction depends on the amplitude of field inhomogeneity. Another important point is that for a larger matrix size (e.g.  $128 \times 128$ ) smaller density (relative to the matrix size) may be needed for the same amount of ghost reduction because the matrix size is proportional to  $N^4$  while the number of significant values in the kernel increases roughly as  $N^2$ .

In the 1D version of the CG correction method, the effect of the number of iterations is similar to that observed in the 2D version of the method (Fig. 5.6). Again 2 or 3 iterations seems to be the best choice.

The width of the diagonal band in the kernel for CG1D reconstruction has interesting consequences (Fig. 5.7). When it is smaller than the maximum amount of distortion (measured in pixels), important artifacts appear on the reconstructed image

(see reconstruction for widths 2 and 4 in Fig. 5.7). However, as long as the width of the central band of the kernel extends beyond the maximum distortions in the image, correction is near complete. Note that, since smaller widths have computation time advantages, the optimal width of the diagonal band depends on the level of distortion in the image to be corrected.

## 5.4.2 Comparison between the different methods for EPI correction

### Effect of EPI image noise

Several conclusions may be drawn from Figs. 5.9, 5.10 and 5.11. The CG methods perform better than the other methods in high SNR situations, with a small advantage for the CG2D method, due to its ability, unique among all the methods compared, to reduce ghosting artifacts, which can be seen on the difference images of the reconstruction examples of Figs. 5.12 to 5.20. This advantage of the CG2D method tends however to disappear at lower image SNR, when the artifact becomes overwhelmed by the noise.

One can also see that the RMS error of those methods increases faster as the EPI image noise level increases compared to other methods, suggesting a higher sensitivity to image noise. We note that 50–70 is a typical SNR for a  $64 \times 64$  EPI image.

The graphs of Figs. 5.9 and 5.10 also show that the sinc interpolated version of the PGI and ICGI method perform significantly better than the version using no interpolation. The CP2D and KSC methods have much larger errors than the others, due to the failure to account for intensity errors for CP2D, and to incomplete distortion correction, especially in large distortion situations, in KSC.

We also note that the performance of the SI-CGI and SI-ICGI is similar to CG1D

in small distortion situations (Fig. 5.9) but gets worse as the amount of distortion increases.

In large distortion situations (50-75 Hz), there is a region in the image that any method fails to properly correct (Figs. 5.15 to 5.20). This region corresponds to where the gradient of the  $B_0$  map is the largest and in a direction which causes a compression of the distorted image. In these regions, the distortion is so large that some information is permanently lost, since many image points are mapped to a unique spatial location. Just above this region is another of high  $B_0$  inhomogeneity gradient, but which causes the image to be stretched. CG1D and CG2D correct for this stretching while other methods fail to do so. One interesting fact is that in large distortion situations, the reconstructions with the sinc-interpolated methods (SI-PGI and SI-ICGI) present an important artifact in the high  $B_0$  inhomogeneity gradient region, making the total RMS error larger than the non interpolated versions of the same algorithms (Fig. 5.20). This behaviour is due to the presence of the high frequency components, in this region of the image, which cause the sinc-interpolation to fail.

The results of the simulation on  $B_0$  map noise (Fig. 5.22) demonstrates the effectiveness of the spline smoothing procedure performed on the  $B_0$  map prior to reconstruction. At a  $B_0$  SNR of 50 and 30, the residuals are very similar for all methods. The situation is quite different when the  $B_0$  map is not processed, as shown on Fig. 5.25, since the RMS errors are significantly larger than in Figure 5.24. The situation is not improved by masking out the noise background in the field map (Fig. 5.26).

### 5.4.3 General Discussion

The simulation presented in this chapter did not consider systematic errors in the computation of the field map. Probably the most important factor is the distortion

of the field map itself. In the case of EPI, distortions of the image are several times larger than the distortion of the field map, so they can be safely ignored. In the case of GE imaging however, the distortion of the field map may be of the same order of magnitude as that affecting the image to be corrected. Sekihara [96] has shown that this effect can be attenuated by correcting the distortion in the field itself before correcting the image. According to their report, this sort of bootstrapping procedure seems to correct for effects related to the geometrical discrepancy between the field map and the corrected image. Another way to minimize the effect of distortion in the field map is to acquire it with a large bandwidth sequence, i.e. a high readout gradient. The SNR price to be paid for this increased bandwidth is minimal considering that the field map need only be acquired at low resolution, and smoothing can be applied to reduce the noise without affecting the nature of the field map.

#### 5.4.4 Conclusion

This chapter described in detail several computer simulations having the goal to investigate the behaviour of the Conjugate Gradient based correction methods under different operating conditions, and to compare these methods with other  $B_0$  map based methods.

The first group of simulations allowed the optimal values for the parameters of the CG correction methods to be determined. The convergence of the CG methods was found to be fast, and a small number of CG iterations are usually needed for achieving satisfactory reconstruction.

In summary, the following conclusions may be drawn. The CG based methods provide more optimal solutions, in the RMS sense, than the other methods. CG2D could partially correct for  $B_0$  inhomogeneity induced ghosts artifacts. All other 1D methods failed in this respect, since they do not take this component of image degra-

dation into account. Moreover, CG-based methods, 1D and 2D, can better correct severe distortions that appear as a stretching of the image. The situation is different when the distortion compresses the image. The explanation in that severe compression of the image may result in a loss of information, which translates as many-to-one mapping, and numerical singularities in the kernel. It may be possible to somewhat improve the reconstruction of near-singular compressed image regions by using many more iterations, but even then, the noise sensitivity of the imaging equation must be somehow controlled, by using preconditioning for instance. Severe stretching distortions on the other hand, do not in general cause the kernel to be singular, and CG-based methods can correct for them.

The practical significance of ghost reduction in EPI images is not obvious because of the relatively small amplitude of those artifacts. They can be safely ignored in simple diagnostic applications where qualitative aspects of the image are considered. The situation may be different in applications, such as fMRI, where quantitative, statistical image analysis plays an important role and the significant signals are the result of small differences between images.

# Chapter 6

## Application to real data

The objective of this chapter is to illustrate and demonstrate the use of the Conjugate Gradient method for the correction of real EPI images and anatomical gradient echo images.

### 6.1 Methods

#### 6.1.1 EPI imaging

The practical implementation of the CG gradient method is the same as that presented in the previous chapters. It involves the measurement of a  $B_0$  map, which is acquired at the same spatial resolution and geometry as the EPI image to be corrected.

#### 6.1.2 3D anatomical imaging

The theory developed in the previous chapters, more specifically the 1D correction procedure, can be applied to anatomical 3D imaging with few modifications. In this case, the main aspect to be addressed is the computing time.

The distortion caused by static field inhomogeneity in 3D Fourier imaging has

an effect only in the frequency encoding (readout) direction. Hence, a  $N \times M \times S$  volume, where  $N$ ,  $M$  and  $S$  refer to the dimensions in the frequency encoding, phase encoding and 3D partition directions respectively, can be corrected from the effect of  $B_0$  inhomogeneity by performing  $M \times S$  1D corrections along the frequency encoding direction.

The assessment of the distortion correction is more difficult in gradient echo imaging due to the much smaller distortions typically observed. In order to evaluate the distortion correction by the CG method, a pair of image volumes acquired in the same geometry and at the same spatial resolution were acquired. One of the two acquisitions used a large readout bandwidth (520 Hz/pixel) while the other, a small bandwidth (32 Hz/pixel). Because of the relationship between readout bandwidth and distortion, one may expect the distortion on the high bandwidth sequence to be around 16 times smaller (520/32). Then, the correction can be applied on the low bandwidth data, and the result compared to the high bandwidth image considered as the “gold standard”. The high and low bandwidth imaging sequences are displayed in Fig. 6.1.

## 6.2 Results

### 6.2.1 Correction of real EPI images

The CG and CP correction methods were applied to real blipped EPI images of a phantom and of a volunteer’s head (matrix size =  $64 \times 64$ , TE = 35 ms, T<sub>acq</sub> = 61 ms) on a Siemens Vision 1.5 T scanner. Non-uniform sampling of the signal was performed in order to obtain equally spaced points in k-space. This non-uniform sampling has been taken into consideration in the calculation of the kernel in Eq. (4.1). No phase correction was applied to the EPI raw data.

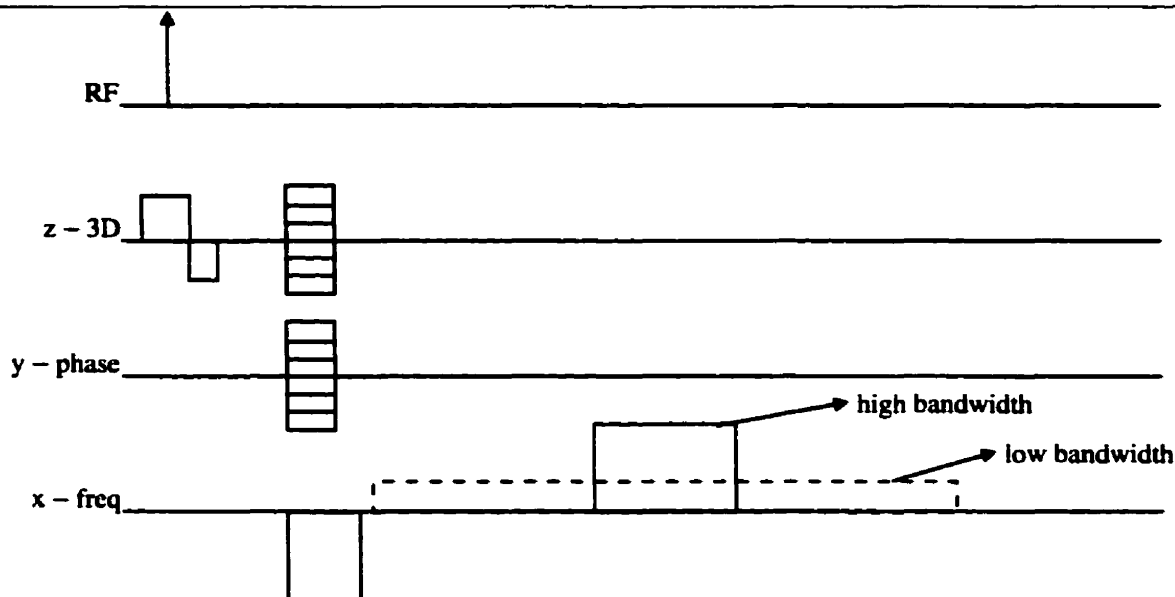


Figure 6.1: High and low bandwidth gradient-echo 3D imaging sequences. *Image sequences used for the gradient echo example. Two data sets, with different bandwidths, were acquired with a gradient-echo sequence. The inverse of the total readout duration is the bandwidth per pixel.*

A normal spin echo sequence (matrix size =  $64 \times 64$ ,  $TE_1/TE_2/TR = 10/14.48/400$  ms), interleaved with a second sequence having the echo shifted by  $\Delta t = 4.480$  ms, was used to generate the  $B_0$  map (Fig. 6.2). The  $B_0$  field map was obtained by subtracting the phases of the two acquisition. With this value of  $\Delta t$ , water and fat protons, although precessing at different rates, demonstrate the same relative phase at  $TE$  and  $TE + \Delta t$ , which makes the phase difference observed between the two acquisitions dependent upon static field inhomogeneity only and not to chemical shift [46]. We found that, for this example, phase unwrapping was not required. We note that, although the acquired field map is itself subject to distortion due to field inhomogeneity, the magnitude of these distortions is negligible compared to the distortions affecting the EPI image.

For the acquisition of both the phantom and the volunteer head data, the field map was fitted with 2D splines in order to minimize noise effects.

In both the CG2D and CP2D methods, the 4D kernel needs to be computed. This took around 5 minutes for this example. The CG iterations, performed for the CG2D method, took a few seconds to complete.

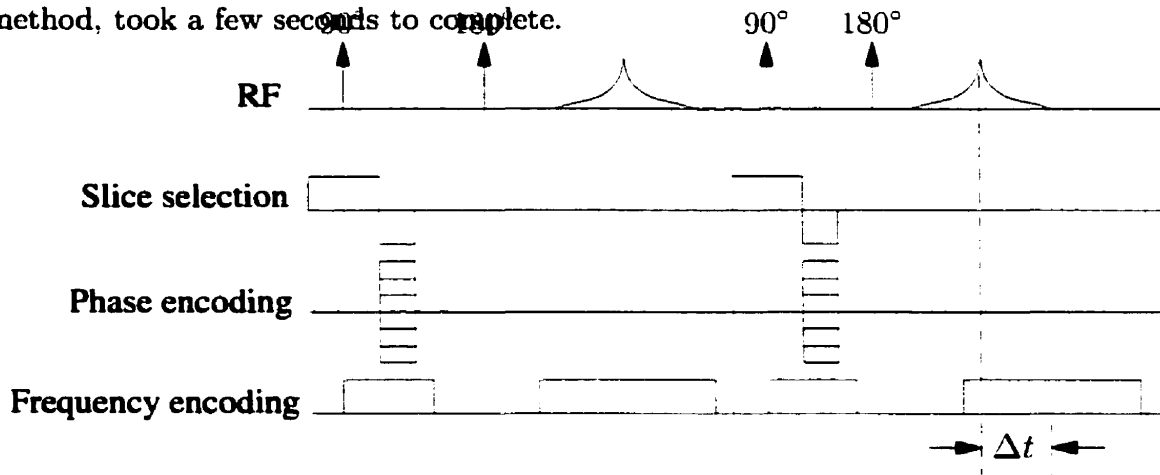


Figure 6.2:  $B_0$  field mapping sequence.

*In this sequence, two data sets are acquired in an interleaved manner. The first acquisition is a standard spin-echo. The second echo is acquired asymmetrically with respect to the spin-echo signal, with a time difference between the spin-echo and the gradient echo equal to  $\Delta t$ . The  $B_0$  map is obtained from the difference of the phase images  $\Delta\phi$  resulting from the reconstruction of the two data sets. At any point of the image, the frequency offset with respect to the nominal resonance frequency is given by  $\Delta f = \Delta\phi / (2\pi\Delta t)$ .*

### 6.2.2 Results of correction of a 3D flash image

Two volumetric data sets, with a matrix producing isotropically resolved voxels of  $1 \times 1 \times 1 \text{ mm}^3$ , were acquired with bandwidths  $32 \text{ Hz/pixel}$  and  $520 \text{ Hz/pixel}$  respectively. For the high bandwidth sequence  $\text{TR}/\text{TE} = 11.6/5.2 \text{ ms}$  and for the low bandwidth

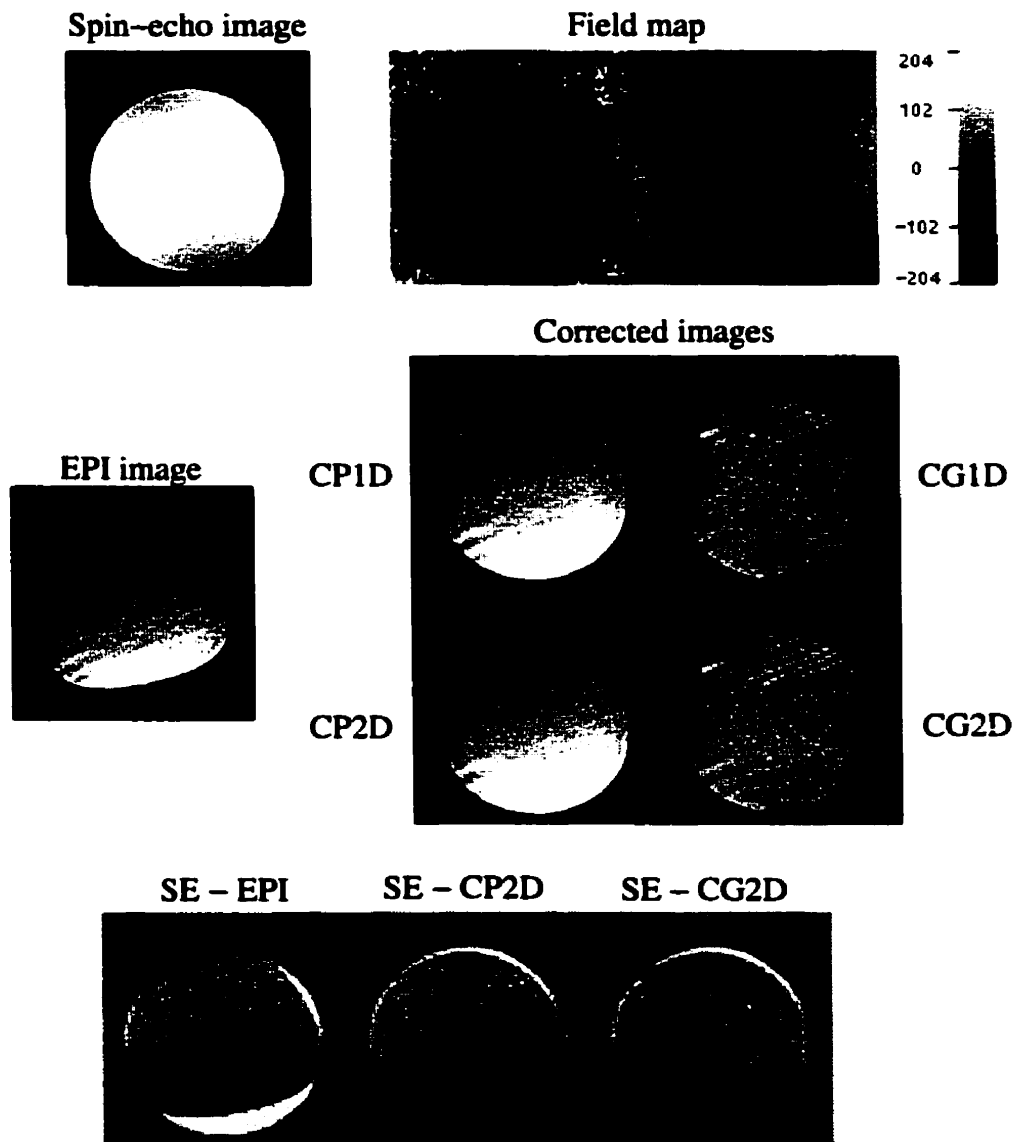


Figure 6.3: CP and CG reconstructions of the EPI image of a phantom. The top images show a spin-echo image of the phantom along with a raw and a processed field map. The center images, are an EPI image of the same phantom (left) and the reconstruction with the CP1D, CP2D, CG1D and CG2D methods. In the bottom images, the difference between the spin echo image and the EPI image, CP2D and CG1D corrections respectively is displayed.

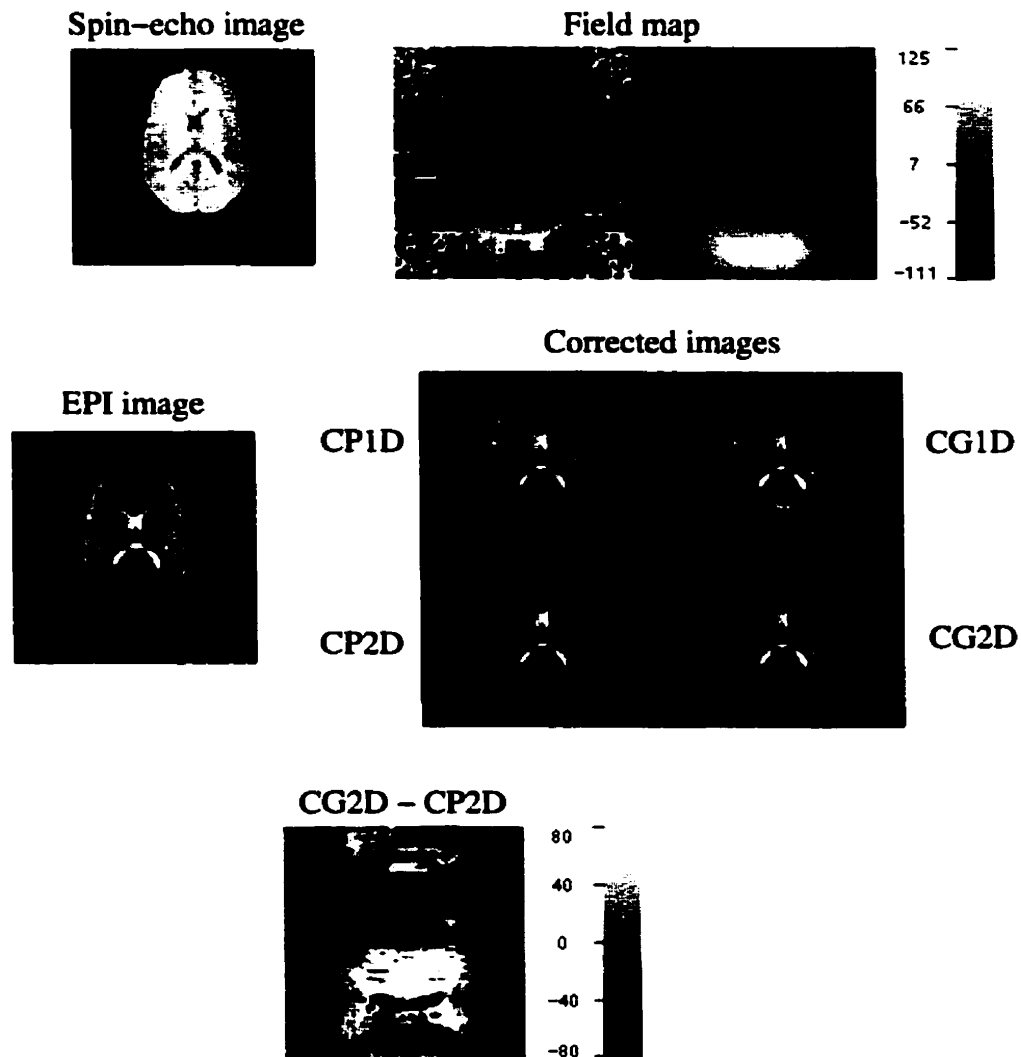


Figure 6.4: Distortion correction on a volunteer's head EPI image.

The top images show a spin-echo image of the volunteer's head along with a raw and a processed field map. The center images, are an EPI image of the same volunteer's head (left) and the reconstruction with the CP1D, CP2D, CG1D and CG2D methods. In the bottom images, the difference between the CG2D and CP1D corrections is displayed.

sequence,  $TR/TE = 40.4/19.6$  ms.

A 3D gradient-echo  $B_0$  map sequence was also acquired ( $TR/TE = 52/5.2$  ms) with a  $2 \times 2 \times 2$  mm<sup>2</sup> resolution.

Fig. 6.5 shows the result of CG reconstruction of an image of the 3D flash acquisition. The comparison is qualitative here, but the difference images display some reduction of the distortion of the low bandwidth image compared to the high bandwidth image. The correction of the whole volume with the CG1D method took approximately 2 hours.

## 6.3 Discussion

### 6.3.1 EPI

The EPI examples, shows that both the CG and CP methods significantly reduce the geometrical distortions. Moreover, the CG methods, as opposed to CP, can be seen to also correct for intensity errors. This intensity correction is more obvious on the phantom image, because of its flat intensity profile. This is borne out by the simulations.

These two examples do not show the difference between 1D and 2D processing. This is because other factors cause  $N/2$ -ghosting that masks the  $B_0$  inhomogeneity related ghost artifacts. Among these factors, we mention ADC offset and eddy currents, because they can induce non-ideal effects that affect differently odd and even k-space lines.

The in-vivo experiment (Fig. 6.4) demonstrates again that the best performance is achieved by the CG1D and CG2D approaches. The intensity correction provided by CG method can be seen on the difference image CG2D – CP1D.

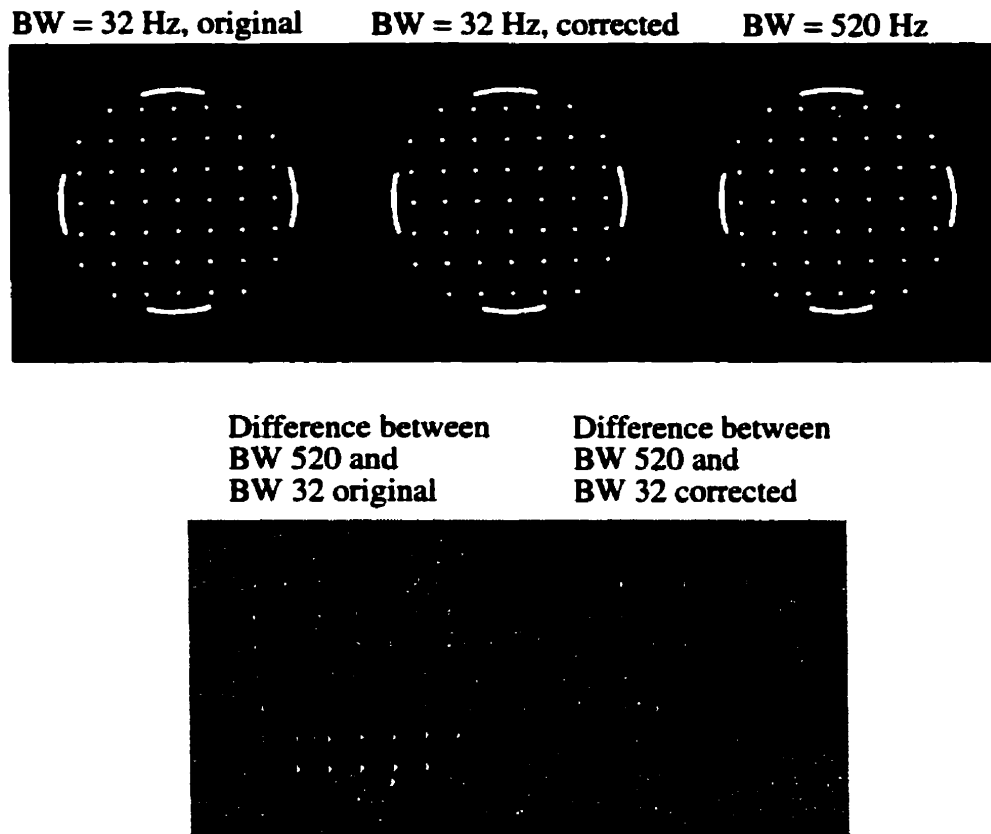


Figure 6.5: Distortion correction a flash acquisition with the CG1D method. *The top left image is taken from a 3D data set acquired with small bandwidth, while the top right image is acquired with a large bandwidth. Because the inverse relationship between bandwidth and distortion, the large bandwidth sequence is expected to represent the reality more closely than the low bandwidth image. The Top centre image is the corrected low bandwidth image. The bottom images show the different between the low and high bandwidth images before and after CG1D correction.*

### 6.3.2 Gradient-echo imaging

The simulations for EPI have shown that the 1D version of CG reconstruction performs in a manner similar to the sinc-interpolated geometric interpolation methods. This points out the fact that using CG for 1D problems may be overkill, particularly in the case of small distortion, considering the significantly longer processing time re-

quired. We nevertheless present an example of CG correction on a real gradient-echo acquisition, with the purpose of demonstrating the general applicability of the CG correction method to this kind of data.

In the case of 3D imaging, for a 1 mm isotropic resolution, the acquisition time for a  $256 \times 256 \times 128$  scan can be of the order of 15 minutes. Because the duration of the acquisition alone is considerable, the associated field map should be acquired as fast as possible. The easiest way to measure the field map quickly is to reduce the spatial resolution. For a factor of 2 or 4 reduction in spatial resolution, the scan time is reduced by a factor of 4 or 16, to around 4 or 1 minutes respectively. Furthermore, since the field map is inherently a low frequency function, and that it undergoes further smoothing for noise reduction (e.g. spline fitting, low-pass filtering), the penalty for measuring a field map with lower resolution than the image to be corrected appears to be small. Moreover, from the simulation results that have shown that the CG methods are somewhat sensitive to field map noise, using the lower spatial resolution field map has the additional advantage of presenting a higher SNR.

## 6.4 Summary

This chapter demonstrates the practical application of the CG based methods, both on EPI images and a gradient-echo image. In the case of EPI image correction, both the CP and CG methods reduced the geometrical distortion equally well. Moreover, the ability for the CG methods to better compensate for intensity inhomogeneity than CP methods, as observed in the simulations of the previous chapter, was clearly demonstrated in the phantom EPI example. These examples do not show, however, the advantage of full 2D correction versus 1D processing, because  $B_0$  inhomogeneity induced ghost artefacts were not the most important ghost artifact on these images.

For gradient-echo correction, the 1D CG and CG methods were applied. In order to somewhat assess the distortion correction, two data sets were acquired: one with small bandwidth and relatively large distortion, and one with large bandwidth and little distortion. The second data set was used as a reference against which the CG correction of the first data set was compared. Results showed an improvement of the geometrical accuracy after the correction.

# Chapter 7

## Conclusions

This thesis has dealt with the issue of distortion and image restoration in MRI. Geometrical distortion is often more difficult to identify than other artifacts, and therefore may not be readily appreciated. Small amounts of distortion are virtually impossible to distinguish visually without relying on an external reference, but can cause localization errors that can reach several millimeters. Obviously this extreme precision is not needed in every applications but one must always be suspicious.  $B_0$  inhomogeneity induced ghosting artifact in EPI images, although usually very small, can nevertheless have important consequences, especially in fMRI studies, where time-varying patterns of pixel intensity that are barely larger than the noise level are considered [60, 58, 32].

Beyond the diagnostic applications, MRI is increasingly being considered as an aid for therapeutic purposes, such as MR Image-Guided surgery or radiotherapy [85, 31, 6], because of its ability to exhibit anatomical and functional characteristics complementary to those obtained from other imaging modalities. This is where the geometric accuracy is essential and the issue of geometrical distortions in MR images arises.

Radio-therapy is a field where MR images are increasingly relied upon. Computed

Tomography (CT) already plays an important role in this field, because the electronic density of tissues can be directly obtained from the CT images, allowing treatment planning software to perform tissue inhomogeneity corrections and compute a more accurate dose distribution. In spite of this, MR may be of great utility as a guide to determine the extent of regions to treat and this is where MR distortion becomes a concern. With the advent of IMRT (Intensity Modulating Radio-Therapy) [110, 86], dose distributions can be tailored with much more precision than with conventional static techniques and the issue of the accurate delimitation of the region to be treated needs to be addressed even more.

Still in the domain of radio-therapy, MR has been used for some time as a tool for relative dosimetry [30, 16, 79]. It is particularly useful in applications where 3D dose distributions are needed and difficult to obtain by other means, such as curie-therapy, where radioactive sources are inserted into the patient, and can also be an essential tool for the quality assurance of complicated dynamic treatment techniques. Because the spatial dose distribution is inferred from the MR scans of a volume of Fricke gel, any geometrical and intensity distortions in these images will result in errors on the measured dose distribution.

## 7.1 Thesis Summary

The thesis begins by introducing the main motivations and objectives for this work. Correction of distortion in EPI images and anatomical imaging (such as 3D gradient echo) are identified as the main objectives.

The second chapter presents a summary of MR imaging theory, from basic physical theory to imaging principles. Concepts needed throughout the thesis, such as EPI imaging,  $B_0$  field mapping, the mathematics and physics of distortion, and Conjugate

Gradient method, were also briefly explained.

Chapter 3 reviews the main published distortion correction methods, focusing on  $B_0$ -map based methods. The relevance of the  $B_0$ -map based methods over the others for distortion correction of dynamic EPI data and large anatomical data sets have been discussed.

The fourth chapter begins the mathematical analysis of the EPI distortion problem, and showed that in EPI, because of the particular k-space trajectory, the artifacts induced by  $B_0$  inhomogeneity are more complicated than in normal 2D or 3D Fourier imaging. In addition to the usual distortion, ghosting artifacts are present. The formalism for the proposed 2D correction method is developed together with a simplification of the computation process based on the low rank of the k-space trajectory matrix. For cases where the distortions are approximately or truly one dimensional, the 1D specialization of the method is also derived, allowing the computational complexity of the correction problem to be dramatically reduced from a large  $MN \times MN$  problem to  $N$  small  $M \times M$  problems.

Chapter 5 presents the main results of the thesis, based on computer simulations. The goal of this chapter is two-fold: it allows the effect of different parameters involved in the Conjugate Gradient reconstruction in 1D or 2D to be studied, as well as the different  $B_0$ -map based methods to be compared. This chapter discusses in detail the various aspects of the simulations and presents results in both quantitative and qualitative forms.

A few examples of the application of the CG-based correction methods on actual MR scans are shown in Chapter 6. The objective is to demonstrate that these techniques are applicable to real-life problems, and discusses the particularity of applying the correction methods on real data. The problem of the validation of the correction in a real situation was not addressed in detail however.

In Appendix A are included the Matlab source code of the main functions that constitute the implementation of the 1D and 2D CG methods, together with that of other  $B_0$  map based methods. We believe that it is important that results of this thesis can be accurately reproduced, used and, doubtlessly, improved by other researchers. Due to the nature of numerical computations, where small differences in implementation may cause notable changes in the results, the only way to ensure that the implementation of algorithms found in this thesis is clear for everybody is to include the source code. The possibility of implementation errors are unfortunately always possible (although rigorous verification and testing can minimize this possibility) and submitting the source code is a way to eventually unmask these bugs. Beyond bugs, the possibility that the algorithms have not been fully optimized is even more likely, if not certain. Considering the substantial computation effort needed to apply some of these algorithms, optimization may make a non negligible difference when using them in a clinical environment.

## 7.2 Main findings

The inverse problem approach was first suggested by Kadah and Chu [54] in order to correct for 1D distortion problems, i.e. when the image degradation is only in one direction. We have gone further by implementing a 2D version of this correction approach, which can potentially eliminate second order ghosting artifacts, in addition to geometrical distortion.

The 2D implementation of the inverse problem method involves a very large system of equations. For example, a  $4096 \times 4096$  system of equations is required for the 2D correction of a modest  $64 \times 64$  image. The storage requirement for such a linear system in complex form and double precision is  $4096 \times 4096 \times 2 \times$

$8(\text{bytes})/1024(\text{bytes/kB})/1024(\text{kB/MB}) = 256\text{MB}$ . For a  $128 \times 128$  image size, the full storage requirement would be of 4Gb. Therefore, direct methods of solutions (pseuso-inverse, SVD, Gaussian elimination) are not practical for this sort of problem due to the size of the equation systems involved.

In this thesis, approximations and computational methods were developed to make the 2D restoration problem practically achievable in the case of the blipped, single-shot EPI sequence, with modest computer hardware and in reasonable times. The key element of this simplification is to recognize that the equation system representing the imaging process is sparse when expressed in image space. This fact allows the useful information in the kernel of the system of equations to be stored in many fewer elements than  $M^2 \times N^2$ , for a  $M \times N$  image size.

We have found that the most computationally intensive part of the 2D correction is the computation of the sparse kernel. Chapter 4 showed that the complexity for the calculation of the kernel can be reduced by exploiting the low-rank characteristic of the EPI blipped sequence k-space trajectory.

The inverse problem method is more elegant and mathematically rigorous, but is more time consuming than other more direct approaches. It was found that the power of the inverse problem approach could potentially be beneficial in EPI image restoration. But even in this case, other factors prevented us from clearly demonstrating this benefit in-vivo. Furthermore, CG based methods have been shown to better deal with large distortions that stretch parts of an image. When distortion appears as a compression of the image, information may be irretrievably lost and CG methods may fail, like the other methods, to correct the image.

## 7.3 Future Work

A number of important issues have not been addressed in this thesis. This section identifies some of them and suggests avenues of investigation.

### 7.3.1 In-Vivo Experimental validation: MR tagging

The absolute in-vivo validation of a distortion correction technique is not an easy problem due to the fact that “reality” may not be known. For this purpose, the use of tagging sequences, such as Spatial Modulation of Magnetization (SPAMM) [2, 68, 114] and DANTE sequences [71] may be considered. The principle is to apply a tagging pulse that produce a pattern of parallel strips, or a grid, on top of the imaged object, before each repetition of a normal acquisition sequence. The geometrical distortion then appears as a deformation of this strip pattern. Two or three strip patterns can be applied in sequence so as to form a two-dimensional or three-dimensional grid. Tagging methods such as these have been used for other reasons than the assessment of geometrical distortion, for instance motion measurement [82, 3] and estimation of in-vivo spatial resolution [104].

### 7.3.2 Field map acquisition and processing

The essential element of the CG method, and many other reconstruction methods is the field map. Whichever method is used, the correction can be only as good as the field map is accurate and representative of the real static field distribution. Consequently, an important part of the improvement of  $B_0$ -based correction methods relies on the field map acquisition and processing side.

It has been shown that the CG method is somewhat sensitive to the noise in the  $B_0$  field map, and that some processing must be performed in order to reduce its noise

prior reconstruction. The best approach we have found so far is to perform spline smoothing on the field map. However, this can be time and memory consuming for large data sets. It would be interesting to consider other field-map processing methods, and particularly edge preserving noise-reduction methods, such as Anisotropic Diffusion [44], or Wavelet Packet Filtering [111] which may be considered for such a task.

Another aspect of field map processing that has not been addressed in this work concerns phase unwrapping [46, 101], which is necessary when the magnitude of the field map exceeds the dynamic range allowed by the field map sequence. This problem is not as simple as it may seem for complicated images containing small regions isolated from the rest of the image. Furthermore, the low resolution of the field map can complicate the task of accurately determining where phase wraps occur.

## 7.4 Concluding remarks

MRI imager technology improves every day. Magnetic field homogeneity is constantly improving, gradient fields are increasingly more linear and stable. One factor that cannot be improved is the subject dependent susceptibility induced field inhomogeneity. Better shimming can improve the situation, but high order shims are needed to take the full complexity of subject-induced field inhomogeneity into account. With the improvement of the technology, such subject dependent factors may likely become the dominant effects as the other design-related factors are reduced. On the other hand, the tremendous increase in computing power may suggest that methods that are ignored today, because of their large computing cost, may find some applications in the future.

While MR technology continues to improve, MR imaging is being applied in in-

creasingly difficult conditions. For instance, interventional MRI [43, 61] uses open magnets where it is difficult to obtain good field homogeneity. In such circumstances, image correction methods may have an important role in the future, considering that the processing power is likely to improve as well.

In this thesis, we have added a new method to an already large set of correction approaches. Since no single correction method or imaging sequence will ever solve all the problems encountered in the complex reality of MRI, a variety of available options is the best guarantee that magnetic resonance imaging will continue to evolve and improve as a diagnostic, treatment support and basic research modality. We modestly hope that this work will contribute to this evolution.

# Appendix A

## Source code

### A.1 CG 2D algorithm

```
function A = kernel4d(B0, traj, thresh)
%
% A = kernel4d(B0, traj, thresh)
%
% Computes the 4D EPI kernel from a B0 map and a k-space trajectory
%
% Input:      B0:      MxN B0 map (Hz)
%             traj:    EPI trajectory (s)
%             thresh:  sparsity threshold (% of maximum value)
%
% Output     A:      MxNxMxN 4D sparse kernel
%
% get image dimensions
[M,N] = size(B0);

% compute singular value decomposition of the k-space trajectory
[U,S,V] = svd(traj);

% allocate space for sparse matrix
A=sparse(M*N,M*N);

% loop over image pixel coordinates
for (jj=-N/2:N/2-1)
    for (ii=-M/2:M/2-1)
        % computes the rank-two decomposition of the EPI PSF
        [u1,u2,v1,v2] = psf_dec(U,S,V,B0(ii+M/2+1,jj+N/2+1),ii,jj);
```

```
% computes PSF
PSF = u1*v1+u2*v2;

% set elements smaller than threshold to zero
PSF(abs(PSF)<thresh/100) = 0;

% compute column index in the 4D kernel
rr = (ii+M/2)+(jj+N/2)*N+1;

% fill up one column of the 4D kernel
A(:,rr) = sparse(PSF(:));
end;
end;
```

```

function [p1,p2,q1,q2] = psf_dec(U,S,V,dB,m,n)
%
% [p1,p2,q1,q2] = psf_dec(U,S,V,dB,m,n)
%
% Computes the rank-two EPI PSF decomposition, i.e.
% the 4 vectors p1,p2,q1 and q2 such that
%  $p1*q1 + p2*q2 = PSF$ 
%
% Input:  [U,S,V]      Singular value decomposition of the k-space
%          dB          Local field inhomogeneity
%          [m,n]      Pixel location
%
% Output: p1          main PSF component column vector
%          p2          ghost PSF component column vector
%          q1          main PSF component row vector
%          q2          ghost PSF component rowvector
%
%
M = size(U,1);
N = size(V,1);

U1 = U(:,1);
U2 = U(:,2);
V1 = V(:,1);
V2 = V(:,2);
S1 = S(1,1);
S2 = S(2,2);
k = (-M/2:M/2-1)'/M;
l = (-N/2:N/2-1)/N;

tmp1 = exp(-2*pi*i*(k*m+dB*S1*V1(1)*U1));

p1 = fftshift(iff(fftshift(tmp1)));
p2 = fftshift(p1);

tmp1 = cos(2*pi*(dB*S2*U2(1)*V2')).*exp(-2*pi*i*l*n);
q1 = fftshift(iff(fftshift(tmp1)));
tmp2 = -i*sin(2*pi*(dB*S2*U2(1)*V2')).*exp(-2*pi*i*l*n);
q2 = fftshift(iff(fftshift(tmp2)));

```

```
function x = cg2(A,b,nit)
%
% x = cg2(A,b,nit)
%
% Solves A'A x = A' b
% with the conjugate gradient method.
% A'b is taken as the initial guess.
%
% Input:  A           MxN Matrix A
%         b           Mx1 Constant vector b
%         nit        Number of iterations
%
% Output: x          Nx1 solution vector x
%

tol = 1e-4;
x=A'*b;
ii = 0;
r = A'*(b-A*x);
d = r;
delta_new = r'*r;
delta_old = delta_new;

for ii=1:nit
    q = A'*(A*d);
    alpha = delta_new/(d'*q);
    x = x+alpha*d;
    r = r-alpha*q;
    delta_old = delta_new;
    delta_new = r'*r;
    beta = delta_new/delta_old;
    d = r+beta*d;
end;
```

## A.2 1D CG algorithm

```
function A = A_mat(delta,ndiag)
%
% A = A_mat(delta,ndiag)
%
% Computes the A matrix for 1D correction
%
% Input:      delta   Nx1 distortion vector (in pixel units)
%            ndiag   Width of main diagonal.
%
% Output:     A       NxN matrix
%
% get vector dimension
N = length(delta);

% set default value for ndiag
if ( nargin==1 )
    ndiag=N;
end;

% allocate space for kernel A
A =zeros(N);

% loop over elements
for (ii=0:N-1)
    for (jj=circ_ind([round(ii-ndiag/2):round(ii+ndiag/2)],N))
        tmp = ii-jj-delta(ii+1);
        tmp2 = tmp/N;
        if (tmp~=0)
            s = sin(pi*tmp)/sin(pi*tmp2);
        else
            s = N;
        end;
        A(ii+1,jj+1) = exp(-pi*i*tmp2)*s;
    end;
end;
```

```
function undist = CG_1D(dist,B0,traj,nit,ndiag)
%
% undist = CG_1D(dist,B0,traj,nit)
%
% Applies the CG method to all columns of an image.
%
% Input: dist      MxN distorted image
%        B0        MxN field map (Hz)
%        traj      MxN k-space trajectory (s)
%        nit       number of CG iterations
%        ndiag     width of diagonal band of the kernel
%
% Output: undist   MxN corrected image
%
% get image dimensions
[M,N] = size(dist);

% set defaults
if nargin < 5
    ndiag = M/4;
end
if nargin < 4
    nit = 3;
end

% allocate space for corrected image
undist = zeros(M,N);

% loop over columns
for jj=1:N

    % effective bandwidth
    BW = 1/(traj(M,jj)-traj(1,jj));

    % compute kernel
    A = sparse(A_mat(B0(:,jj)/BW,ndiag));

    % apply CG on column
    undist(:,jj) = cg2(A/M, dist(:,jj), nit);

end;
```

## A.3 PGI and SI-PGI algorithms

```

function undist = PGI(dist,delta)
%
% undist = PGI(dist,delta)
%
% Implementation of the Weis's correction method
%
% Input:      dist      Mx1 distorted profile
%            delta      Mx1 pixel displacement vector (in pixel units)
%
% Output:     undist    MxN corrected profile
%
%
% REF:  Weis, J. and Budinsky, L., Simulation of the influence of
%       magnetic field inhomogeneity and distortion correction
%       in MR imaging.
%       Magnetic Resonance Imaging 8(4), pp 483-9, 1990.
%
%
M = length(dist);
undist = zeros(M,1);
for ii=2:M-1
    L = ii-0.5+0.5*(delta(ii-1)+delta(ii));
    R = ii+0.5+0.5*(delta(ii)+delta(ii+1));
    Ilp = round(L);
    Irp = round(R);
    % make sure indices are valid
    if (Ilp<1) Ilp = 1; end;
    if (Ilp>M) Ilp = M; end;
    if (Irp<1) Irp = 1; end;
    if (Irp>M) Irp = M; end;
    Dl = L-(Ilp-0.5);
    Dr = R-(Irp-0.5);
    n = Irp-Ilp+1;
    if n>1
        undist(ii) = (1-Dl)*dist(Ilp) + Dr*dist(Irp);
        for(kk=Ilp+1:Irp-1)
            undist(ii) = undist(ii)+dist(kk);
        end;
    else
        undist(ii) = (Dr-Dl)*dist(Ilp);
    end;
end;
end;

```

```
undist(1) = dist(1);  
undist(M) = dist(M);
```

```

function undist = PGI_1D(dist,B0,traj,nint)
%
% undist = PGI_1D(dist,B0,traj,nint)
%
% Applies the PGI method to all columns of an image.
%
% Input: dist      MxN distorted image
%        B0        MxN field map (Hz)
%        traj      MxN k-space trajectory (s)
%        nint      number of points for sinc interpolation
%
% Output: undist   MxN corrected image
%
% get image dimensions
[M,N] = size(dist);

% set default: no interpolation
if (nargin < 4)
    nint = M;
end;

% allocate space for corrected image
undist = zeros(M,N);

% loop over columns
for jj=1:N

    % effective bandwidth
    BW = 1/(traj(M,jj)-traj(1,jj));

    % interpolation
    if (nint > M)
        % interpolates to nint points
        dist2 = interpft(dist(:,jj),nint);
        B02   = B0_interp(B0(:,jj)/BW,nint);

        % apply PGI on interpolated data
        tmp = PGI(abs(dist2),B02);

        % interpolate back to original size
        undist(:,jj) = interpft(tmp,M);

    % no interpolation

```

```
elseif (nint == M)
    undist(:,jj) = PGI(abs(dist(:,jj)), B0(:,jj)/BW);

% not a good idea
else
    error('PGI_1D: invalid interpolation parameter')
end;

end;
```

```
function undist = ICGI(dist,delta)
%
% undist = ICGI(dist,delta)
%
% Implementation of the Intensity Compensated Geometrical Interpolation
% method.
%
% Input:      dist      Mx1 distorted profile
%            delta      Mx1 pixel displacement vector (in pixel units)
%
% Output:     undist     MxN corrected profile
%
% REF: Sekihara, K. and Kuroda, M. and Kohno, H., Image restoration from
% non-uniform magnetic field influence for direct Fourier NMR imaging.
% Phys. Med. Biol. 29(1), pp. 15-24, 1984
%
M = length(dist);
undist = zeros(M,1);
for ii=1:M-1
    g = ii+delta(ii);
    Ip = floor(g);
    % make sure Ip is fine
    if (Ip<1) Ip = 1; end;
    if (Ip>M-1) Ip = M-1; end;
    D = g-Ip;
    undist(ii) = ( (1-D)*dist(Ip) + D*dist(Ip+1) ) * ...
                ( 1+ delta(ii+1)-delta(ii) );
end;
undist(M) = dist(M);
```

```
function undist = ICGI_1D(dist,B0,traj,nint)
%
% undist = ICGI_1D(dist,B0,traj,nint)
%
% Applies the ICGI method to all columns of an image.
%
% Input: dist      MxN distorted image
%        B0        MxN field map (Hz)
%        traj      MxN k-space trajectory (s)
%        nint      number of points for sinc interpolation
%
% Output: undist   MxN corrected image
%
% get image dimensions
[M,N] = size(dist);

% set default: no interpolation
if (nargin < 4)
    nint = M;
end;

% allocate space for corrected image
undist = zeros(M,N);

% loop over columns
for jj=1:N

    % effective bandwidth
    BW = 1/(traj(M,jj)-traj(1,jj));

    % interpolation
    if (nint > M)
        % interpolates to nint points
        dist2 = interpft(dist(:,jj),nint);
        B02   = B0_interp(B0(:,jj)/BW,nint);

        % apply ICGI on interpolated data
        tmp = ICGI(abs(dist2),B02);

        % interpolate back to original size
        undist(:,jj) = interpft(tmp,M);

    % no interpolation
```

```
elseif (nint == M)
    undist(:,jj) = ICGI(abs(dist(:,jj)), B0(:,jj)/BW);

% not a good idea
else
    error('ICGI_1D: invalid interpolation parameter')
end;

end;
```

## A.4 KSC algorithm

```

function undist = KSC(dist,delta)
%
% undist_im = KSC(dist,delta)
%
% Implementation of the K-Space Correction method (fourier version)
%
% Input:   dist      Mx1 distorted profile
%          delta     Mx1 pixel displacement vector (in pixel units)
%
% Output:  undist    MxN corrected profile
%
%
% REF: Weisskoff R.M. et al., Correcting Gross Distortion on
%      Echo Planar Images, Proceedings of 11th Ann meeting SMR p.411 (1992)
%
%
M = length(dist);

% compute synthetic data
k = fftshift((0:(M-1))'-M/2);
m = (0:(M-1));
k_synth = exp( -2*pi*i*k*(m-delta')/M) * dist;

% reconstruct undistorted image
% phase correction on reconstructed image because k=-M/2 -> t=0 in
% the trajectory
% exp(2*pi*i*delta/2)
% no need to compute this factor if only the magnitude corrected
% image is wanted
% undist = ifft(k_synth).*exp(2*pi*i*delta/2);
undist = ifft(k_synth);

```

```
function undist = KSC_1D(dist,B0,traj)
%
% undist = KSC_1D(dist,B0,traj)
%
% Applies the KSC method to all columns of an image.
%
% Input: dist      MxN distorted image
%         B0       MxN field map (Hz)
%         traj     MxN k-space trajectory (s)
%
% Output: undist   MxN corrected image
%
% get image dimensions
[M,N] = size(dist);

% allocate space for corrected image
undist = zeros(M,N);

% loop over columns
for jj=1:N

    % effective bandwidth
    BW = 1/(traj(M,jj)-traj(1,jj));

    % apply KSI on column
    undist(:,jj) = KSC(dist(:,jj),B0(:,jj)/BW);

end;
```

## A.5 Analytic phantom

```

function samples = circle2D(parx,pary,r0,center,int)
%
% samples = circle2D(parx,pary,r0,center,int)
%
% Returns the samples of the 2D Fourier transform of a circle
% at the positions kx, ky.
%
% Input:  parx:      [FOVx, Nx]
%         pary:      [FOVy, Ny]
%         r0:        Radius of the circle
%         center:    [x,y] of the center
%         int:       Multiplicative factor (intensity)
%
% Output samples:   (Nx)x(Ny) matrix representing the k-space
%                   sample of the object.
%                   for a FOV of (FOVx)c(FOVy)
%
FOVx = parx(1); Nx = parx(2);
FOVy = pary(1); Ny = pary(2);
dx = FOVx/Nx;
dy = FOVy/Ny;
dkx = 1/Nx/dx;
dky = 1/Ny/dy;

[kx, ky] = meshgrid( -1/2/dx:dkx:1/2/dx-dkx, 1/2/dy:-dky:-1/2/dy+dky );
r = sqrt(kx.^2+ky.^2);
ind_orig = find(r==0);
r(ind_orig) = 1;
samples = zeros(size(kx));
samples = int*r0*besselj(1,2*pi*r0*r)./r;
samples(ind_orig) = int*pi*r0^2;

% offcenter
samples = samples.*exp(2*pi*i*(center(1)*kx+center(2)*ky));

```

```

function samples = rect2D(parx,pary,dim,center,int)
%
% samples = circle2D(parx,pary,dim,center,int)
%
% Returns the samples of the 2D Fourier transform of a rectangle.
%
% Input:  parx:      [FOVx, Nx]
%         pary:      [FOVy, Ny]
%         dim:       a and y dimensions of the rectangle
%         center:    [x,y] of the center
%         int:       Multiplicative factor (intensity)
%
% Output samples:   (Nx)x(Ny) matrix representing the k-space
%                   sample of the object.
%                   for a FOV of (FOVx)c(FOVy)
%
FOVx = parx(1); Nx = parx(2);
FOVy = pary(1); Ny = pary(2);
dx = FOVx/Nx;
dy = FOVy/Ny;
dkx = 1/Nx/dx;
dky = 1/Ny/dy;
[kx, ky] = meshgrid( -1/2/dx:dkx:1/2/dx-dkx, 1/2/dy:-dky:-1/2/dy+dky );

epsilon = 0.0001;
ind_orig = find(kx==0);
kx(ind_orig) = epsilon*ones(size(kx(ind_orig)));
ind_orig = find(ky==0);
ky(ind_orig) = epsilon*ones(size(ky(ind_orig)));
samples = zeros(size(kx));
samples = int*sin(pi*dim(1)*kx)./(pi*kx).*sin(pi*dim(2)*ky)./(pi*ky);

% offcenter
samples = samples.*exp(2*pi*i*(center(1)*kx+center(2)*ky));

```

```

% 2D analytical phantom test
%
%
%
%
%

clear all;

% imaging parameters
FOVx = 256;
FOVy = 256;
Nx = 64;
Ny = 64;
Radius = 110;
T = 2*Radius/sqrt(2)*0.98;
Width = 10;
Gap = 10;
%%%%%%%%%%%%%%%%%%%%%%%%%%%%%%%%%%%%%%%%%%%%%%%%%%%%%%%%%%%%%%%%%%%%%%%%

N_squares = floor( (T+Width)/(Width+Gap) )
T = N_squares*(Width+Gap)-Gap;

% phantom background
k_space = circle2D([FOVx Nx],[FOVy Ny],Radius,[0 0],1);

% squares
for ii = 1:N_squares
    for jj = 1:N_squares
        disp(['... computing square ', num2str(ii), ', ', num2str(jj), ' ...']);
        centerx=-T/2+Width/2+(ii-1)*(Gap+Width);
        centery=-T/2+Width/2+(jj-1)*(Gap+Width);
        k_space = k_space + ...
            rect2D([FOVx Nx],[FOVy Ny],[Width Width],[centerx centery],2);
    end;
end;

% reconstruct
phantom = fftshift(fft2(fftshift(k_space)));

```

## A.6 EPI image simulation

```

function epi = simulate_epi(im, B0, traj)
%
%
% epi = simulate_epi(undist_im, B0, traj)
%
% Compute a simulated EPI image
%
% Input:      im:      MxN image
%             B0:      B0 field map in Hz
%             traj:    k-space trajectory in s
%
% Output:     epi:     MxN simulated EPI image
%
[M,N] = size(im);

k = zeros(size(im));
[l1,kk] = meshgrid(-N/2:N/2-1,-M/2:M/2-1);

% loop over the pixels of the image
for ii = -M/2:M/2-1
    for jj = -N/2:N/2-1
        k = k + im(ii+M/2+1,jj+N/2+1)* ...
            exp ( -2*pi*i*(ii*kk/M + jj*l1/N + ...
                B0(ii+M/2+1,jj+N/2+1)*traj) );
    end; % jj
end; % ii

% reconstruct epi image
epi = fftshift(iff2(fftshift(k)));

```

## A.7 K-space trajectory

```

function traj = make_traj(ADC_raster_file, M, N, TR, offset)
%
% traj = make_traj(ADC_raster_file, M, N, TR, offset)
%
% Makes an EPI k-space trajectory from a raster file
%
% Input:          ADC_raster_file: file name
%                M:            number of k-space lines
%                N:            size of the raster file
%                TR:           time to read one k-space line (us)
%                offset:      time the readout begins (us)
%
% Output:        traj:        MxN matrix whose element traj(i,j)
%                            represents the time at which
%                            point (i,j) of k-space was sampled.
%                            Units of traj are in seconds.
%
%
t = read_adc_raster([ADC_raster_file, '_', num2str(N), '.txt'], N);

d = (TR-t(N)/1e3)/2;

T = offset;

% make k-space trajectory
for ii=1:2:M
    T = T+d;
    traj(ii,:) = T+t/1e3;
    T = traj(ii,N)+2*d;
    traj(ii+1,:) = T+fliplr(t)/1e3;
    T = traj(ii+1,1)+d;
end;

traj=traj/1e6; % change units for seconds

```

```
#include <stdio.h>
#include <string.h>
#include <math.h>
#include "mex.h"

void mexFunction(
    int nlhs,      mxArray *plhs[],
    int nrhs, const mxArray *prhs[]
)

{
    char tmp_string[100];
    char *file_name;
    FILE* f;
    int tmp, i, buflen, N;
    double* tmp_vect;
    int* tmp_vect2;

    /* Check for proper number of arguments */
    if (nrhs != 2) {
        mexErrMsgTxt("read_adc_raster requires two input arguments.");
    }
    if (nlhs != 1) {
        mexErrMsgTxt("read_adc_raster requires one output argument.");
    }

    /* get file name */
    buflen = (mxGetM(prhs[0])*mxGetN(prhs[0])) + 1;
    file_name = mxMalloc(buflen, sizeof(char));
    mxGetString(prhs[0], file_name, buflen);

    f = fopen(file_name,"r");

    if (!f) mexErrMsgTxt("read_adc_raster: cannot open file\n");

    N = *mxGetPr(prhs[1]);
    tmp_vect = mxMalloc(N,sizeof(double));
    tmp_vect2 = mxMalloc(N,sizeof(int));

    while(!feof(f)) {
        fscanf(f,"%s",tmp_string);
        if (!strcmp(tmp_string, "Entry_Values:")) break;
    }
}
```

```
    }  
    for (i=0; i<N; i++) {  
        fscanf(f,"%d",&tmp_vect2[i]);  
        tmp_vect[i] = (double)tmp_vect2[i];  
    }  
  
    plhs[0] = mxCreateDoubleMatrix(1,N,mxREAL);  
    mxSetPr(plhs[0],tmp_vect);  
  
    return;  
}
```

## A.8 Support functions

```

function n = B0_noise(mag, SNR, mask)
%
% n = B0_noise(mag, sigma, mask)
%
% Creates B0 map noise
%
% Input:      mag      MxN magnitude image
%            SNR      SNR of one of the magnitude image
%            mask     image mask
%
% Output     n        MxN noise matrix
%
% Field map are typically obtained from the difference between
% the phase of two images. The parameter SNR is the signal-to-noise
% ratio of the two images generating the field map.
%
% compute standard deviation
sigma = mean(abs(mag(mask)))/SNR;

% phase noise in background: uniformly distributed between -pi and pi
n_ph = (rand(size(mag))*2*pi-pi);

% phase noise in signal regions: normally distributed
% with std dev = sigma/mag
n_ph(mask) = randn(size(mask))*sigma./mag(mask);

% because 2 phase images are subtracted, the noise standard deviation
% is sqrt(2) larger.
dt = 4480e-6;
n = n_ph/2/pi/dt*sqrt(2);

```

```
function d = rms_diff(a,b,mask)
%
% d = rms_diff(a,b,mask)
%
% Computes the RMS difference between two images
%
% Input:  a           First image
%         b           Second Image
%         mask        Image mask over which the difference is evaluated.
%                   See image_mask function.
%
% Output: d           RMS difference
%

[M,N] = size(a);
d=sqrt( sum( ( abs(a(mask)) - abs(b(mask)) ).^2 ) /M/N);
```

```
function [m,bk] = image_mask(im,th)
%
% [m,bk] = image_mask(im,th)
%
% Computes the image and background mask for an image based on a threshold.
%
% Input:  im          Image
%         th          Threshold in percent of maximum image value.
%
% Output: m          Image mask, i.e. indices for which abs(im) >= th
%         bk          Background mask, i.e. indices for which
%                   abs(im) < th
%
% convert threshold in absolute pixel value
thpercent = max(im(:))*th/100;

% compute image make
m = find( abs(im(:)) >= thpercent );

% find background mask as the complement of image mask
bk = setdiff(1:length(im(:)),m)';

if (length(m)+length(bk))~=length(im(:))
    error('image_mask: Abnormal image mask calculation')
end
```

```
function g = gauss(M,N,FWHM,cx,cy)
%
% g = gauss(M,N,FWHM,cx,cy);
%
% Creates an MxN Gaussian centered at the origin.
%
% Input:  M,N           Size of the 2D gaussian
%         FVWM         Full Width at Half maximum in pixel units
%         cx,cy        Center
%
% Output: g           2D Gaussian
%

% set default values
if (nargin==3)
    cx = 0;
    cy = 0;
end;

% compute variance
a = FWHM^2/4/log( 2 );

[x,y] = meshgrid(-N/2:N/2-1,-M/2:M/2-1);
g = exp( - ( (x-cx).*(x-cx) + (y+cy).*(y+cy))/a );
```

```
function ind = circ_ind(x,N);
%
% ind = circ_ind(x,N)
%
% Circular index in the range 1:N, i.e. circ_ind(x+n*N,N) = x if 1<=x<=N
%
% Input:  x           Index
%         N           range
%
% Output: ind        Index
%
ind = mod(x-1,N)+1;
```

```
function B02 = B0_interp(B0,nint);
%
% B02 = B0_interp(B0,nint)
%
% Performs cubic interpolation on a 1D field map
%
% Input:  B0           Nx1 field map
%         nint        Size of interpolated field map
%
% Output: B02         nintx1 interpolated field map
%
% get B0 map dimensions
N = length(B0);

% perform cubic interpolation
B02 = interp1(1:N,B0,1:N/nint:N+1-N/nint,'*cubic')*nint/N;

% replace NaN values by 0
B02(isnan(B02))=0;
```

# Bibliography

- [1] A. Abragam. *The Principles of Nuclear Magnetism*. Oxford, 1961.
- [2] L. Axel and L. Dougherty. Heart wall motion: improved method of spatial modulation of magnetization for MR imaging. *Radiology*, 172(2):349–50, Aug 1989.
- [3] L. Axel and L. Dougherty. MR imaging of motion with spatial modulation of magnetization. *Radiology*, 171(3):841–5, Jun 1989.
- [4] C.J.G. Bakker, R. Bhagwandien, M.A. Moerland, and L.M.P. Ramos. Simulation of susceptibility artifacts in 2D and 3D Fourier Transform spin-echo and gradient-echo magnetic resonance imaging. *Magnetic Resonance Imaging*, 12(5):767–774, 1994.
- [5] C.J.G. Bakker, M.A. Moerland, R. Bhagwandien, and R. Beersma. Analysis of machine-dependent and object-induced geometric distortion in 2DFT MR imaging. *Magnetic Resonance Imaging*, 10(4):597–608, 1992.
- [6] A.W. Beavis, P. Gibbs, R.A. Dealey, and V.J. Whitton. Radiotherapy treatment planning of brain tumours using MRI alone. *British Journal of Radiology*, 71(845):544–8, 1998.

- [7] P. Bendel. Echo Projection Imaging – a method to obtain NMR images undistorted by magnetic field inhomogeneities. *IEEE Transactions on Medical Imaging*, 4(2), June 1985.
- [8] R. Bhagwandien, R. Van Ee, R. Beersma, C.J.G. Bakker, M.A. Moerland, and J.J.W. Lagendijk. Numerical analysis of the magnetic field for arbitrary magnetic susceptibility distributions in 2D. *Magnetic Resonance Imaging*, 10:299–313, 1992.
- [9] A. M. Blamire and R. G. Shulman. Implementation of echo-planar imaging on an unmodified spectrometer at 2.1 Tesla for functional imaging. *Magnetic Resonance Imaging*, 12(4):669–73, 1994.
- [10] F. Bloch. Nuclear induction. *Physical Review*, 70:460–474, 1946.
- [11] Ch. Boesch, R. Gruetter, and E. Martin. Temporal and spatial characterization of eddy current fields in high-field superconductive magnets. In *Proceedings of the 8th annual meeting of the SMRM*, page 965, Amsterdam, The Netherlands, 1989.
- [12] R. Bowtell, D.J.O. McIntyre, M-J. Commandre, P.M. Glover, and P. Mansfield. Correction of geometric distortion in echo planar images. In *Proceedings of the 12th annual meeting of the SMRM*, page 411, 1993.
- [13] H. Bruder, H. Fischer, H. E. Reinfelder, and F. Schmitt. Image reconstruction for echo planar imaging with nonequidistant k-space sampling. *Magnetic Resonance in Medicine*, 23(2):311–23, Feb 1992.

- [14] M.H. Buonocore and L. Gao. Ghost artifact reduction for echo planar imaging using image phase correction. *Magnetic Resonance in Medicine*, 38(1):89–100, Jul 1997.
- [15] K.J. Burchiel, T.T. Nguyen, B.D. Coombs, and J. Szumoski. MRI distortion and stereotactic neurosurgery using the Cosman-Roberts-Wells and Leksell frames. *Stereotactic Functional Neurosurgery*, 66(1-3):123–36, 1996.
- [16] C. Calmet, D. Vincensini, J. Bonnet, C. Bertino, A. Catala, M. Martinez, and F. Joffre. MRI dosimetry: a fast quantitative MRI method to determine 3D absorbed dose distributions. *Investigation Radiology*, 34(3):236–41, 1999.
- [17] H. Chang and J.M. Fitzpatrick. Geometrical image transformation to compensate for MRI distortions. In *SPIE Vol. 1233 Medical Imaging IV: Image Processing*, 1990.
- [18] H. Chang and J.M. Fitzpatrick. A technique for accurate magnetic resonance imaging in the presence of field inhomogeneities. *IEEE Transactions on Medical Imaging*, 11(3):319–329, 1992.
- [19] C-N Chen and Hould D.I. *Biomedical Magnetic Resonance Technology*. Adam Hilger, Bristol and New York, 1989.
- [20] N-K. Chen and A.M. Wyrwicz. Correction for EPI distortions using multi-echo gradient-echo imaging. *Magnetic Resonance in Medicine*, 41:1206–1213, 1999.
- [21] Z.H. Cho, D.J. Kim, and Y.K. Kim. Total inhomogeneity correction including chemical shifts and susceptibility by view angle tilting. *Medical Physics*, 15(1):7–11, 1988.

- [22] Z.H. Cho, H.S. Kim, H.B. Song, and J. Cumming. Fourier transform nuclear magnetic resonance tomographic imaging. *Proceedings of the IEEE*, 70(10):1152–1173, Oct 1982.
- [23] S.C.-K Chu, Y. Xu, J.A. Balschi, and C.S. Jr. Springer. Bulk magnetic susceptibility shifts in NMR studies of compartmentalized samples: Use of paramagnetic reagents. *Magnetic Resonance in Medicine*, 13:239–262, 1990.
- [24] W.C. Chu, B. Bavarian, C.B. Ahn, Y.S. Kwoh, and E.A. Jonckheere. Distortion compensation in MR images for robotic stereotactic procedures. *Proceedings of Spie - the International Society for Optical Engineering*, vol.1349,, 1349:421–30, 1990.
- [25] C. Cohen-Tannoudji, B. Diu, and Laloe F. *Mécanique Quantique*. Enseignement des Sciences. Hermann, Paris, 1980.
- [26] A.G. Collins, D.J. Bryant, I.R. Young, D.G.T. Thomas, S.S. Gill, and G.M. Bydder. Analysis of the magnitude of susceptibility effects in disease of the brain: Implications for MR spectroscopy. *Journal of Computer Assisted Tomography*, 12(5):775–777, Sep / Oct 1988.
- [27] R.T. Constable and R.M. Henkelman. Contrast, resolution, and detectability in MR imaging. *Journal of Computer Assisted Tomography*, 15(2):297–303, Mar/Apr 1991.
- [28] B.L.K. Davey, R.M. Comeau, C. Gabe, A. Olivier, and T.M. Peters. Interactive stereoscopic image-guided neurosurgery. In *Proceedings of SPIE Medical Imaging*, volume 2164, pages 167–176. SPIE, 1994.

- [29] B.L.K. Davey, R.M. Comeau, P. Munger, L.J. Pisani, D. Lacerte, A. Olivier, and T.M. Peters. Multimodality interactive stereoscopic image-guided neurosurgery. In Richard A. Robb, editor, *Proceedings of Third Conference on Visualization in Biomedical Computing*, volume 2359, pages 526–536. SPIE, SPIE, Oct. 4-7 1994.
- [30] Y. De Deene, C. De Wagter, B. Van Duyse, S. Derycke, B. Mersseman, W. De Gerscm, T. Voet, E. Achten, and W. De Neve. Validation of MR-based polymer gel dosimetry as a preclinical three-dimensional verification tool in conformal radiotherapy. *Magnetic Resonance in Medicine*, 43(1):116–25, 2000.
- [31] M. Debois, R. Oyen, F. Maes, G. Verswijvel, G. Gatti, H. Bosmans, M. Feron, E. Bellon, G. Kutcher, H. Van Poppel, and Vanuytsel L. The contribution of magnetic resonance imaging to the three-dimensional treatment planning of localized prostate cancer. *Int J Radiat Oncol Biol Phys.*, 45(4):857–65, 1999.
- [32] F. Di Salle, E. Formisano, D.E. Linden, R. Goebel, S. Bonavita, A. Pepino, F. Smaltino, and G. Tedeschi. Exploring brain function with magnetic resonance imaging. *Eur J Radiol.*, 30(2):84–94, 1999.
- [33] W. Thomas Dixon. Simple proton spectroscopic imaging. *Radiology*, 153:189–194, 1984.
- [34] W.A. Edelstein, G.H. Glover, C.J. Hardy, and R.W. Redington. The intrinsic signal-to-noise ratio in NMR imaging. *Magnetic Resonance in Medicine*, 3:604–618, 1986.

- [35] W.A. Edelstein, J.M.S. Hutchison, G. Johnson, and T. Redpath. Spin warp NMR imaging and applications to human whole-body imaging. *Phys. Med. Biol.*, 25:751-756, 1980.
- [36] D.T. Edmonds and M.R. Wormald. Theory of resonance in magnetically inhomogeneous specimens and some useful calculations. *J. Magn. Res.*, 77:223-232, 1988.
- [37] A. Ericsson, A. Hemmingsson, B. Jung, and G.O. Sperber. Calculation of MRI artifacts caused by static field disturbances. *Phys. Med. Biol.*, 33(10):1103-1112, 1988.
- [38] F. Farzaneh, Riederer S.J., and Pelc N.J. Analysis of T2 limitations and off-resonance effects on spatial resolution and artifacts in echo-planar imaging. *Magnetic Resonance in Medicine*, 14(1):123-39, April 1990.
- [39] E. Feig, F. Greenleaf, and M. Perlin. Magnetic resonance imaging with non-uniform fields. *Physics in Medicine and Biology*, 31(10):1091-1099, 1986.
- [40] R. L. Galloway, R. J. Maciunas, and James W. Latimer. The accuracies of four stereotactic frame systems: An independent assessment. *Biomedical Instrumentation and Technology*, 25:457-460, 1991.
- [41] R. L. Galloway Jr., R. J. Maciunas, and C. A. Edwards II. Interactive image-guided neurosurgery. *IEEE Transactions on Biomedical Engineering*, 39(12):1226-1231, Dec 1992.
- [42] A. Gauvin. Geometrical distortion of magnetic resonance images. Master's thesis, McGill University, May 1992.

- [43] W.M. Gedroyc. Interventional magnetic resonance imaging. *BJU Int.*, 86 Suppl 1:174–180, 2000.
- [44] G Gerig, O. Kubler, R Kikinis, and A.J. Ferenc. Nonlinear anisotropic filtering of MRI data. *Transactions on Medical Imaging*, 11(2):221–232, 1992.
- [45] G.H. Glover. Multipoint dixon technique for water and fat proton and susceptibility imaging. *Journal of Magnetic Resonance Imaging*, 1(5), 1991.
- [46] G.H. Glover and E. Schneider. Three-point Dixon technique for true water/fat decomposition with  $B_0$  inhomogeneity correction. *Magnetic Resonance in Medicine*, 18, 1991.
- [47] G.H. Golub and C.F. Van Loan. *Matrix Computations*. John Hopkins University Press, Baltimore and London, third edition, 1996.
- [48] J.C. Haselgrove and J.R. Moore. Correction for distortion of echo-planar images used to calculate the apparent diffusion coefficient. *Magnetic Resonance in Medicine*, 36(6):960–4, Dec 1996.
- [49] M.R. Hestenes. Pseudoinverse and conjugate gradients. *Communications of the ACM*, 18(1):40, January 1975.
- [50] W.S. Hinshaw and A.H. Lent. An introduction to NMR imaging: From the bloch equation to the imaging equation. *Proceedings of the IEEE*, 71(3):338–350, March 1983.
- [51] R.W. Holt, P.J. Diaz, J.L. Duerk, and E.M. Bellon. MR susceptometry: an external-phantom method for measuring bulk susceptibility from field-echo phase reconstruction maps. *Journal of Magnetic Resonance Imaging*, 37(3):212–8, Apr 1995.

- [52] J.M.S. Hutchison, R.J. Sutherland, and J.R. Mallard. NMR imaging: image recovery under magnetic fields with large non-uniformities. *J. Phys. E. Sci Instrum.* 11:217–221, 1978.
- [53] E.A. Jonckheere and S.a.n. Yik Kwok. Correction of distortion of MR pictures for MR-guided robotic stereotactic procedures. *Proceedings of Spie - the International Society for Optical Engineering*, 914:660–664, 1988.
- [54] Y.M. Kadah and X. Hu. Algebraic reconstruction for magnetic resonance imaging under  $B_0$  inhomogeneity. *IEEE Transactions on Medical Imaging*, 17(3):362–370, June 1998.
- [55] S.A.R. Kannengießer, Y. Wang, and E.M. Haacke. Geometric distortion correction in gradient-echo imaging by use of dynamic time warping. *Magnetic Resonance in Medicine*, 42:585–590, 1999.
- [56] A. Kawanaka and M. Takagi. Estimation of static magnetic field and gradient fields from NMR image. *J. Phys. E.: Sci. Instrum.*, 19:871–875, 1986.
- [57] S. Kawata and O. Nalcioglu. Constrained iterative reconstruction by the conjugate gradient method. *IEEE Transactions on Medical Imaging*, MI-4(2):65–71, 1985.
- [58] S.G. Kim and K. Ugurbil. Functional magnetic resonance imaging of the human brain. *J Neurosci Methods.*, 74(2):229–243, 1997.
- [59] A. Kumar, D. Welte, and R.R. Ernst. NMR fourier zeugmatography. *Journal of Magnetic Resonance*, 18:69–83, 1975.
- [60] K.K. Kwong. Functional magnetic resonance imaging with echo planar imaging. *Magn Reson Q.*, 11(1):1–20, 1995.

- [61] M.E. Ladd and J.F. Debatin. Interventional and intravascular MR angiography. *Hertz*, 25(4):440–541, 2000.
- [62] C.-M. Lai. Reconstruction NMR images under magnetic fields with large homogeneities. *J. Phys. E: Sci. Instrum.*, 15:1093–1100, 1982.
- [63] S. Langlois, M. Desvignes, J.M. Constans, and M. Revenu. MRI geometric distortion: A simple approach to correcting the effects of non-linear gradient fields. *Journal of Magnetic Resonance Imaging*, 9:821–831, 1999.
- [64] P.C. Lauterbur. Image formation by induced local interactions: Examples using nuclear magnetic resonance. *Nature*, 242:190–191, 1973.
- [65] R.J. Maciunas, J.M. Fitzpatrick, S. Gadamsetty, and C.R. Maurer Jr. A universal method for geometric correction of magnetic resonance images for stereotactic neurosurgery. *Stereotact Funct Neurosurg*, 66(1-3):137–40, 1996.
- [66] L. Man, J.M. Pauly, and Macovski A. Correcting severe local inhomogeneity blurs by spatially variant deconvolution. In *Proceedings of the 12th annual meeting of the SMRM*, page 738, 1993.
- [67] P. Mansfield. Multi-planar image formation using NMR spin echoes. *J. Phys. C (GB)*, 10(3):L55–8, Feb 1977.
- [68] R.A. Meuli, F.R. Verdun, F.O. Bochud, L. Emsley, and H. Fankhauser. Assessment of MR image deformation for stereotactic neurosurgery using a tagging sequence. *ajnr*, 15:45–49, Jan 1994.
- [69] J. Michiels, H. Bosmans, P. Pelgrims, D. Vandermeulen, J.Gybels, G. Marchal, and P. Suetens. On the problem of geometric distortion in magnetic resonance images for stereotactic neurosurgery. *Magnetic Resonance Imaging*, 12(5), 1994.

- [70] J.B. Miller and A.N. Garroway. Removal of static field inhomogeneity and chemical-shift effects in NMR imaging. *Journal of Magnetic Resonance*, 67:575–579, 1986.
- [71] T.J. Mosher and M.B. Smith. Magnetic susceptibility measurement using a double-DANTE tagging (DDT) sequence. *Magnetic Resonance in Medicine*, 18(1):251–5, Mar 1991.
- [72] P Munger, R.G. Crelier, T.M. Peters, and G.B. Pike. Conjugate gradient restoration of EPI images. In *Proceedings of the Sixth Annual Meeting of the International Society for Magnetic Resonance in Medicine. Sydney, Australia, April 1998*.
- [73] P Munger, R.G. Crelier, T.M. Peters, and G.B. Pike. An inverse problem approach to the correction of distortion in EPI images. *IEEE Transactions on Medical Imaging*, 19(7), July 2000.
- [74] D. G. Nishimura, J. I. Jackson, and J. M. Pauly. On the nature and reduction of the displacement artifact in flow images. *Magnetic Resonance in Medicine*. 22(2):481–92, Dec 1991.
- [75] D.G. Nishimura. Principles of magnetic resonance imaging. Lecture Notes, 1994.
- [76] D.G. Nishimura, A. Macovski, J.I. Jackson, R.S. Hu, C.A. Stevick, and L. Axel. Magnetic resonance angiography by selective inversion recovery using a compact gradient echo sequence. *Magnetic Resonance in Medicine*, 8(1):96–103, Sep 1988.

- [77] D.C. Noll, J.M. Pauly, C.H. Meyer, D.G. Nishimura, and A. Macovski. Deblurring for non-2D Fourier Transform magnetic resonance imaging. *Magnetic Resonance in Medicine*, 25:319–333, 1992.
- [78] M. O'Donnell and W.A. Edelstein. NMR imaging in the presence of magnetic field inhomogeneities and gradient field nonlinearities. *Medical Physics*, 12(1):20–26, Jan/Feb 1985.
- [79] D.R. Olsen and J. Hellesnes. Absorbed dose distribution measurements in brachytherapy using ferrous sulphate gel and magnetic resonance imaging. *Br J Radiol.*, 67(803):1121–6, 1994.
- [80] D.L. Parker and G. T. Gullberg. Signal-to-noise efficiency in magnetic resonance imaging. *Medical Physics*, 17(2):250–7, Mar-Apr 1990.
- [81] T.M. Peters, B.L.K. Davey, P. Munger, R.M. Comeau, A. Evans, and A. Olivier. Three-dimensional multi-modal image-guidance for neurosurgery. *IEEE Transactions on Medical Imaging*, 15:121–128, 1996.
- [82] J. G. Pipe, J. L. Boes, and T. L. Chenevert. Method for measuring three-dimensional motion with tagged MR imaging. *Radiology*, 35(5):771–80, May 1996.
- [83] S. Posse and W.P. Aue. Susceptibility artifacts in spin-echo and gradient-echo imaging. *Journal of Magnetic Resonance*, 88:473–492, 1990.
- [84] William K. Pratt. *Digital Image Processing*. John Wiley & Sons, 1978.
- [85] F.J. Prott, U. Haverkamp, H. Eich, A. Resch, O. Micke, A.R. Fishedick, N. Willich, and R. Potter. Effect of distortions and asymmetry in MR images on radiotherapeutic treatment planning. *Int J Cancer.*, 90(1):46–50, 2000.

- [86] J.A. Purdy. Intensity-modulated radiation therapy. *Int J Radiat Oncol Biol Phys.* 34(4):845-6, 1996.
- [87] I.L. Pykett and R.R. Rzedzian. Instant images of the body by magnetic resonance. *Magnetic Resonance in Medicine*, 5(6):563-71, Dec 1987.
- [88] P.J. Reber, E.C. Wong, R.B. Buxton, and L.R. Frank. Correction of off resonance-related distortion in echo-planar imaging using EPI-based field maps. *Magnetic Resonance in Medicine*, 39(2):328-30, Feb 1998.
- [89] T.G. Reese, T.L. Davis, and R.M. Weisskoff. Automated shimming at 1.5 T using echo-planar image frequency maps. *Journal of Magnetic Resonance Imaging*, 5(6):739-45, Nov-Dec 1995.
- [90] L. Schad, S. Lott, F. Schmitt, V. Sturm, and W.J. Lorenz. Correction of spatial distortion in MR imaging: A prerequisite for accurate stereotaxy. *Journal of Computer Assisted Tomography*, 11(3):499-505, 1987.
- [91] L.R. Schad, M. Bock, K. Baudendistel, M. Essig, J. Debus, M.V. Knopp, R. Engenhardt, and W.J. Lorenz. Improved target volume definition in radiosurgery of arteriovenous malformations by stereotactic correlation of MRA, MRI, blood bolus tagging, and functional MRI. *Eur Radiol*, 6(1):38-45, 1996.
- [92] L.R. Schad, Robert Boesecke, Wolfgang Schlegel and Gunther H. Hartmann, Volker Sturm, Ludwig G. Strauss, and Walter J. Lorentz. Three dimensional image correlation of CT, MR, and PET studies in radiotherapy treatment planning of brain tumors. *Journal of Computer Assisted Tomography*, 11, 1987.

- [93] K. Sekihara and H. Kohno. Image restoration from nonuniform static field influence in modified echo-planar imaging. *Medical Physics*, 14(6), Nov.-Dec. 1987.
- [94] K. Sekihara, M. Kuroda, and H. Kohno. Image restoration from non-uniform magnetic field influence for direct Fourier NMR imaging. *Physics in Medicine and Biology*, 29(1):15-24, 1984.
- [95] K. Sekihara, S. Matsui, and H. Kohno. A new method of measuring static field distribution using modified fourier NMR imaging. *J. Phys. E: Sci. Instrum.*, 18:224-227, 1985.
- [96] K. Sekihara, S. Matsui, and H. Kohno. A new method of measuring static field distribution using NMR images. *IEEE Transactions on Nuclear Science*, NS-32(1):799-802, Feb 1985.
- [97] J.R. Shewchuk. An introduction to the Conjugate Gradient method without the agonizing pain. Web document. School of Computer Science, Carnegie Mellon University, Pittsburgh, PA, March 1994.
- [98] L. Shizhe, J.A. Gilmore, Q.X. Yang, and M.B. Smith. Three dimensional finite element calculations of magnetic susceptibility effects in high resolution anatomical models of human head. In *Proceedings of the Society of Magnetic Resonance*, volume 2, page 831, 1994.
- [99] J. Sijbers, A.J. den Dekker, J. Van Audekerke, M. Verhoye, and D. Van Dyck. Estimation of the noise in magnitude MR images. *Magnetic Resonance Imaging*, 16(1):87-90, 1998.

- [100] Jan Sijbers. *Signal and noise estimation from magnetic resonance images*. PhD thesis, Universiteit Antwerpen, 1998.
- [101] S.M.H. Song, S. Napel, N.J. Pelc, and G.H. Glover. Phase unwrapping of MR phase images using Poisson equation. *IEEE Transactions on Image Processing*, 4(5):667–676, 1995.
- [102] T.S. Sumanaweera, G.H. Glover, T.O. Binford, and J.R. Adler. MR susceptibility misregistration correction. *IEEE Transactions on Medical Imaging*, 12(2):251–259, 1993.
- [103] D. Twieg. The k-trajectory formulation of the NMR imaging process with applications in analysis and synthesis of imaging methods. *Medical Physics*, 10(5):610–621, 1983.
- [104] S. C. Wayte and T. W. Redpath. Estimating spatial resolution of in vivo MR images using spatial modulation of magnetization. *Magnetic Resonance Imaging*, 19(1):47–53, Jan 1995.
- [105] S Webb, editor. *The Physics of Medical Imaging*. IOP Publishing Ltd, Bristol, England, 1988.
- [106] J. Weis and L. Budinsky. Simulation of the influence of magnetic field inhomogeneity and distortion correction in MR imaging. *Magnetic Resonance Imaging*, 8(4):483–9, 1990.
- [107] R.M. Weisskoff, M.S. Cohen, and R.R. Rzedzian. Nonaxial whole-body instant imaging. *Magnetic Resonance in Medicine*, 29:796–803, 1993.

- [108] R.M. Weisskoff and T.L. Davis. Correcting gross distortion on echo planar images. In *Proceedings of the 11th annual meeting of the SMRM*, page 4515, 1992.
- [109] T.S. Wong and D. Rosenfeld. Spin-inversion imaging: A technique for NMR imaging under magnetic fields with high field nonuniformities. *IEEE Transactions on Medical Imaging*, MI-6(2):148-156, 1987.
- [110] S.Y. Woo, W.H. 3rd Grant, D. Bellezza, R. Grossman, P. Gildenberg, L.S. Carpentar, M. Carol, and E.B. Butler. A comparison of intensity modulated conformal therapy with a conventional external beam stereotactic radiosurgery system for the treatment of single and multiple intracranial lesions. *Int J Radiat Oncol Biol Phys.*, 35(3):593-597, 1996.
- [111] J.C. Wood and K.M. Johnson. Wavelet packet denoising of magnetic resonance images: importance of rician noise at low SNR. *Magnetic Resonance in Medicine*, 41(3):631-635, 1999.
- [112] M.L. Wood and R.M Henkelman. Truncation artifacts in magnetic resonance imaging. *Magnetic Resonance in Medicine*, 2, 1985.
- [113] I.R. Young, G.M. Bydder, S. Khenia, and A.G. Collins. Assessment of phase and amplitude effects due to susceptibility variations in MR imaging of the brain. *Journal of Computer Assisted Tomography*, 13(3):490-494, May / Jun 1989.
- [114] S. Zhang, M. A. Douglas, L. Yaroslavsky, R. M. Summers, V. Dilsizian, L. Fananapazir, and S. L. Bacharach. A Fourier based algorithm for tracking SPAMM tags in gated magnetic resonance cardiac images. *Medical Physics*, 23(8):1359-69, Aug 1996.